Micromachined Electrospray Thrusters for Spacecraft Propulsion

THÈSE N^O 4255 (2009)

PAR

Renato KRPOUN

ÉCOLE POLYTECHNIQUE
FÉDÉRALE DE LAUSANNE

Suisse
2009

Contents

Abstract

M̲ICROMACHINING has enabled the downscaling of large, massive and power hungry systems into small batch-produced integrated devices. Recent progress in electrospray thruster technology, in particular the discovery of an ionic emission mode using the ionic liquid EMI-BF$_4$ as fuel has sparked interest in miniaturizing this thruster technology, initially developed in the 1950's and lying dormant for several decades.

Electrospray thrusters operate by applying a potential difference between a conductive liquid, usually on the tip of a needle or capillary, and an extractor electrode. Once a threshold voltage is reached the electric stress at the apex of the liquid surface overcomes surface tension and a spray of particles is ejected toward a counter electrode. The purely electrostatic nature of this type of thruster makes it an ideal candidate for miniaturization and the use of ionic liquids, also known as molten salts, as fuel allows operating the thruster in bipolar mode eliminating the need for an additional neutralizer.

This thesis describes a process flow to fabricate planar arrays of silicon capillaries with integrated individual extractor electrodes. The developed process flow offers the possibility to manufacture arrays on the wafer scale allowing, in principle, to increase thrust from a fraction of micronewton for a single capillary to the millinewton level for large arrays. This process flow has been validated by microfabricating several thruster prototypes, which were packaged using Low Temperature Co-Fired Ceramic (LTCC) technology. In conjunction with this microfabrication process an onset voltage model was developed intended as design tool during thruster layout. This model allows to predict the voltage at which particle emissions initiate for complex geometries and to estimate the effect of dimensional variations on parameters such as crosstalk in large arrays.

Tests carried out with thruster prototypes using single capillaries show a well defined energy distribution of the particles and the possibility to modulate spray current by changing the voltage. Controlled variations in the fluidic impedance of the emitters allow to spray in either ionic or droplet mode. Time-of-flight measurements with arrays show a beam composed of ions (monomers, dimers), thus yielding a high specific impulse. A first life test finally shows thruster operation for several hours with stable beam properties.

Keywords: electrosprays, colloid thrusters, micropropulsion, microfabrication, ionic liquids, finite element modeling, satellite propulsion.

Résumé

De nos jours, la microfabrication permet la miniaturisation de systèmes à l'origine massifs et grands consommateurs de puissance en systèmes intégrés compacts pouvant être produits en série. Les progrès récents dans la technologie de propulseurs à électrospray, en particulier la découverte d'un mode d'émission ionique utilisant le liquide ionique EMI-BF$_4$ comme carburant, a éveillé l'intérêt pour la miniaturisation de ce type de propulseurs.

Les propulseurs à électrospray fonctionnent en appliquant une différence de potentiel entre un liquide conducteur, habituellement posé sur le bout d'une aiguille ou d'un capillaire, et une électrode d'extraction. Quand une tension limite est atteinte, la contrainte électrique à la pointe du liquide surpasse la tension de surface et un spray de particules est éjecté vers une électrode d'extraction. La nature purement électrostatique de ce type de propulseur en fait un candidat idéal pour la miniaturisation. L'utilisation de liquides ioniques, aussi appelés sels fondus, permet au propulseur de fonctionner en mode bipolaire, éliminant ainsi le besoin d'un neutraliseur additionnel.

Cette thèse décrit un procédé pour la microfabrication d'une matrice de capillaires en silicium ayant chacun une électrode d'extraction intégrée. Le procédé développé permet de fabriquer ces matrices à l'échelle d'un wafer (galette), augmentant ainsi la propulsion d'une fraction de micro-newton pour un seul capillaire à l'ordre du milli-newton pour de grandes matrices. Ce procédé a été validé utilisant des techniques de microfabrication et aboutissant au prototypage de différents types de propulseurs, lesquels ont été intégrés en utilisant le cofrittage de céramique à basse température (LTCC). En parallèle avec ce procédé de micro fabrication, un modèle de tension d'allumage a été développé dans le but d'être utilisé comme outil de conception pour le propulseur. Ce modèle permet de prédire la tension à partir de laquelle commence l'émission de particules dans le cas de géométries complexes et également d'estimer l'effet des variations de paramètres tel que l'effet de larges matrices sur le champ électrique.

Les tests effectués avec les prototypes de propulseurs utilisant un seul capillaire ont montré une distribution d'énergie des particules bien définies et la possibilité de moduler le courant emis en variant la tension. Les variations contrôlées de l'impédance du fluide émetteur permettent de pulvériser soit dans un mode ionique soit dans un mode de gouttelettes. Les mesures du temps de parcours dans le cas d'une matrice de capillaires ont montré un flux composé d'ions (monomères et dimères) permettant ainsi une haute impulsion spécifique. Les premiers tests ont montré que le propulseur peut fonctionner plusieurs heures avec des propriétés de faisceau stables.

Mots-clé: Electrospray, micro propulsion, microfabrication, liquides ioniques, modèle d'éléments finis, propulsion pour satellite.

Acknowledgments

With the exception of a few introverted geniuses having only paper, pencil and their brilliant minds as tools a thesis is an important team effort and mine is no exception. Without the help and support of my family, friends, and colleagues, to whom I wish to extend my gratitude, this work would not have been possible.

I first like to thank my advisor and friend Professor Herbert Shea to whom I am greatly indebted for giving me the opportunity and necessary support to embark on my 'micropropulsion journey'. His advice has been a key ingredient to the success of this thesis. I also owe much gratitude to Professor Yves Perriard, who has been a great mentor supporting my passion for space during my student years and without whom I most likely would not have started a thesis at all.

Microfabrication has been done in the cleanroom in Neuchâtel. Many thanks go to Sylvain Jeanneret and his team: Edith Millotte, Pierre-André Clerc and Stéphane Ischer, Giovanni Bergonzi, Rémy Fournier, Sylviane Pochon, Eduardo Santoli and José Vaquera. Without their support microfabrication would not have been possible. I would also like to thank Phillipe Flückiger and his team at the CMI in Lausanne for granting me access to their cleanroom and letting me experiment around with their wonderful tools.

A special thank goes to Kate Smith at Queen Mary, University of London, for her commitment and her contribution to this thesis in form of much advice, encouragement, and key experimental results. I am equally grateful for the help of Yannick Fournier, Thomas Maeder and Prof. Peter Ryser from the Laboratory of Microengineering for Manufacturing at EPFL for introducing me to the art of LTCC making. I would further like to thank my students Manuel Räber, Kaspar Jenni, Arnaud Salette and Léandro Durney to whom I am very grateful for their contributions to this project.

I am equally grateful for the financial support from the European Space Agency that helped getting my research started and would like to thank Jose Gonzales del Amo at ESTEC for his help and advice.

I am also greatly indebted to the members of my Jury: Prof. John Stark, Prof. Urs Staufer, Prof. Jürgen Brugger and Prof. Adrian Ionescu who kept an eye on me all along my thesis and have provided me with excellent suggestions and feed-back.

Frequently Used Terms, Abbreviations, and Notation

Terms and abbreviations

CVD: Chemical vapor deposition. Process used to deposit thin films.

DRIE: Deep reactive ion etching. Process to etch vertical walls into a substrate such as silicon, glass or metal.

FEEP: Field emission electric propulsion.

FWHM: Full width at half maximum, width of a pulse at $1/2$ of its maximum value. The relationship to the standard deviation, σ, is given by FWHM$= 2\sqrt{2\ln 2}\sigma$.

LPCVD: Low pressure chemical vapor deposition.

ILIS: Ionic liquid ion sources.

PCB: Printed circuit board.

RPA: Retarding potential analyzer.

RTIL: Room temperature ionic liquids. Class of solvents composed solely of anions and cations and liquid at room temperature.

SOI: Silicon-on-insulator. A silicon wafer composed of two silicon wafers separated by an insulating silicon dioxide layer. The insulating layer is used as etch-stop during plasma etching. The silicon layers are called device and handle layer whereas the oxide in between is called the buried oxide (BOX) layer.

TOF spectrometry: Time-of-flight spectrometry is used to determine the charge over mass ratio of particles in a charged beam.

Notation and variables

	Variables, functions ,symbols and operators;
a	Distance between center of RPA grid wires, m
A	Constant
A_e	Electrode surface on the emitter side, m^2
$B_{i,p}$	Bernstein basis function
d	Extractor electrode to tip distance
d_c	Capillary outer diameter (at the base), m
d_e	Extractor electrode hole diameter, m
d_i	Capillary inner diamter, m
d_o	Capillary outer diameter (at the tip), m
d_{sp}	Ruby micro-ball spacer diameter, m
D_c	Capillary array pitch, m
D_w	Distance between capillary and lateral sidewalls, m
$\vec{E}$	Electric field, V·m^{-1}
E_n, E_t	Electric field, normal and tangential components V·m^{-1}
f	Frequency, Hz
$f(x)$	Generalized function with the variable x
$g(\epsilon), G(\epsilon)$	Empirical parameters found in spray scaling laws
h_c	Capillary height, m
h_i	Insulator height or electrode to capillary tip distance, m
h_p	Distance between grounded and biased RP planes, m
h_u, h_v, h_w	Scale factors in the prolate spheroidal coordinate system
I	Current, A
I_F	Current collected in the Faraday cup, A
I_s	Surface current, A
I_{sp}	Specific impulse, s
K	Conductivity, S·m^{-1}
l_c	Capillary insulator groove diameter, m
l_e	Extractor insulator groove diameter, m
L_{TOF}	Time-of-flight length, m
m	Mass, kg
m_0	Mass of a particle emitted in an electrospray, kg
N	Number of particles
$\vec{P}_n$	Vectors representing points, $(n = 1, 2, \ldots, n)$
P_ν	Legendre polynomial of order the ν

q	Charge, C
Q	Volumetric flow rate, $\mathrm{m^3 \cdot s^{-1}}$
Q_0	Characteristic flow rate, $\mathrm{m^3 \cdot s^{-1}}$
Q_j	Volumetric flow rate of capillary segment j, $\mathrm{m^3 \cdot s^{-1}}$
Q_{min}	Minimum flow rate, $\mathrm{m^3 \cdot s^{-1}}$
r	Radial coordinate from the apex of the cone, m
r^*	Characteristic dimension of the relaxation region, m
r_1, r_2	Principal radii of curvature, m
r_a	Radius of curvature at apex of liquid surface, m
r_j	Radius of the capillary segment j, m
r_t	Radius at the tip of an hyperboloid needle, m
r_w	Radius of RPA grid wire, m
R_0	Jet diameter, m
s	Running parameter
t	Time variable, s
t_{TOF}	Time-of-flight, s
T	Thrust, N
T_m	Melting point temperature, °C
u, v, w	Alternative coordinates in the prolate spheroidal coordinate system
v_0	Constant representing an equipotential surface
v_e	Exhaust speed, $\mathrm{m \cdot s^{-1}}$
V_0	Equilibrium voltage between electric and surface stress, V
V_E	Emitter voltage, V
V_{oc}	Onset voltage, V
V_{ox}	Extinction voltage, V
V_{RP}	Retarding potential voltage, V
$V_w^{\pm}$	Electrochemical window limit, V
x, y, z	Coordinates in the cartesian coordinate system
Z_j	Flow impedance at segment j, $\mathrm{N \cdot s \cdot m^{-5}}$
α	Parameter in the prolate spheroidal coordinate system
α_s	Spray half angle
α_ρ	Non-dimensional flow rate
α_μ	Non-dimensional parameter indicating visous to inertial effects
β	Taylor cone half angle
γ	Surface tension, $\mathrm{N \cdot m^{-1}}$
δ	Kronecker delta
δ_{dl}	Double layer thickness, m
δ_μ	Viscous dimensionless parameter
δ_p	Pressure difference across liquid meniscus, Pa

ΔP	Pressure difference across feed system, Pa
ΔP_j	Pressure difference at capillary segment j, Pa
Δt_j	Filling time of capillary segment j, s
Δx_j	Length of the capillary segment j, m
ϵ	Dielectric constant
θ	Polar angle of spherical coordinate system
θ_0	Inverse Taylor cone angle, $\theta_0 = \pi - \beta$
μ	Viscosity, Pa·s
μ	Median
ξ, η, ϕ	Coordinates in the prolate spheroidal coordinate system
ρ	Mass density, kg·m^{-3}
σ	Standard deviation
σ_E	Electrical stress, N·m^{-2}
σ_γ	Surface tension stress, N·m^{-2}
ϕ	Azimuth angle of spherical coordinate system
Φ	Electric potential, V
Φ_0	Boundary potential ($\Phi_0 = \Phi(v_0)$), V
Φ_B	Beam potential, V

Operators;

$\vec{\nabla}$	Gradient operator
∇^2	Laplace operator
$\langle \ldots \rangle$	Average

Fixed constants;

g_0	Gravitational acceleration on earth, 9.82 m·s^{-2}
q_0	Elementary charge $1.60217646 \cdot 10^{-19}$ C
ϵ_0	Permittivity of free space, $8.854 \cdot 10^{-12}$ C^2·N^{-1}·m^{-2}

Chapter 1

Introduction

Eｌｅｃｔｒｏｓｐｒａｙｓ have been known for almost a century and their potential use as thruster on spacecraft has been recognized very early in the history of space exploration. But only recently, after lying dormant for several decades, the technology has reappeared and gained sufficient confidence from spacecraft designers to be included as propulsion system on a mission. This renaissance has occurred for several reasons and is closely linked to the appearance of small satellites and the increased research efforts to develop suitable "micropropulsion" systems allowing to add maneuvering capabilities to this particular class of spacecraft. On the other hand future flagship missions planning for several satellites to fly in formation while keeping their position with nanometer precision require novel high-performance propulsion systems providing large throttling capabilities and extended lifetimes. Another important factor has been the popularity of electrosprays in mass spectrometry of large macromolecules which has made elements such as pulled silica needles or microfluidic components readily available on the market. Finally the discovery of room temperature ionic liquids (RTIL) and their unique properties have been an important contributor to the breakthrough of electrospray thruster technology.

This chapter will introduce the principle of operation of an electrospray thruster. It will review the early history, the major milestones in the development of electrosprays for spacecraft applications and discuss the present research efforts. The chapter will be concluded with the outline of this work, its objectives and contributions to the field.

1.1   Operation principle of an electrospray thruster

When a sufficiently large potential difference is applied between a conductive liquid inside a capillary and an extractor electrode the liquid surface at the tip of the capillary sharpens and eventually, once a threshold voltage is reached, snaps into a cone like protrusion and emission sets-in. These sources of small droplets or ions are known as *electrosprays* or when used as propulsion system for satellites also as *colloid thrusters*.
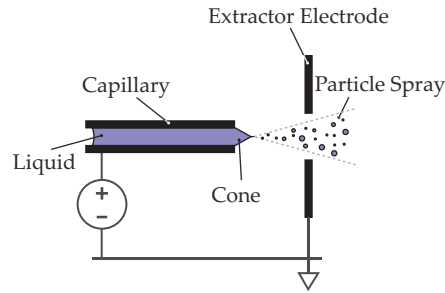
Figure 1.1: Arrangement of an electrospray or colloid thruster. Droplets and ions are extracted from a conductive liquid by applying a potential difference between the conductive liquid and the extractor electrode.
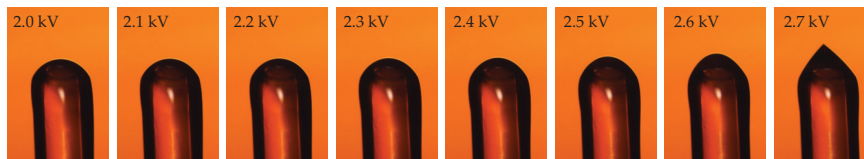
Figure 1.2: Sharpening of the ionic liquid EMI-BF$_4$ at the tip of a capillary with 150 μm inner and 360 μm outer diameter. The extractor electrode above the capillary is not shown. The sharpening occurs as the voltage difference is increased. Above 2.7 kV the liquid deforms into a cone-like structure and emission sets in.

Figure 1.1 shows the basic arrangement of an electrospray thruster, where a capillary containing a conductive liquid is facing an extractor electrode. Within a stability window the emitted spray current can be controlled by changing the potential or the flow rate. To further accelerate the particles an additional element can be added called the acceleration electrode (not shown in the figure). The charged particles are accelerated toward the extractor electrode and, when properly neutralized, generate a small amount of thrust when they are lost into space. The picture series in figure 1.2 illustrates the evolution of the liquid at the tip of a capillary. As the voltage is increased the apex of the liquid sharpens and eventually deforms into a cone like structure.

1.2 Brief history of colloid thruster research

1.2.1 First electrospray experiments

The first observations of electrosprays were recorded by Zeleny (1914, 1917). His discharge experiments were conducted in air and the experimental setup consisted of a glass capillary filled with various liquids (diluted hydrochloric acid, ethanol, glycerine) which was placed above a grounded plate. By varying the pressure of the liquid and the voltage difference between the liquid and the plate Zeleny observed

(a) Cone with jet

(b) Zeleny's experimental setup
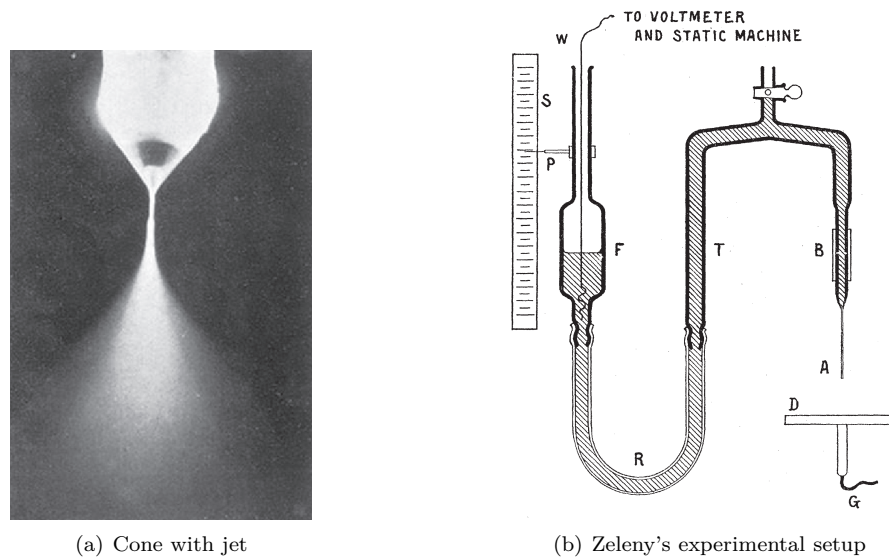
Figure 1.3: (a) Cone with jet observed on the tip of a capillary by Zeleny. The capillary had a diameter of 0.92 mm and the liquid was ethyl alcohol. (b) Zeleny's experimental setup. The glass capillary 'A' faced a brass disc 'D' serving as extractor electrode. Liquid pressure could be controlled by changing the height of the glass reservoir 'F'. Electrical contact was done through the wire 'W'. Both images are taken from Zeleny (1914, 1917).

and photographed the behavior of the liquid at the tip of the capillary. In his paper he comments on the formation of a cone at the tip of the capillary (Zeleny 1917):

> "Under certain conditions of potential and hydrostatic pressure it is possible to get the alcohol drop at the end of the tube to assume the form of a cone with a fine thread of liquid coming from its apex".

In the 1930's investigations with electrosprays were done by Macky (1931). His motivation was to understand the behavior of water droplets in strong electric fields, such as the ones present in thunderstorms. During his experiments water droplets fell through a strong electric field, were elongated and eventually formed a cone on the opposite sides facing the electrodes. He observed that the positive end of the droplet would deform more readily into cone like protrusion than the negative one and under certain conditions a jet would appear. Based on this research further work was done by English (1948) and Drozin (1955) who studied the characteristics of electrosprays with various liquids.

1.2.2 Early colloid thruster research

Following the very early investigations the first reports on the use of electrosprays to generate thrust for spacecraft propulsion appeared in the early 1960's. A joint research effort on an electrospray thruster was undertaken in the US by TRW Inc. and the

Aero Propulsion Laboratory at Wright-Patterson Air Force Base. This collaboration is first mentioned in a paper by Hendricks (1962) in which the author describes the determination of the charge-to-mass ratio of an electrospray using octoil, a low vapor pressure oil used in diffusion pumps. In a paper entitled "Present status of colloid microthruster technology" Huberman *et al.* (1968) provide a more detailed overview of this collaboration:

> "This work has been devoted primarily to developing 1) optimum performance capillary dimensions and geometry, 2) a suitable high performance propellant, and 3) adequate diagnostic techniques for thruster analysis."

Although these research objectives were formulated over 40 years ago they are still up-to-date. The paper describes time-of-flight measurements done with thrusters using glycerol doped with NaI as propellant. These spray experiments were done with capillaries having an inner diameter of 100 μm and a 360 μm outer diameter. Further tests were performed with a bipolar thruster array, expelling positive and negative droplets simultaneously. The paper also reports on lifetimes greater than 100 hours for a 60 capillary emitter array and on a colloid engine breadboard operated for over 1'500 hours with a specific impulse, a measure to describe thruster efficiency, of $I_{sp} = 800$ s and introduces the concept of a slit geometry thruster to obtain larger thrust densities.

Work on a annular slit thruster was also initiated at NASA Goddard Space Flight Center by Stark and Sherman (1970). They first tested simple capillaries to gain experience in colloid thruster operation and then moved on to an annular design. They tested forty eight different single emitter configurations varying materials, capillary geometries and fuels. The tested fuels included glycerol doped with NaI, H_2SO_4, HCL and NaOH. Capillaries were made of Hastelloy C, a corrosion resistant alloy, Platinum and a Platinum - 10% Iridium alloy. The developed annular thrusters had a maximum specific charge of $\langle q/m_0 \rangle = 2'852$ C/kg, a thrust around $T = 25$ μN and a specific impulse of $I_{sp} = 1'085$ s.

Early research on electrospray thrusters in Europe was carried out at the European Space Research and Technology Centre (ESTEC) and at Southampton University. Bailey *et al.* performed experiments with slit, annular and single emission site thrusters. Like their American colleagues they used a sodium iodide/glycerol (20% NaI by weight) solution. The performance of the slit thruster was measured with a torsion balance (Bailey *et al.* 1972) and the results were a thrust of $T = 100$ μN and an exhaust speed of $\langle v_e \rangle = 12$ km/s. This thruster configuration was abandoned due to manufacturing problems.

The voltage/current characteristic of the European 2 cm annular thruster (Bailey 1973) is reported to resemble a Zener-diode as over the operation range of 50-400 μA the voltage changes by only 15%. The thruster was operated with negative and positive voltages and in both cases the thruster characteristics were reported to be similar. For the annular thruster configuration the authors believed that multiple emission sites were present. Thrust measurements were done by means of a thrust

balance with a resolution down to 10^{-7} N. The maximum charge over mass ration obtained for this thruster was $\langle q/m_0 \rangle = 1.2 \cdot 10^4$ C/kg at a thrust of 400 μN and a mass flow rate of $\dot{m} = 5.4 \cdot 10^{-8}$ kg/s. Interestingly the mass flow rate was reported to be fairly constant over the whole operating range. The computed exhaust speed was approximately $\langle v_e \rangle = 6$ km/s.

Their third thruster design, a single emission site thruster, had the advantage of limiting emission to one single site. For a restricted mass flow rate (Bailey 1973) a thrust of $T = 0.056$ μN, a charge over mass ratio of $\langle q/m_0 \rangle = 33'000$ C/kg and an exhaust speed of $\langle v_e \rangle = 19$ km/s were measured.

In the mid-seventies a shift in interest toward the Shuttle program in the US and the Ariane launcher in Europe led to budgetary restrictions and the research on colloid thrusters was halted. For further information on electrospray thruster history the interested reader is referred to the detailed account compiled by López Urdiales (2004).

1.2.3   Recent research and state of the art

A renaissance of electrospray (colloid) propulsion systems has taken place at the end of the last century. The newly gained interest in this technology can be linked to the effort to miniaturize satellite systems. Malyshev *et al.* (1995) proposed the use of such a colloid system for small satellites and reported on a 30 W thruster with 2'800 hours of lifetime developed at the Moscow State Aviation Institute with a thrust up to $T = 1$ mN, a specific charge of $\langle q/m_0 \rangle = 3'300$ C/kg and a specific impulse of $I_{sp} = 1'000$ s at an acceleration voltage of 15 kV.

Compared with other electric propulsion systems electrospray thrusters can be easily miniaturized, have high efficiencies and specific impulse. Although research on electrospray thrusters had disappeared in the west for almost thirty years the use of electrosprays for mass spectrometry of large organic molecules had popularized the technology (Fenn *et al.* 1989) and made components such as needles or microfluidic components readily available.

A first collaboration was started between professor Martínez-Sánchez at the Massachussets Institute of Technology, professor Fernández de la Mora at Yale University and Vlad Hruby at Busek Co. (Martínez-Sánchez *et al.* 1999). Investigating novel fuels they showed that with the ionic liquid 1-ethyl-3-methyl-imidazolium tetrafluoroborate (EMI-BF$_4$) a purely ionic spray mode can be reached (Romero-Sanz *et al.* 2003) with a specific mass above $\langle q/m_0 \rangle > 300'000$ C/kg. Ionic liquids have also the advantage to have no measurable vapor pressure, good electrical conductivity and they can be sprayed applying positive or negative voltages. Basic research on beam characteristics was done by Lozano (2003) who analyzed the beam composition obtained with a spray from pulled silica needles with 5 μm inner diameter at very low flow rates (around 20 pico-liters per second) using formamide doped with sodium iodide (conductivity 2.15 S·m^{-1}) and the ionic liquid EMI-BF$_4$ (conductivity 1.4 S·m^{-1}). His results showed that the energy spread of particles in the beam decreases to a few eV for EMI-BF$_4$ and is thus comparable to liquid metal ion sources.

This small energy spread has been confirmed through follow-up analyzes of sprays obtained from porous tungsten needles (Lozano 2006). This collaboration, together with the NASA Jet Propulsion Laboratory, has resulted in the development of a space qualified colloid thruster in a short time, starting with a first breadboard in 2001 to a qualified flight model delivered to ESA in 2008 to fly on the LISA Pathfinder mission (Hruby *et al.* 2001, Ziemer *et al.* 2008, Demmons *et al.* 2008).

In parallel to the progress in electrospray technologies and fuels, the fast evolution of the semi-conductor industry and the development of novel microfabrication techniques, such as high aspect-ratio anisotropic etching of silicon (Laermer and Shilp 1994), has enabled the manufacture of large arrays of emitters. Early work on out-of-plane electrospray emitters without extraction electrodes has been carried out by Schultz *et al.* (2000). Their design featured a single silicon nozzle for electrospray mass spectrometry with 20 μm inner diameter and a standoff height of 50 μm. The test nozzles were operated with water solutions at a flow rate of 100 nL/min and a stable spray was provided by the nozzle for several hours.

An improved silicon nozzle has been developed by Griss *et al.* (2002). Their design features a sharp capillary tip obtained through a sequence of isotropic and anisotropic plasma etching steps. The tip dimensions are an outer diameter of 38 μm (at the base of the capillary) and an inner diameter of 18 μm with a standoff height of 70 μm. Their design also featured groves on the back side to glue directly a silica capillary onto the chip. The tips, intended for mass spectrometry (Sjödahl *et al.* 2003), were operated at 100 nL/min by means of a syringe pump and the results were compared to a conventional pulled capillary tip. The authors report a good robustness of the needle design and their operability during several runs for several months where they performed mass spectrometric analyzes.

Pioneering work on integrated capillary devices for spacecraft propulsion has been done by Paine (2002, 2004) at the University of Southampton. Unfortunately the low aspect ratio of his capillaries led to fuel leakage and his devices were not functional. He later joined the group of Prof. J. Stark at Queen Mary, University of London, who was also investigating electrospray thrusters for spacecraft propulsion (Stark *et al.* 2003, Kent *et al.* 2004). His group has developed a flow meter to measure the pressure drop along the fuel feed line (Smith 2005). This pressure difference is measured with quartz crystal resonators in which the frequency of oscillation varies with pressure-induced stress. The instrument's high sensitivity permits measuring flow rates in the range of 1 nL/s. This has allowed to study the dependence of volumetric flow rate on the applied voltage (Smith *et al.* 2006), the pulsation modes of electrosprays (Alexander *et al.* 2006) and the effects of molar conductivity on spray characteristics (Smith *et al.* 2005). In parallel to basic electrospray research the group at Queen Mary has developed and tested, in partnership with the Rutherford Appleton Laboratory, a high aspect ratio capillary emitter (Wang *et al.* 2007). The tests done with these devices, linear arrays of silicon dioxide nozzles having an inner diameter of 10 μm and 250 μm length, have shown their operability at flow rates of 100 nL/min and applied voltages ranging from 2.5 to 2.7 kV. To minimize wetting of

these microfabricated emitters the exterior of the capillaries was coated with materials having low surface energies (gold and conducting diamond-like-carbon).

Recent research work at the MIT was done on microfabricated externally wetted silicon emitters with integrated electrodes (Velásquez-García, 2004, 2006, Gassend, 2007, 2008). Externally wetted emitters cannot clog and naturally provide the necessary high fluid impedance to reach a purely ionic beam. The difficulty in this approach is to modify the silicon surface to allow surface to be wetted by the ionic liquid. Velásquez-García and Gassend developed a plasma etch procedure to create tiny silicon pillars on the surface of the wafer, also known as *black silicon*. Unfortunately this black silicon is difficult to reproduce from one batch to another and in consequence Legge and Lozano (2008) moved to alternative manufacturing procedures resulting in porous tungsten emitters. With their novel design they have obtained excellent manufacturing reproducibility and purely ionic beams.

1.3 Thesis objectives and novelty

Inspired by the works of Romero-Sanz *et al.* (2003) reporting a high charge-over-mass ratio spraying the ionic liquid EMI-BF$_4$ and by the successful spray experiments done by Schultz *et al.* (2000) and Griss *et al.* (2002) with micromachined out-of-plane single electrospray emitters, the objective of this thesis was to develop a microfabrication process for arrays of electrospray emitters, the necessary numerical design tools and a test bench to measure the performance of the thruster. The works resulted in a novel capillary type thruster composed of single or arrays of capillary emitters *with* integrated extractor electrodes. The integration and precise alignment of extractor electrodes into the design provides one individual extractor for each capillary emitter within an array and thus guarantees homogeneous spray characteristics for all emitters. To minimize crosstalk, provide thrust modulation and optimize the fabrication process a method to estimate the onset voltage of the emitters has been developed which is compatible with low aspect ratio structures as found in micromaching and can thus take into account electric field distortions by adjacent structures. The performance measurements show different spray characteristics ranging from droplet to ionic emissions, depending on the configuration. This flexibility in operation regimes allows to tailor the thruster to different mission requirements. A first life test demonstrating stable operation during several hours further validates the concept of such a thruster design.

1.4 Thesis structure

Chapter 1 has given an overview on electrospray thrusters by presenting its principle of operation and giving an account of past research and the present state-of-the-art of the technology. It also situates the work done in this thesis within the research efforts in the field.

Chapter 2 reviews the various modes of operation of a colloid thruster and summarizes the two most common current scaling laws. It also reviews the various requirements on thruster needed for formation flight missions such as the ESA/NASA Laser Interferometric Space Antenna (LISA). Based on observations done by other research groups a simple evaluation is done to verify if the basic requirements (thrust, power-to-thrust, specific impulse, among others) can be met. Chapter 1 and 2 are intended as review, whereas the remaining chapters are original to this thesis.

A novel method to determine the onset voltage of electrospray thrusters having complex geometries is presented in chapter 3. It combines analytical methods together with finite element modeling to determine the onset voltage of single of arrays of emitters. The chapter describes the method in detail and correlates it to results reported in literature.

Fabrication is discussed in chapter 4. It introduces the thruster's design and the process flows to manufacture the various elements. It also discusses process improvements to increase yield and post-processing steps to enhance thruster performance. The last part presents the packaging concept for the microfabricated silicon chips which are attached bonded to a multi-functional glass-ceramic interface.

Experimental results are presented in chapter 5. It first introduces the experimental methods and installations and discusses the results obtained with a first generation of devices and their correlation with the onset voltage model. Results obtained with the second generation of thrusters are then presented and discussed in the second part of the chapter.

Chapter 6 concludes this thesis and gives recommendations for future work.

Chapter 2

Electrospray Thruster System

Eᴸᴇᴄᴛʀᴏsᴘʀᴀʏ thrusters can be controlled by adjusting the mass flow rate or the applied voltage. The various resulting operating modes have been used in several applications such as mass spectrometry of large biomolecules (Fenn *et al.* 1989), surface modification and microfabrication (Zorzos and Lozano 2008), deposition of thin films (Jaworek 2007) and femto-liter drops (Paine *et al.* 2007), electrospinning of nanofibers (Reneker *et al.* 2000), and spacecraft propulsion, as introduced in chapter 1.

Electrospray thrusters offer great flexibility to spacecraft operators as they allow variations in the specific impulse and thrust. This chapter will investigate different aspects of electrospray thrusters mainly in the stable regime called the *cone-jet* mode. It will review Taylor's theory of the equipotential cone, semi-empirical scaling laws to predict spray current and jet diameter in cone-jet mode and discuss the target thruster performance parameters that should be reached for the electrospray thruster system to be competitive with other electric propulsion technologies.

2.1   Electrospray operation

Although the principle of operation of an electrospray is fairly simple (Sec. 1.1) the underlying physics is complex. Cloupeau and Prunet-Foch (1990) observed and classified the various modes of operation of electrosprays based on visual observation of the emitter region. The observed regimes include dripping, microdripping, cone-jet, ramified jet, spindle and pulsating modes (some examples are sketched in figure 2.1). For propulsion applications the most interesting is the stable cone-jet mode which, under certain conditions, emits droplets, a mix of droplets and ions, or solely ions.

When spraying in cone-jet mode a mix between droplet and ionic emissions starts to appear for liquids with conductivities above 0.8 S·m^{-1}. Gamero-Castaño and
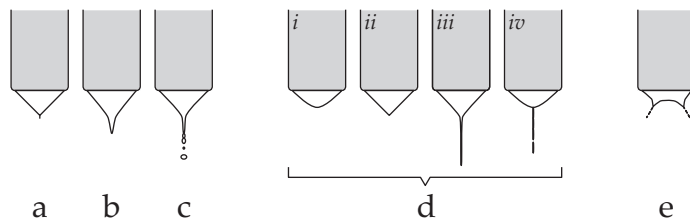
Figure 2.1: Sketches of different electrospray modes. (a)-(c) Variations of the cone-jet ranging from purely ionic spray to an elongated spray with droplet emissions, (d) pulsating mode, the liquid cone forms at the tip of the capillary, ejects droplets, retracts and restarts, and (e) multi-jet mode, several conic emission sites exist.

Fernández de la Mora (2000) show that the maximum electric field occurs at the transition region between the liquid cone and the jet or in the jet breakup region. Energy measurements in spray experiments with capillary emitters using the ionic liquid EMI-Tf$_2$N indicate that most of these ionic emissions occur at the jet breakup (Gamero-Castaño 2008a).

Purely ionic emissions have first been observed by Romero-Sanz $et\ al.$ (2003) while performing capillary spray tests at very low flow rates with the ionic liquid EMI-BF$_4$. Lozano (2006) has demonstrated, using needle sources, that for $Ionic$ $Liquid\ Ion\ Sources$ (ILIS) energy deficits below 7 eV and energy spreads of less than 8 eV (FWHM – full width at half maximum) can be achieved, similar to liquid metal ion sources used in $Focused\ Ion\ Beam$ (FIB) applications.

For the remainder of this section we will focus mainly on droplet regime and the purely ionic mode. The physics underlying mixed mode emissions is still poorly understood and will only be discussed qualitatively hereafter. Factors influencing the electrospray performance include:

- geometry of the emitter and electrodes;

- liquid flow rate (active pumping or passive flow);

- applied voltages;

- flow resistance;

- liquid properties (surface tension, conductivity, viscosity, among others);

- electrode dimensions and materials.

Experiments done by Lozano (2006) and Castro $et\ al.$ (2007) with needle emitters show that the nature of the source, in particular its flow impedance, plays an additional role. They observe an ionic spray with EMI-Tf$_2$N, a liquid having a relatively low conductivity (0.88 S·m^{-1}) and surface tension (34.9 dyn·cm^{-1}). On the other hand Gamero-Castaño (2008a) identifies the presence of droplets in the beam using the same ionic liquid but spraying from a capillary emitter.

2.1.1 Taylor cone

The first theoretical model of the conic shape of the liquid has been given by Taylor (1964). He assumed the liquid to be a perfect conductor and postulated that the cone resulted from an equilibrium between surface tension forces and the electrostatic stress on the liquid's surface. The surface tension stress at a point on the liquid surface can be calculated using the Young-Laplace equation

$$\sigma_\gamma = \gamma \left(\frac{1}{r_1} + \frac{1}{r_2} \right) \tag{2.1}$$

where r_1 and r_2 are the principal radii of curvature of the meniscus and γ is the surface tension of the liquid. For a cone the curvature is $r_1 = \cot \beta / r$, where β is the cone half angle, r is the radial coordinate from the apex of the cone, while the second radius of curvature is infinite ($r_2 \to \infty$). The surface stress can thus be written as

$$\sigma_\gamma = \frac{\gamma \cot \beta}{r} \tag{2.2}$$

The electrical stress on the surface of the conducting liquid is given by the Maxwell stress tensor (Landau *et al.* 1984):

$$\sigma_E = -\epsilon_0 \left(\frac{1}{2} \vec{E}^2 \delta_{nt} - E_n E_t \right) \tag{2.3}$$

where $\vec{E}$ is the electrical field, E_n and E_t its normal and tangential components, ϵ_0 the permittivity of free space and δ_{nt} the Kronecker delta. On the surface of an equipotential liquid the field $\vec{E}$ has no tangential component therefore equation 2.3 results into

$$\sigma_E = \frac{1}{2} \epsilon_0 E_n^2. \tag{2.4}$$

In the case of a static liquid cone the electrostatic stress balances the surface tension

$$\gamma \frac{\cot \beta}{r} = \frac{1}{2} \epsilon_0 E_n^2. \tag{2.5}$$

In spherical coordinates the Laplace equation can be written as (assuming symmetry about ϕ)

$$\nabla^2 \Phi = \frac{1}{r^2} \frac{\partial}{\partial r} \left(r^2 \frac{\partial \Phi}{\partial r} \right) + \frac{1}{r^2 \sin \theta} \frac{\partial}{\partial \theta} \left(\sin \theta \frac{\partial \Phi}{\partial \theta} \right). \tag{2.6}$$

In the case of a conic the behavior of the potential near $r = 0$ can be written in terms of the Legendre polynomial (Jackson 1999)

$$\Phi(r, \theta) \cong A r^\nu P_\nu(\cos \theta). \tag{2.7}$$

Finally the normal field, the potentials gradient, is determined

$$E_n = -\frac{1}{r} \frac{\partial \Phi}{\partial \theta} \cong A r^{\nu-1} \sin \theta \frac{dP_\nu}{d(\cos \theta)}(\cos \theta). \tag{2.8}$$

To insert the normal electrical field of equation 2.8 into the equilibrium expression 2.4

it is necessary for the exponent to be $\nu = 1/2$. The potential field 2.7 is therefore:

$$\Phi = Ar^{1/2}P_{1/2}(\cos\theta) \tag{2.9}$$

The initial hypothesis of an equipotential conic surface, or in other terms a constant potential for all r on $\theta_0 = \pi - \beta$ results in the condition

$$P_{1/2}(\cos\theta_0) = 0 \tag{2.10}$$

The condition above is met for a cone half-angle of $\beta = 49.29°$. In electrosprays the observations deviate from the Taylor cone angle, as space charge and the jet will have an effect on the cone angle. Nevertheless some remarkable TEM observations of the liquid cone for liquid metal ion sources made by Driesel *et al.* (1996*b*, 1996*a*) have shown that for certain liquid metals, spraying at low currents, the cone half-angle is very close to the one predicted by Taylor.

2.1.2 Onset voltage

When applying a potential difference between an emitter and an extractor electrode no spray current will be measured. Once a sufficiently large potential is reached emission sets in and a spray current can be measured (figure 2.2a). This threshold potential is known as the *onset voltage*, an analogous potential exists for spray extinction called the *extinction voltage*.

A common model to determine the onset voltage of long slender needles assumes a hyperbolic surface facing a flat plate, as shown in figure 2.2b. It assumes that once a threshold field is reached the liquid snaps-over to a Taylor cone and emission starts. In this model the threshold field at the tip of the hyperboloid surface is defined as the equilibrium between the electrical stress pulling the liquid toward the electrode, σ_{E_t}, and the the surface tension, σ_{γ_t}, pulling the liquid back to the needle (Martínez-Sánchez 2004).

$$\sigma_{E_t} \geq \sigma_{\gamma_t} \tag{2.11}$$

As previously seen the surface tension stress at a point on a liquid surface can be calculated using the Young-Laplace equation. At the tip of a hyperboloid surface both radii are identical, r_t, and equation 2.1 simplifies into

$$\sigma_{\gamma_t} = \frac{2\gamma}{r_t} \tag{2.12}$$

The electrical stress on the surface of the conducting liquid in absence of tangential stress has been derived previously in equation 2.4.

The absence of space charge allows writing the well-known relationships between
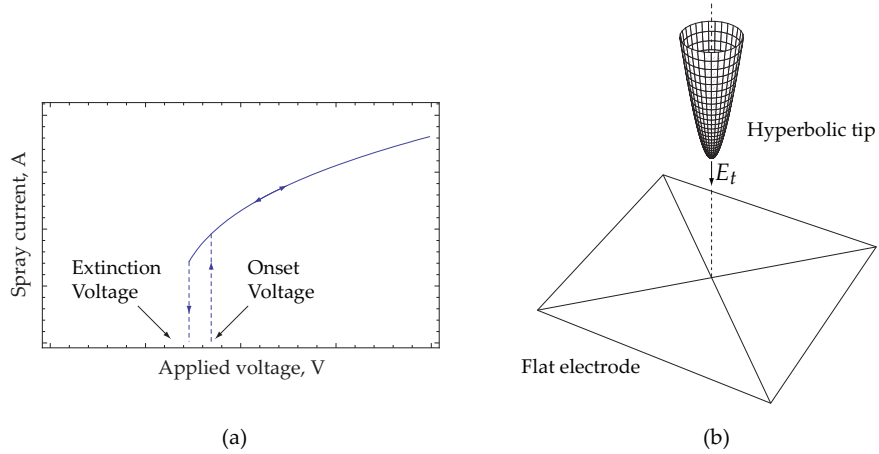
Figure 2.2: (a) Graph illustrating the current vs. voltage characteristics of an electrospray source. The voltage at which a spray sets in (a current is measured) is known as the onset voltage, while emissions stop at the extinction voltage. (b) Sketch of a hyperboloid tip facing a flat electrode.

electric potential, Φ, and field, $\vec{E}$

$$\nabla^2 \Phi(x, y, z) = 0 \tag{2.13}$$

$$\vec{E} = -\vec{\nabla}\Phi. \tag{2.14}$$

The boundary conditions, in the case of this model, are the hyperboloid surface and an infinite plate facing it (fig 2.2). To allow for a simple analytic solution this geometry is modeled in a prolate spheroidal coordinate system.

The prolate-spheroidal coordinate system is defined as (Abramowitz and Stegun 1964)

$$
\begin{aligned}
x &= \alpha \sinh \xi \sin \eta \cos \phi \\
y &= \alpha \sinh \xi \sin \eta \sin \phi \\
z &= \alpha \cosh \xi \cos \eta
\end{aligned}
\tag{2.15}
$$

where $\xi \in [0, \infty)$, $\eta \in [0, \pi]$, and $\phi \in [0, 2\pi)$. The constant α represents one-half the distance between the hyperboli foci (fig. 2.3). In this coordinate system surfaces having constant ξ are prolate-spheroidal, whereas those with constant η are hyperboloid surfaces. By performing the variable transformations $u = \cosh \xi$, $v = \cos \eta$ and $w = \phi$ an alternate form is obtained

$$
\begin{aligned}
x &= \alpha\sqrt{(u^2 - 1)(1 - v^2)} \cos w \\
y &= \alpha\sqrt{(u^2 - 1)(1 - v^2)} \sin w \\
z &= \alpha\, u\, v
\end{aligned}
\tag{2.16}
$$
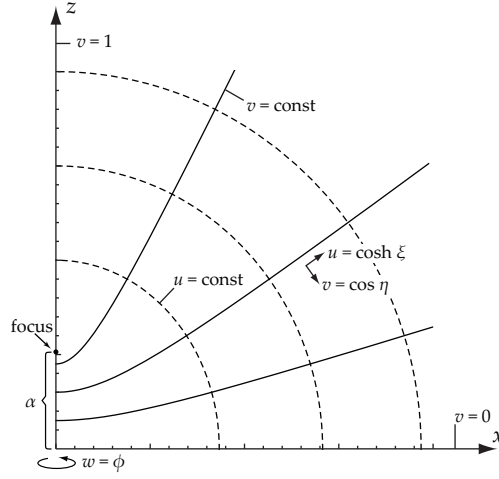
Figure 2.3: Illustration of the prolate spheroidal coordinate system (projection onto the x-z plane). The coordinate w defines the angular position around the z-axis. Surfaces with constant u are prolate-spheroid surfaces, whereas surfaces with constant v describe hyperboloid surfaces. The constant α represents one-half the distance between the hyperbolic foci.

where $u \in [1, \infty)$, $v \in [-1, 1]$, and $w \in [0, 2\pi)$. The scale factors (Boas 2006) are

$$
\begin{aligned}
h_u &= \alpha \sqrt{\frac{u^2 - v^2}{u^2 - 1}} \\
h_v &= \alpha \sqrt{\frac{u^2 - v^2}{1 - v^2}} \\
h_w &= \alpha \sqrt{(u^2 - 1)(1 - v^2)}
\end{aligned}
\tag{2.17}
$$

For the prolate-spheroidal coordinates the Laplacian is written as

$$
\begin{aligned}
\nabla^2 \Phi &= \frac{1}{\alpha^2} \frac{1}{u^2 - v^2} \frac{\partial}{\partial u}\left[(u^2 - 1)\frac{\partial \Phi}{\partial u}\right] \\
&+ \frac{1}{\alpha^2} \frac{1}{u^2 - v^2} \frac{\partial}{\partial v}\left[(1 - v^2)\frac{\partial \Phi}{\partial v}\right] \\
&+ \frac{1}{\alpha^2} \frac{1}{(u^2 - 1)(1 - v^2)} \frac{\partial^2 \Phi}{\partial w^2}.
\end{aligned}
\tag{2.18}
$$

The tip is modeled by a constant v_0 and represents a hyperboloidal surface where the partial derivatives of the potential in the other two directions are zero.

$$
\begin{aligned}
\frac{\partial \Phi}{\partial u} &= 0 \\
\frac{\partial \Phi}{\partial w} &= 0.
\end{aligned}
\tag{2.19}
$$

Equation 2.13 can now be simplified into

$$0 = \frac{\partial}{\partial v}\left[(1-v^2)\frac{\partial \Phi}{\partial v}\right] \tag{2.20}$$

The solution of this equation, with the boundary conditions $\Phi(v_0) = \Phi_0$ and $\Phi(0) = 0$ yields

$$\Phi(v) = \Phi_0 \frac{\ln\frac{1+v}{1-v}}{\ln\frac{1+v_0}{1-v_0}}. \tag{2.21}$$

The electric field can now be calculated (Boas 2006)

$$\mathbf{E} = -\nabla\Phi = -\frac{1}{h_2}\frac{\partial \Phi}{\partial v} = -\frac{2\Phi_0}{\alpha\sqrt{1-v^2}\sqrt{u^2-v^2}\log\frac{1+v_0}{1-v_0}} \tag{2.22}$$

The radius of curvature r at a point (x, y) on a curve in cartesian coordinates given by (Bronstein *et al.* 2005)

$$r = \frac{\left[1 + (f'(x))^2\right]^{\frac{3}{2}}}{f''(x)} \tag{2.23}$$

Due to the symmetry of the hyperboloid the radius of curvature at the apex, r_a can be calculated considering a simple curve in the x-z plane, i.e. $w = 0$. For $v = v_0$. The function $f(x)$ is written as

$$f(x) = \frac{\sqrt{\alpha^2(1-v_0^2) - x^2}}{\sqrt{1-v_0^2}} \tag{2.24}$$

The radius at the tip of the needle, $x = 0$, is therefore

$$r_t = \frac{\alpha(1-v_0^2)}{v_0} \tag{2.25}$$

The distance from origin to the hyperboloid tip is directly derived from equation 2.16

$$d = \alpha v_0. \tag{2.26}$$

The electrical field at the tip of the hyperboloid defined by $v = v_0$ can now be found by substituting the variables α and v_0 with r_t and d

$$E_t = \frac{2\Phi_0\sqrt{1 + \frac{r_t}{d}}}{r_t \ln\left[\frac{r_t + 2d + 2\sqrt{d(d+r_t)}}{r_t}\right]}. \tag{2.27}$$

By substituting 2.12, 2.5, 2.27 into 2.11 an expression for the onset voltage V_{oc} can be found

$$V_{oc} = \sqrt{\frac{\gamma r_t}{\epsilon_0}} \cdot \frac{\ln\left[\frac{r_t + 2d + 2\sqrt{d(d+r_t)}}{r_t}\right]}{\sqrt{1 + \frac{r_t}{d}}} \tag{2.28}$$

Equation 2.28 does assume a snap-over behavior of the liquid. Its use should be limited to long needles with no structures surrounding the tip. It is important to notice that a change in distance, d, or tip radius, r_t, leads to the change of the cone half angle, as these two parameters define v_0. Consequently for a fixed tip radius r_t
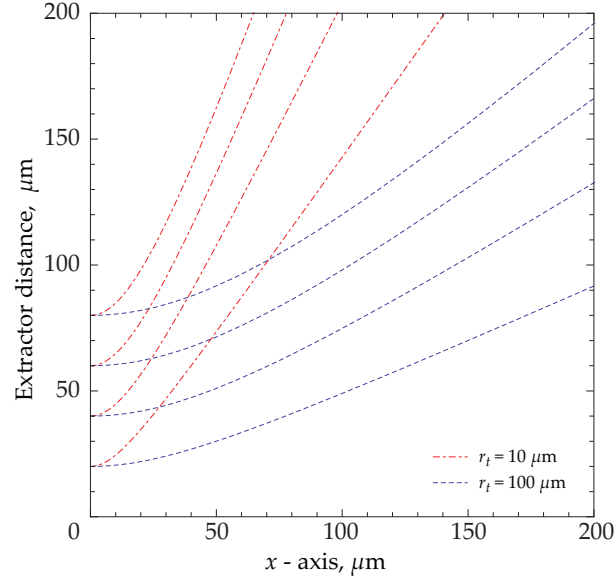
Figure 2.4: Projection of the hyperboloid surface onto the x-z plane. The electrode is placed at $z = 0$. The variation in tip geometry is shown for two tip radii, 10 μm and 100 μm. For small electrode-tip distances, d, the change of the asymptote angle is clearly visible.

and increasing extractor-tip distance, d, the asymptotic angle becomes very large and the hyperboloid surface starts to resemble more a sharp needle

$$\lim_{d \to \infty} v_0(d, r_t) = \lim_{d \to \infty} \sqrt{\frac{d}{d + r_t}} = 1. \tag{2.29}$$

This dependence is illustrated in Figure 2.4 for the tip radii of 10 μm and 100 μm. For a change in distance from the origin a variation in the asymptote angle is observed.

Finally for large tip to extractor distances, $d \gg r_t$, the expression for the onset voltage (equation 2.28) can be simplified into

$$V_{oc} = \sqrt{\frac{\gamma r_t}{\epsilon_0}} \cdot \ln\left[\frac{4d}{r_t}\right]. \tag{2.30}$$

2.1.3 Cone-jet mode - scaling laws of the droplet regime

Scaling laws for spray current and jet diameter have been derived by Fernández de la Mora and Loscertales (1994) for electrosprays operating in droplet mode. Their model is based on the hypothesis that the equipotential conic surface described by Taylor is maintained up to a meniscus cross section at which the charge relaxation time

$$t_e = \frac{\epsilon \epsilon_0}{K}, \tag{2.31}$$

(a)   (b)

Figure 2.5: Drawing of the cone-jet transition region illustrating (a) the mixed ion-droplet mode, (b) ionic mode.
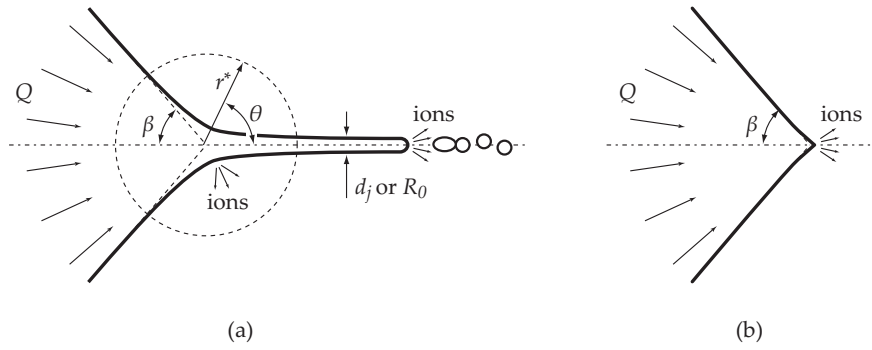
becomes comparable to the liquid convection time (assuming a sink flow)

$$t_h \approx \frac{r^3}{Q}, \tag{2.32}$$

where ϵ is the dielectric constant of the liquid, Q the flow rate, K conductivity and r the radial coordinate (fig 2.5). The dimension of the transition region can be found by equating 2.31 and 2.32 and solving for r:

$$r^* = \left(\frac{\epsilon \epsilon_0 Q}{K}\right)^{\frac{1}{3}}, \tag{2.33}$$

where r^* is the characteristic length at which the removed charges cannot be compensated by bulk conduction, the Taylor equilibrium cannot be maintained anymore and the liquid transitions into a jet. In the transition region the current ceases to be carried mainly by bulk conduction but transitions to the surface where it is transported by surface convection of the liquid jet.

In the transition region the surface current is of the order of $I_s \propto (\gamma K Q/\epsilon)^{1/2}$. In a recent review paper Fernández de la Mora (2007) summarizes the derived scaling laws for current, I, and jet diameter, d_j:

$$I = g(\epsilon)\,(\gamma K Q)^{1/2} \tag{2.34}$$

$$d_j = G(\epsilon) r^* \tag{2.35}$$

where g and G are empirical parameters depending on the dielectric constant of the liquid. At first it might surprise that the voltage does not play a role in the emission current, but as discussed previously, as the meniscus cross section becomes small enough the liquid moves through it at high speeds and the finite electric conductivity is not able to replace the removed charges. An equipotential surface cannot be established and a jet forms. Fernández de la Mora and Loscertales (1994) further

introduce a dimensionless flow rate and define it as

$$\eta = \left(\frac{\rho K Q}{\gamma \epsilon \epsilon_0} \right)^{1/2}.$$

(2.36)

Experimental findings show that the minimum flow rate, at which the cone becomes instable, is around $\eta = 1$.

$$Q_{min} \approx \frac{\gamma \epsilon \epsilon_0}{\rho K}$$

(2.37)

The existence of such a minimum flow rate could have an impact on whether a liquid can reach the purely ionic mode or not. Figure 2.6a plots the characteristic radius, based on equation 2.33, as a function of the volumetric flow rate for three different conductivities. The chosen liquid parameters and conductivities correspond to different solutions of Triethylene Glycol (TEG) doped with sodium iodide (NaI) as used in experiments by Smith *et al.* (2006). The apex radius corresponding to a critical electric field of 1 V/nm, the necessary field strength for ions to evaporate from the surface (Gamero-Castaño and Fernández de la Mora 2000, Takahashi and Lozano 2008), has been calculated, using equations 2.4 and 2.1, and has been marked by a horizontal line in the plot. The minimum flow rate, Q_{min}, calculated using equation 2.37 is indicated for each liquid with a vertical line. The graph shows that ionic mode with doped TEG is not possible as the cone will become unstable before reaching the critical field strength at the cone apex. The situation is different for higher conductivity liquids as the computation of the characteristic radius using the liquid properties of the ionic liquids EMI-BF$_4$ and EMI-Tf$_2$N shows. The results, shown in figure 2.6b, illustrate that the critical electric field at the cone apex is reached before Q_{min}, therefore evaporation of ions should be possible.

Alternative scaling laws have been introduced by Gañán Calvo in several papers (1994, 1997). A recent paper compiles these laws for liquids of very different nature (Gañán Calvo 2004) and will be briefly summarized hereafter. To classify the various liquids two non-dimensional parameters are introduced. The first one corresponds to a non dimensional flow rate and is defined as

$$\alpha_\rho = \frac{Q}{Q_0} = \frac{\rho K Q}{\gamma \epsilon_0}.$$

(2.38)

The second non-dimensional parameter indicates the relation between viscous and inertial effects in the liquid

$$\alpha_\mu = \frac{Q}{Q_0} \frac{1}{\delta_\mu^3} = \frac{K^2 \mu^3 Q}{\epsilon_0^2 \gamma^3},$$

(2.39)

where δ_μ is the viscous dimensionless parameter (Gañán Calvo *et al.* 1997)

$$\delta_\mu = \frac{\rho Q_0}{\mu R_0} = \left(\frac{\rho \epsilon_0 \gamma^2}{K \mu^3} \right)^{\frac{1}{3}}.$$

(2.40)

In this expression the function Q_0, called the characteristic flow rate, is of the order of the minimum flow rate (defined in equation 2.37), while R_0 is postulated to be in
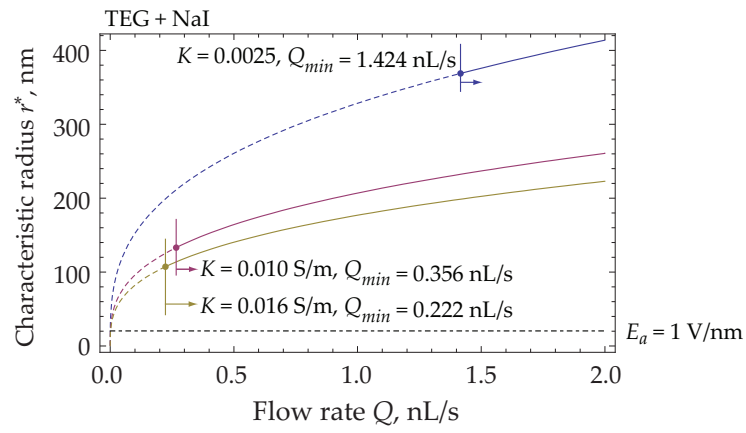
(a)
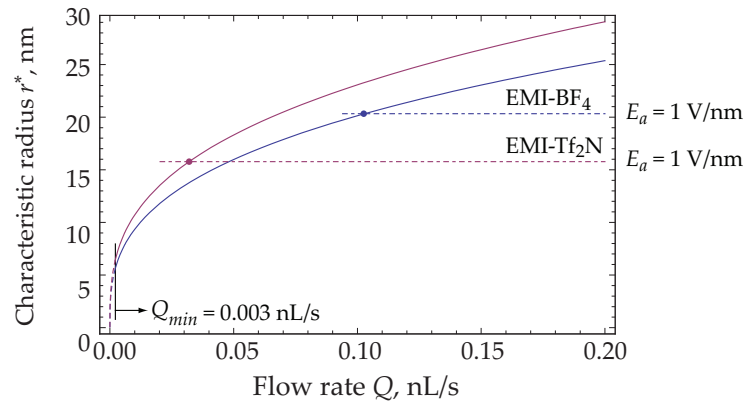
(b)

Figure 2.6: Critical radius, r^*, vs. volumetric flow rate computed using equation 2.33. (a) Plot corresponding to three TEG+NaI solutions with conductivites of 0.0025, 0.010 and 0.016 S·m^{-1}. The minimum flow rate, Q_{min}, for these solutions (vertical lines) is reached well before the curves cross the critical field of 1 V·nm^{-1} (horizontal line) necessary for ion evaporation to set in. Consequently ionic mode can most likely not be reached with these solutions. (b) Same plot using liquid properties corresponding to the ionic liquids EMI-BF$_4$ and EMI-Tf$_2$N, in this case the critical field is reached at higher flow rates than Q_{min}, thus an ionic regime should exist.

the order of the jet diameter

$$Q_0 \quad = \quad \frac{\gamma \epsilon_0}{\rho K} \tag{2.41}$$

$$R_0 \quad = \quad \left(\frac{\gamma \epsilon_0^2}{\rho K^2} \right)^{\frac{1}{3}}. \tag{2.42}$$

The scaling laws discussed by Gañán Calvo depend on the liquid properties and are expressed in terms of validity domains for the parameters α_μ and α_ρ. The most common regime is the one for which inertia and electrostatic effects dominate (IE-scaling), in this regime the current is

$$I = (\gamma K Q)^{1/2}, \tag{2.43}$$

and the regimes validity limits are defined by

$$\alpha_\rho \gg \alpha_\mu^{1/4}, \; \alpha_\rho/(\epsilon - 1) \gg 1. \tag{2.44}$$

For polar liquids where inertia and polarization forces are important (IP-scaling) the current scales as

$$I = \left(\frac{\rho K^2 Q^2}{(\epsilon - 1)\epsilon_0} \right)^{1/2} \tag{2.45}$$

and the required conditions are

$$1 \gg \frac{\alpha_\rho}{(\epsilon - 1)} \gg \frac{\alpha_\mu}{(\epsilon - 1)^4}. \tag{2.46}$$

As this mode corresponds to a parameter $\eta < 1$ it has only been observed for a few liquids such as water or formamide.

The current in a third region where viscous forces and polarization forces dominate (VP-scaling) is defined as

$$I = \left(\frac{\mu^3 K^3 Q^2}{(\epsilon - 1)^4 \gamma^2 \epsilon_0^2} \right)^{1/2} \tag{2.47}$$

with a validity range of

$$\frac{\alpha_\rho}{(\epsilon - 1)} \ll \frac{\alpha_\mu}{(\epsilon - 1)^4} \ll 1. \tag{2.48}$$

The fourth reported regime where viscous forces and electrostatic suction dominate (VE-scaling) has the the same current scaling laws as IE-scaling and will not be considered hereafter. Figure 2.7 plots different liquids in the parameter space defined by Gañán Calvo. For this example the flow rate input are multiples (n=1,2,...,10) of the minimum flow rate Q_{min} of different liquids reported in literature. For the reasons previously mentioned no liquid can be found in the IP region as values in the region would require a $Q < Q_{min}$ (in experiments lower flow rates have been observed for water and formamide). It is also unlikely that the ionic liquids EMI-BF$_4$ and EMI-Tf$_2$N can reach flow rates close to $\eta = 1$ as the required critical radii, r^*, would be well below the necessary cone apex radius yielding a strong enough electric field to initiate field evaporation of ions (as discussed in figure 2.6).
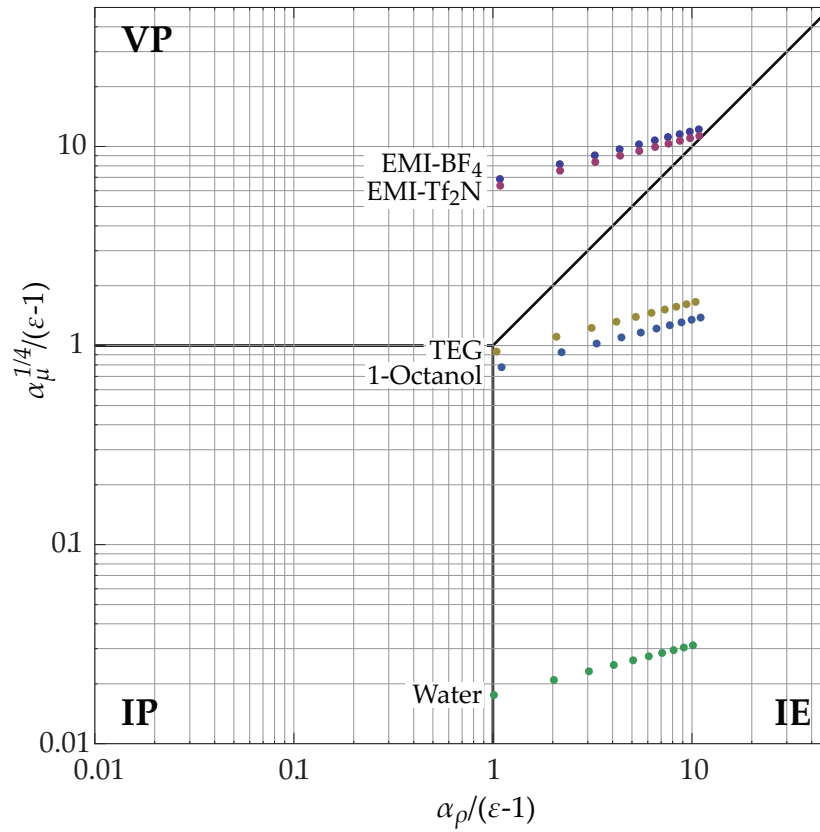
Figure 2.7: Five different liquids have been plotted in the parameter subspaces defined by Gañán-Calvo. The flow rates used to compute α_ρ and α_μ are multiples $(Q = n \cdot Q_{min})$ of the minimum flow rate $\eta = 1$ defined in equation 2.37.

Table 2.1: Properties of several solvents used as input parameters for figure 2.7

	EMI-BF$_4$[a]	EMI-Tf$_2$N[a]	1-Octanol[b]	TEG[b]	Water[b]
γ (dyn/cm)	45.2	34.9	26.1	45.2	72.58
K (S·m^{-1})	1.4	0.88	$1.16 \cdot 10^{-3}$	$4.38 \cdot 10^{-3}$	$2.15 \cdot 10^{-3}$
ϵ	12.9[c]	12.2[c]	10.34	23.69	80.1
μ (cP)	38	34	10.64	49.0	1.0019
ρ (g·cm^{-3})	1.24	1.52	0.8255	1.123	0.9982

[a] Garoz *et al.* (2007)
[b] Fernández de la Mora and Loscertales (1994)
[c] Kobrak (2008)

At present both scaling laws have shown to yield acceptable results within their respective validity range. Nevertheless for electrosprays using high conductivity liquids, such as ionic liquids, these results have not been validated yet. Further at low flow rates the current scaling laws might be quite different as ions and solvated ions are sprayed. In any case the maximum current does not exceed

$$I < I_{max} = nqQ, \tag{2.49}$$

where n represents the number density of ions, q the charge and Q the flow rate. In the case of ionic liquids the entire liquid consists of cations and anions and n can be expressed in terms of the cations or anions mass, m_0, and the liquid's density, ρ:

$$n = \frac{1}{2} m_0 \rho \tag{2.50}$$

The factor $1/2$ takes into account the fact that half of the liquid consists of anions and the other of cations. According to Fernández de la Mora (2007) this charge separation equation holds in all cases against experimental data.

It should also be mentioned that a significant influence of the applied voltage at low flow rates has been measured by Smith *et al.* (2006) who have observed, using a online flow rate measurement system, the effects of the voltage on the flow rate spraying a triethylene glycol (TEG) solution doped with sodium iodide (NaI). In their experiments they record a variation of 25% per kilovolt for a flow rate of 4 nL/s whereas variations fall well below 5% for flow rates above 20 nL/s.

2.1.4 Ionic and mixed drop-ion regime

Romero-Sanz *et al.* (2003) have performed time-of-flight measurements spraying the ionic liquid EMI-BF$_4$ and observed, for decreasing flow rates, an increase of the ionic current (in contrast to droplets) in the beam. Similar observations were done by Chiu *et al.* (2005) who have identified, operating at "low flow rates", an ionic beam through TOF and mass spectrometry. The current vs. mass flow rate recorded in their experiments are illustrated in figure 2.8. As the flow rate increases the ionic current goes through a maximum while the drop current increases steadily.

Gamero-Castaño and Fernández de la Mora (2000) have observed, for various concentrations of NaI dissolved in formamide ($K = 0.21 - 3.00$ S·m^{-1}), a sharp increase in current for flow rates below Q_{min}. At Q_{min} they compute an electric field of 0.96 V/nm, which corresponds to the critical value for ion evaporation to set in. Molecular dynamic simulations by Takahashi and Lozano (2008) on ion emissions from a EMI-BF$_4$ 'drop' exposed to an electric field also show that for fields above 1 V/nm emission of monomers, dimers and trimers occurs.

Mixed mode emissions have also been reported by Guerreo *et al.* (2007) while studying the spray properties of propylene carbonate (PC) doped with the ionic liquids EMI-BF$_4$ and EMI-Tf$_2$N. In their experiments they observed an evolution from purely colloidal regime to an almost purely ionic regime when decreasing the flow rate.
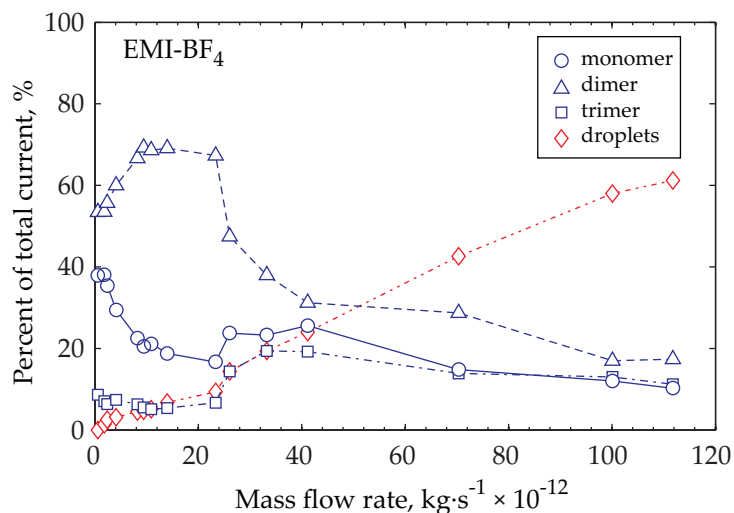
Figure 2.8: Repartition of the monomer, dimer, trimer and droplets in the total current of an EMI-BF$_4$ capillary spray (Romero-Sanz *et al.* 2003). As the mass flow rate increases the droplet current increases while ionic current decreases.

Measurement of very large solvated ions were done with a QSTAR mass spectrometry system capable to capture mass over charge ratios (m/q) up to 40'000 amu (Jhuree *et al.* 2007). Similar to the current vs. flowrate measurements done by Gamero-Castaño and Fernández de la Mora these current vs. voltage measurements show a minimum in the current as the voltage is increased and an increase of the mass over charge ratio for larger voltages.

These observations lead to the hypothesis that for low flow rates the current is mainly composed of ionic species and behaves linearly as suggested by equation 2.49. When increasing the flow rate (or the voltage) a transition region appears where a mix of ions and droplets is expelled to finally follow a square-root law for which the drop current is dominant (equation 2.34).

Needle type emitters, also called *Ionic Liquid Ion Sources* (ILIS), emit no droplets. These sources are externally wetted and exhibit a very large fluid impedance. Lozano (2006) and Castro *et al.* (2007) have used porous tungsten needles as sources and have observed ionic sprays over a large range of voltages. In particular the measured energy properties of these beams seem to be comparable to liquid metal ion sources. Lozano (2006) reports an energy deficit, i.e. the energy loss due to the ionization mechanism, below 7 eV and a narrow energy distribution with a FWHM of about 7±1 eV. Figure 2.9 compares the energy density distributions recorded by Lozano (2006) with a needle and by Gamero-Castaño (2008a) with a capillary emitter spraying EMI-Tf$_2$N. Time-of-flight spectra for 2.9a show an ionic beam, whereas a mixed droplet-ionic regime is observed for 2.9b.

Table 2.2 summarizes the different ionic liquids that have been shown to operate in ionic mode. Martino *et al.* (2006) argue that for a liquid to reach ionic mode a
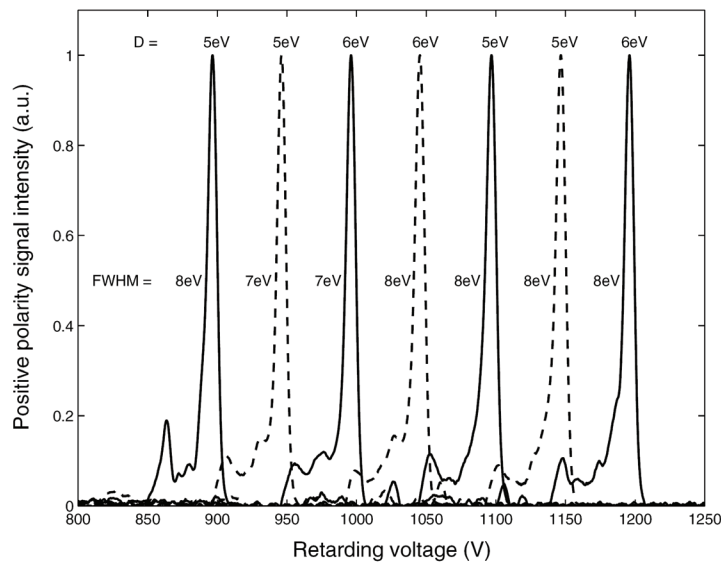
(a)
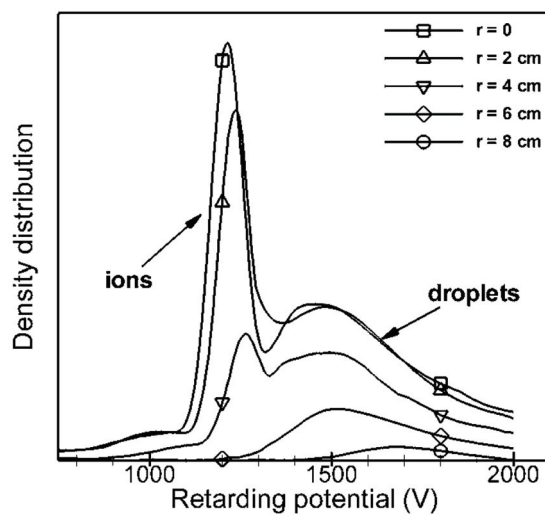
(b)

Figure 2.9: Energy density distribution measurements for EMI-Tf$_2$N sprays. (a) shows the result for a needle type emitter in ionic mode with emitter voltages from 900 to 1200 V increasing the voltage by steps of 50 V (from Lozano 2006). The trace was recorded with a high resolution retarding potential analyzer placed 104 mm from the extractor electrode. (b) shows the results for a capillary type emitter spraying in mixed ionic-droplet mode the emitter voltage was 1700 V the measurements were taken at an increasing separation from the beam axis (from Gamero-Castaño 2008*a*).

Table 2.2: Properties of ionic liquids for which the ionic regime has been observed. The parameters are γ surface tension, ρ density, K conductivity, T_m melting point. Available literature is organized for capillary and needle geometry. Cations: EMI=1-ethyl-3-methylimidazolium; BMI=1-butyl-3-methylimidazolium; C_6MI=1-hexyl-3-methylimidazolium. Anions: $Tf_2N = (CF_3SO_2)_2N$

Ionic liquid	γ (dyn·cm^{-1}) (21-23 °C)	ρ (g·cm^{-3}) (20 °C)	K (S·m^{-1}) (25 °C)	T_m (°C)	emitter geom. cap.	needle
EMI-BF$_4$	45.2[a]	1.24[a]	1.4[a]	12[b]	a,d,e	b,c
EMI-GaCl$_4$	48.6[a]	1.53[a]	2.2[a]	11[c]	a	c
EMI-C(CN)$_2$	47.9[a]	1.11[a]	2.2[a]	-11[c]	a	c
EMI-N(CN)$_2$	49.05[a]	1.08[a]	2.8[a]	-12[c]	a	c
BMI-FeBr$_4$	47.1[c]	1.98[c]	0.55[c]	-2[c]		c
C$_6$MI-FeBr$_4$	42.01[c]	1.86[c]	0.28[c]	-82[c]		c
C$_6$MI-FeCl$_4$	39.37[c]	1.33[c]	0.47[c]	-86[c]		c
EMI-Tf$_2$N	34.9[a]	1.52[a]	0.88[a]	4[b]	f	g

[a] Garoz *et al.* (2007)
[b] Lozano and Martínez-Sánchez (2005*a*)
[c] Castro *et al.* (2007)
[d] Romero-Sanz *et al.* (2003)
[e] Chiu *et al.* (2005)
[f] Gamero-Castaño (2008*a*)
[g] Lozano (2006)

high surface tension (> 30 dyn·cm^{-1}) and conductivity (> 1 S·m^{-1}) are necessary, a hypothesis which is confirmed so far by experiments in the case of capillary emitters (Garoz *et al.* 2007).

2.2 Missions and performance requirements

Future missions, such as the joint ESA / NASA Laser Interferometer Space Antenna (LISA), consist of spacecraft constellations in which each satellite is positioned with nanometer precision and requires micro- to millinewton thrust. Table 2.3 summarizes some of the key requirements for LISA. On the other hand micro- and nano-satellites require light-weight and efficient propulsion systems. For both mission types electrospray thrusters are interesting candidates.

2.2.1 Specific impulse

Measurements with single electrospray emitters have shown that a thrust below 1 μN can be generated (Stark *et al.* 2005, Ziemer *et al.* 2005, Guerreo *et al.* 2007). The measure of energy content in the fuel and its conversion efficiency into thrust is called

Table 2.3: Performance requirements for a propulsions system on a mission such as the ESA/NASA Laser Interferometer Space Antenna.

Parameter	Value
Thrust	1 μN - 1mN
Thrust noise	$< 0.1~\mu\text{N}/\text{Hz}^{1/2}$
Noise bandwidth	10^{-2} - 10 Hz
Power to thrust ratio	< 80 W/mN (for Isp=8000 s)
Mass	minimize
Isp	> 8000 s
Thrust resolution	$< 0.1~\mu$N
Minimum impulse bit	$< 10^{-9}$ N/s
Thrust linearity	$< 4~\mu\text{N} \pm 4\%$
Thrust repeatability	$< 0.5~\mu\text{N} \pm 0.5\%$
Lifetime	$>10'000$ hours
Thrust vector instability	minimze

specific impulse and is defined by

$$I_{sp} \equiv \frac{T}{\dot{m}g_0} = \frac{v_e}{g_0} \tag{2.51}$$

where T is the thrust, $\dot{m}$ is the mass flow rate, v_e the exhaust speed and g_0 the gravitational acceleration on earth. For an electric propulsion system the exhaust speed can be obtained by calculating the kinetic energy of a particle being accelerated by a potential difference, Φ_B (Jahn 1968)

$$v_e = \sqrt{2\Phi_B \frac{q}{m_0}} \tag{2.52}$$

where q/m_0 is the charge over mass ratio, I the current of charged particles and Φ_B the potential difference encountered by the particle. The mass flow rate, assuming the conservation of charge, for a beam with constant charge-over-mass ratio is

$$\dot{m} = I\frac{m_0}{q}. \tag{2.53}$$

Thrust and specific impulse can therefore be formulated as

$$T = I\sqrt{2\Phi_B \frac{m_0}{q}} \tag{2.54}$$

$$I_{sp} = \frac{1}{g_0}\sqrt{2\Phi_B \frac{q}{m_0}}. \tag{2.55}$$

Equations 2.54 and 2.55, valid for a single electrospray emitter, show the fundamental divergence between a high thrust and high specific impulse. In early thrusters mainly

Table 2.4: Theoretical specific impulse for an electrospray source in ionic mode (in seconds)

Ionic compound	Applied Voltage		
	1 kV	2 kV	5 kV
EMI^+ (monomer)	4246	6005	9494
$(EMI\text{-}BF_4)EMI^+$ (dimer)	2545	3599	5690
$(EMI\text{-}BF_4)_2EMI^+$ (trimer)	1987	2810	4442

droplets were emitted, but the discovery of an ionic spraying mode using ionic liquids (Romero-Sanz *et al.* 2003) promises an important increase of the charge over mass ratio. Chiu *et al.* (2005) report a specific impulse of 4000 s for an $EMI\text{-}BF_4$ capillary type source. Table 2.4 indicates the maximum theoretical specific impulse achievable for a beam consisting of either the monomer, dimer and trimer of the ionic liquid $EMI\text{-}BF_4$ and shows that high specific impulses can be achieved while operating at moderate voltages.

2.2.2   Thrust

The limitation of mass available on-board a satellite requires an efficient use of the fuel and thus a high specific impulse. To cover a thrust ranging from 1 μN to 1 mN the following measures can be taken: 1) Increase of the voltage difference between source and acceleration electrode, but as the mass of the power supply scales with the magnitude of the voltage this can only be done to a limited extent. 2) Increase the current which, in general, is proportional to the flow rate. 3) Multiply the number of emitters.

For capillary electrospray sources using active pumping the flow rate in cone-jet mode scales with the applied pressure difference (Rosell-Llompart and Fernandez de la Mora 1994) and the applied voltage (Smith *et al.* 2006), as does the droplet size (Fernández de la Mora and Loscertales 1994, Chen *et al.* 1995). In passively fed systems recent research has identified that flow rate can be voltage modulated, but as for forced flow an increase in droplet size has been observed for higher flow rates (Jhuree *et al.* 2007). An increase in the mass of the expelled particle is not desired as the consequence would be a low specific impulse, thus increasing the current (flow rate) is not an interesting option to increase thrust.

For needle type emitters no data on droplet sizes as a function of emitter voltage is available. The energy spectra measured by Lozano (2006) show a similar energy pattern for a voltage range of several hundred volts and it can thus be assumed that beam characteristics are similar. Nevertheless it is unlikely that a single emitter will be able to generate thrust ranging from sub-micronewton to millinewton thrust.

The development of an array of electrospray sources remains therefore the best way to achieve the required thrust range. Figure 2.10 illustrates the power to thrust
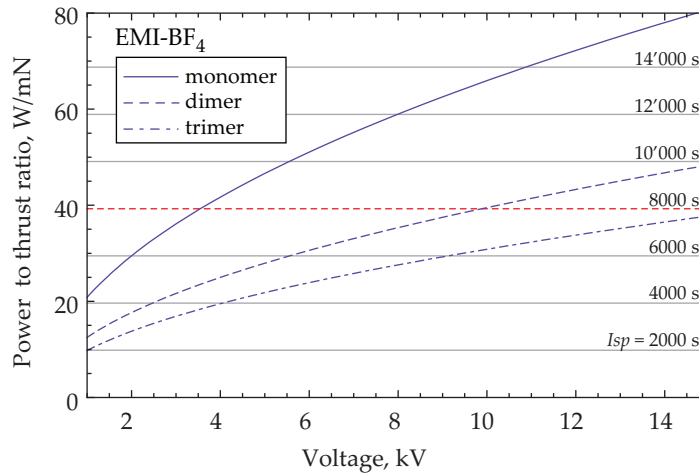
Figure 2.10: Power to thrust ratio for the monomer, dimer and trimer of the ionic liquid EMI-BF$_4$.

ratio for the monomer, dimer and trimer of the ionic liquid EMI-BF$_4$. A beam composed of monomers reaches a specific impulse of 8000 s (as specified in table 2.3) at 3.6 kV, the dimer at 9.8 kV and the trimer at 16.2 kV. Measurements by Romero-Sanz *et al.* (2003) have shown that for very low flow rates the repartition between the ion species are: 38% monomer, 53% dimer and 9% trimer. This suggest that the design should allow for an electrode for particle extraction (extraction electrode), and an electrode to accelerate (acceleration electrode) the ions in order to attain the required specific impulse.

2.3   Fuel

Electrosprays can be operated with almost any conductive liquid, but as discussed previously ionic mode has only been reached by a few ionic liquids which have been summarized earlier in table 2.2. Certain room temperature ionic liquids, or molten salts have been known for almost a century, but interest has only occurred over the last few years. Since the discovery of the air and moisture stable imidazolium based ionic liquids (Wilkes and Zaworotko 1992) the field has developed at a very fast rate. Ionic liquids are composed, like salts, of anions and cations, they are perceived to be environmentally benign, largely because of their non-volatility. For use in space they possess excellent properties such as high thermal stability and negligible vapor pressure. The properties of ionic liquids are tunable and it has been predicted that 10^{18} different types of ionic liquids could exist (Holbrey and Seddon 1999).

Based on the available experimental data and on the available literature the ionic liquids 1-Ethyl-3-methylimidazolium tetrafluoroborate (EMI-BF$_4$) and 1-Ethyl-3-methylimidazolium bis(trifluoromethylsulfonyl)imide (EMI-Tf$_2$N) were chosen as
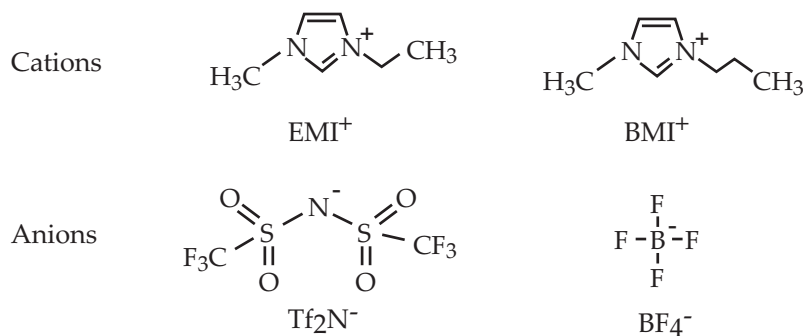
Figure 2.11: Skeletal formulas of the cations EMI^+, BMI^+ and the anions BF_4^- and Tf_2N^-

fuel for thruster characterization[1]. The skeletal formulas of these ionic liquids are illustrated in figure 2.11.

Contamination and degradation of the ionic liquid needs to be considered when choosing them as fuel for a spacecraft propulsion system. Any change in the liquid properties can lead to a change in thruster performance, which is clearly not desired. Seddon *et al.* (2000) provide a good introduction to the synthesis of ionic liquids and the effect of impurities on their properties. They studied the effects of cholride impurities, a byproduct of the liquids synthesis, and observed an increase in viscosity and decrease in density for increasing chloride concentration. As important differences in chloride concentration exist for various synthesis routes the fabrication process should be carefully chosen.

At room temperature the ionic liquid $EMI\text{-}Tf_2N$ is insoluble in water while EMI-BF_4 is fully miscible with water. Seddon *et al.* (2000) show that the anion has a primary effect on water miscibility and the cation a secondary effect. They also note that ionic liquids are in general miscible with liquids having a medium to high dielectric constant and are immiscible with low-dielectric constant liquids. Tests with BMI-BF_4 show that after two hours exposure to air the mass percentage of water is 2 wt%. For $EMI\text{-}Tf_2N$ Bonhôte *et al.* (1995) report a mass percentage of water content in saturation of 1.4 wt% at 20°C. In consequence special care is required when handling and storing ionic liquids as the presence of water will change the liquids properties and evaporation during depressurization causes bubble formation within the fluidic system.

Missions such as LISA will amass hundreds of thousands kilorads over their lifetime and the fuel will be exposed to ultraviolet radiation. Qi *et al.* (2008) exposed BMI-BF_4 to γ-radiation and observed a darkening of the liquid and identified the scission of bonds within the BMI^+ cation. Although not considered in the fuel selection of this work the liquids behavior under radiation conditions should also be considered when choosing ionic liquids as fuel for spacecraft propulsion.

---

[1]Often in literature $EMI\text{-}Tf_2N$ is abbreviated as EMI-Im, and the imidazolium based cation based on the number of carbon molecules in the linear alkyl chain $[C_n mim]^+$

2.4   Conclusion

An electrospray thruster can be operated in one of the modes of the stable cone-jet
regime. These modes generate a particle spray which is either composed of ionic com-
plexes, droplets or both. A qualitative study of the different regimes has been done
and scaling laws for the well known droplet mode have been reviewed. A literature
overview of the performance characteristics in the ionic regime and a table compiling
the various ionic liquids that have been shown to emit ions have been presented.

The second part of this chapter investigates the specifications required by a
thruster system capable to span a thrust ranging from micro- to millinewtons. To
fulfill the specific impulse requirements of $I_{sp} \geq 8000$ s an accelerator electrode is
needed in addition to the extractor electrode, as the extractor voltage is only around
1 kV which results in an I_{sp} below 4000 s. As mostly monomers and dimers are
emitted this acceleration electrode would need to be at a voltage around 10 kV (see
fig. 2.10), which still yields (theoretically) a power-to-thrust ratio well below the
specified 80 W·mN^{-1}. The emitter "electrode" being the liquid, lifetime issues on
the emitter side should mainly be due to fuel rather than to capillary degradation, as
discussed at the end of this chapter.

Chapter 3

Onset Voltage Modeling

A MODEL predicting the onset voltage is a powerful tool when designing MEMS electrospray emitter arrays. In particular electric field distortion of adjacent emitters in symmetrical arrays leads to inhomogeneities in onset voltages across the array and should be minimized.

The common model to determine the onset voltage assumes a paraboloid or hyperboloid tip facing an extraction electrode (Mair 1980, Prewett and Mair 1991, Martínez-Sánchez 2004), as introduced previously in section 2.1.2. It assumes that once the electrical stress at the tip of the needle exceeds the surface tension of the liquid a cone will form and emission will start. This approach has shown good agreement with experiments using long slender needles (Mair 1980), but does not produce satisfactory results for lower aspect ratio structures as can be made for MEMS. One difficulty is the complex geometry surrounding the emitter and distorting the electric field around the liquid surface. Pioneering work on the effect of capillary spacing in arrays has been done by Regele *et al.* (2002) and Quang Tran Si *et al.* (2007). Both authors have studied the influence of array pitch on the onset voltage and present an analytical model to calculate the onset voltage in their arrays, but require the experimental determination of a calibration factor.

The objective of this chapter is to introduce an alternative method, developed as part of this thesis, to compute the onset voltage. This method allows to quantitatively determine the onset voltage of single or arrays of electrosprays taking into account the real emitter-extractor geometry and the surface tension of the liquid. The method is based on an analytical approach, but requires a finite element model (FEM) to solve the Laplace equation. The approach assumes a quasi-static evolution of the liquid at the tip of the capillary and does not consider fluid dynamics or space charge effects.

3.1 Overview

The method can be best understood as a sequence of snapshots taken of the forming cone at the tip of a capillary or needle. This approach avoids the difficulty of modeling
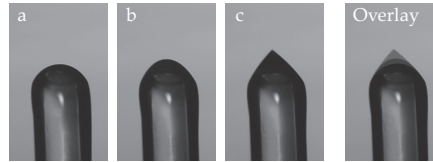
Figure 3.1: Sharpening of the liquid surface at the tip of a 360 μm outer diameter capillary. Photographs were taken at ambient pressure while spraying ionic liquid EMI-BF$_4$, with a surface tension of 0.045 N/m. The extractor electrode (not visible in these images) is a plate placed a few millimeters above the capillary.

hydrodynamic effects by assuming a quasi static evolution of the liquid at the tip of a capillary. As the voltage difference between extractor electrode and emitter increases the liquid at the tip of the capillary starts to deform, as shown in figure 3.1. For non-forced flow observations indicate that the shape of this deforming liquid surface goes from a flat surface into a perfect cone, similar to a conic section transforming from an ellipsoid into a paraboloid while staying within fixed generatrices. Consequently a conic surface has been chosen to model the liquids behavior. The shape of this model surface is controlled by the radius of curvature at the apex of the deforming conic surface. The method computes the equilibrium voltage between surface tension and electric field for a series of conic surfaces, constructed on a static strucuture, with decreasing apex radii. From the resulting relationships between equilibrium voltage and apex radius the onset voltage is determined.

In contrast to the method computing the equilibrium voltage of the liquid on the tip of a hyperboloid surface and assuming a snap-over behavior once equilibrium is reached (Sec. 2.1.2) this snapshot method takes into account the deformation of the liquid on top of the capillary. As will be shown in paragraph 3.4.1 the electric field at the apex of a liquid meniscus evolving within the Taylor cone half-angle of 49.3° is inversely proportional to the square root of the apex radius. This behavior allows predicting the onset voltage for purely ionic mode and droplet mode jets without knowing of the electric field level necessary to initiate emission. Onset voltage modeling for other cone half-angles will be discussed in paragraph 3.5. We will show that for angles below 49.3° the knowledge of a "critical" electric field at the apex of the liquid is necessary to determine at which voltage emission starts.

It should be noted that this study is limited to capillaries with flat tops, but the same approach could be taken for determining onset voltages on the tip of needles. So far only problems with an axisymmetric liquid cone have been investigated.

3.2   Methodology and theoretical background

The method presented hereafter is a four step process: a) define a geometry consisting of a fixed capillary on top of which a conductive liquid is placed with a pre-determined shape, this shape is varied from flat to a cone and can be expressed by the radius of

curvature r_a at the apex. b) compute the relationship between electric field at the apex and applied voltage for different apex radii of curvature (it is assumed the liquid and capillary are perfect conductors). c) determine the equilibrium voltage at which the electrostatic and surface tension forces are equal for any r_a, finally d) using the plot of equilibrium voltage, V_0, vs. r_a, and the approximate knowledge of the electric field required for ion emission, determine with high accuracy the onset voltage for electrospray.

Because this model only considers voltages up to emission, no emission occurs hence there is no space charge and so the combination of the static geometry of the emitter with the evolving surface defines the boundary conditions of the Laplace problem. Figure 3.1 shows a series of photographs taken of tip sharpening. Images 3.1a and 3.1b represent steady states below the onset voltage. Once a threshold voltage is reached the liquid drop snaps-over into a Taylor cone, fig. 3.1c. Because we assume a quasi-static case the liquid surface and capillary structure can be considered at an equipotential. Once snap-over occurs charge transport becomes an issue for low conductivity liquids. The momentum gained by the liquid needs to be dissipated or can lead to oscillations of the liquid surface. For this model we will only consider the point up to snap-over for sprays operating in droplet mode, thus ignoring all dynamic aspects, such as jet formation. To reach ionic mode on the other hand the time to replenish charges at the surface during snap-over, thus keeping the surface equipontential, needs to be below the hydrodynamic time, as discussed in section 2.1.3. Thus the flow rate needs to be as low as possible.

This chapter is organized in the same order as the method's practical application. The model requires the superposition of a liquid surface on top of a static capillary geometry, therefore at first the variable liquid surface is constructed using a function closely reproducing the liquids behavior (Sec. 3.2.1). This surface is then combined with the static emitter geometry and the Laplace equation solved for an arbitrary potential (Sec. 3.2.2). Due to the linear nature of the problem the relationship between electric field and potential can be extrapolated to solve the equilibrium equation relating electric stress and the surface tension (Sec. 3.2.3). The interpretation of the obtained equilibrium voltage curves leads to the determination of the onset voltage.

3.2.1 Liquid surface modeling

For electrosprays the shape of the liquid surface in transition from a flat surface into a cone is only poorly documented and varies depending on the type of liquid, the applied voltages and the flow regime. Observations by Driesel *et al.* (1996*a*) of liquid metal ion sources show a stable cone for very low emission currents and a cone half angle close to $49.3°$ as predicted by Taylor (1964).

Observations (fig. 3.1) of the liquid on the tip of a 360 μm capillary show an initial sharpening of the liquid surface as the voltage is increased, and once a threshold voltage is reached the surface deforms suddenly into a cone.

Near the onset voltage the emitted spray may operate in a pulsating mode rather than in a steady state. A slight increase in the flow rate or voltage leads to a con-

stant current operating mode. A very large increase in voltage will lead to unstable operation and multiple emission sites per capillary. Two research groups have studied pulsating electrosprays with high speed cameras (Marginean *et al.* 2004, Alexander *et al.* 2006) and have defined four distinct modes of operation with a cycle duration around 500 μs. During phase I the liquid accumulates at the tip of the capillary and is close to spherical shape. In phase II the Maxwell stress transforms the surface into a cone. Once it transitions into phase III the cone deforms into a cusp like structure with a jet, finally in phase IV the liquid retreats into a drop and the cycle restarts.

Based on observations made in experiment and on the shapes observed in pulsating ES the sharpening of the apex is modeled by a conic section. The chosen function corresponds to a straight line for an infinite radius of curvature, $r_a = \infty$, and a perfect cone for zero apex radius, $r_a = 0$. An arc of a conic having such properties can be expressed mathematically as a Bernstein-Bézier curve (Faux and Pratt 1979)

$$\vec{C}(s) = \frac{B_{0,2}(s)\vec{P_0} + B_{1,2}(s)w\vec{P_1} + B_{2,2}(s)\vec{P_2}}{B_{0,2}(s) + B_{1,2}(s)w + B_{2,2}(s)} \qquad (3.1)$$

where $B_{i,p}(s)$ are the p th degree Bernstein basis functions defined by

$$B_{i,p}(s) \quad = \quad \begin{pmatrix} p \\ i \end{pmatrix} s^i (1-s)^{p-i} \quad (i = 0, 1, \cdots, p) \qquad (3.2)$$

$$\begin{pmatrix} p \\ i \end{pmatrix} \quad : \quad \text{Binomial coefficient.}$$

The parameter $w \in [0, \infty)$ defines the apex radius of curvature r_a and $s \in [0, 0.5]$ is the running parameter. Equation 3.1 defines a one parameter family of conics passing through $\vec{P_0}$ and $\vec{P_2}$. The conic is further tangent to the chords $[\vec{P_0}, \vec{P_1}]$ and $[\vec{P_1}, \vec{P_2}]$. Figure 3.2 plots the function, bounded by the asymptotes of the Taylor half-angle, β, for different apex radii. For an arc having its apex on the $z = 0$ line and bound by the cone half angle β the chords can be written as

$$\vec{P_0} = -\vec{P_2} = \begin{pmatrix} -p_x \\ 0 \end{pmatrix}; \quad \vec{P_1} = \begin{pmatrix} 0 \\ p_x \cot(\beta) \end{pmatrix}. \qquad (3.3)$$

The surface obtained by spinning this curve around the z-axis in a cartesian coordinate system yields the following parametric surface equations

$$
\begin{aligned}
x(s, w, \phi) \quad &= \quad \frac{(1-2s)\, p_x}{1 - 2s(1-s)(1-w)} \cos \phi \\
y(s, w, \phi) \quad &= \quad \frac{(1-2s)\, p_x}{1 - 2s(1-s)(1-w)} \sin \phi \\
z(s, w, \phi) \quad &= \quad \frac{2(1-s)s\, w \cot \beta\, p_x}{1 - 2s(1-s)(1-w)}
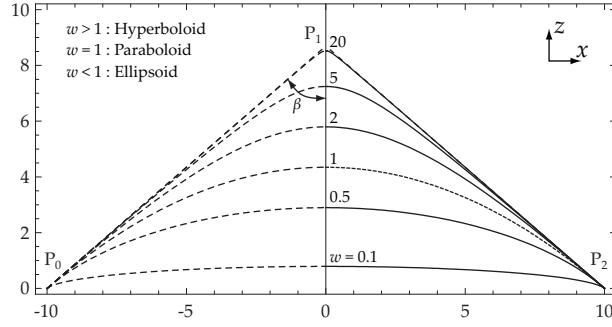\end{aligned}
\qquad (3.4)
$$

Figure 3.2: Plot of the conic function used to model the formation of a Taylor cone with $p_x = 10$ and $\beta = 49.3°$.

where $\phi \in [0, 2\pi)$. In cartesian representation equation 3.4 can be written as

$$\left(\frac{|1 - w^2|}{w} \frac{z}{p_x \cot \beta} + w \right)^2 + \left(1 - w^2\right) \left(\frac{r}{p_x} \right)^2 = 1 \qquad (3.5)$$

where $r^2 = x^2 + y^2$. For each w a radius of curvature at the apex of the conic surface is associated

$$w \longrightarrow r_a = r_a(w). \qquad (3.6)$$

The axial symmetry of the the surface allows to find the radius at the apex by making a projection of the surface onto the x-z axis (fig. 3.2) by setting $\phi = 0$ and thus eliminating $y(s, w, \phi)$. For a parametric curve

$$r_a = \left| \frac{\left(x'^2 + z'^2 \right)^{3/2}}{\begin{vmatrix} x' & z' \\ x'' & z'' \end{vmatrix}} \right| \qquad (3.7)$$

The radius of curvature at the apex is

$$r_a = \frac{p_x}{w} \tan \beta. \qquad (3.8)$$

3.2.2 Solving the Laplace equation

Assuming that the liquid surface deforms in a quasi-static way and that no emission occurs the Laplace equation can be used to compute the electric potential (equations 2.13 and 2.14). The boundary conditions are the two potentials of the conductors: the extraction electrode, and the capillary and liquid, which form one conductor. The complexity of the geometry makes it difficult to find a solution using analytical
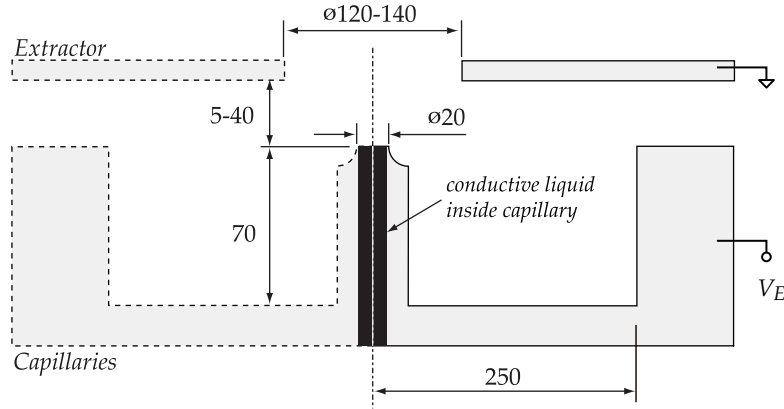
Figure 3.3: Geometry of the electrospray thruster used for onset voltage simulation. The insulator between capillary emitters and extractor electrodes is not shown, dimensions are in microns.

methods thus a finite element model is constructed to compute the electric field distribution based on the potential on the extractor electrode and on the capillary.

The geometry of the MEMS thruster developed in this thesis is illustrated in figure 3.3. To simplify the geometry an axisymmetrical model is created, where the adjacent capillaries or structures are represented by a solid sidewall. To decrease computation time only a small slice of the symmetrical geometry is modeled by carefully constraining the lateral faces of the slice to have the same potential distribution (fig. 3.4). To generate cyclic constraints in ANSYS a lateral face is first meshed with surface elements, this mesh is then replicated onto the other face. The next step consists in volume-meshing the entire slice, removing the unnecessary surface elements and placing cyclical constraints on the lateral faces to reproduce the behavior of the axisymmetric geometry. Finally surface potentials are defined, the capillary and liquid surfaces are set to an arbitrary voltage, V_ξ, and the extractor electrode is placed at zero potential. At this point the solver can be launched and the resulting electric field, E_{a_ξ} at the apex of the liquid is obtained.

This procedure is repeated for a series of liquid shapes (described in Sec.3.2.1) sharpening into a Taylor cone. For each liquid shape (i.e., for each radius of curvature r_a) the ratio

$$\kappa = \frac{E_{a_\xi}}{V_\xi} \tag{3.9}$$

can be obtained from the FEM solution, allowing the electric field E_{a_ξ} to be computed for any applied voltage to the capillary using the expression.

$$E_{apex} = \kappa V_{capillary} \tag{3.10}$$

When the electric field of sharp surfaces having nanometer scale radii surrounded by macroscopic structures is computed particular care needs to be taken when setting up the mesh. Although a proof of the validity of a finite element tool for all geometries
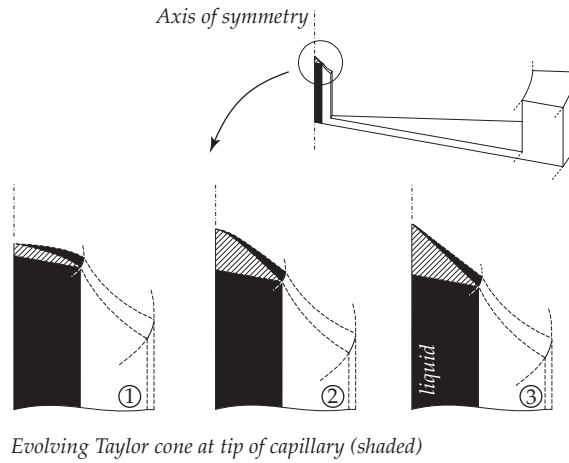
Evolving Taylor cone at tip of capillary (shaded)

Figure 3.4: Slice of the geometry used to compute the electric field distribution for three radii of curvature. The liquid and capillary walls are assumed to be perfect conductors. The extractor electrode is not shown for clarity, and is as in figure 3.3.

is not possible we have simulated a specific case of a sharpening cone for which an analytical solution exist. The results are in excellent agreement and the electric field computed with FEM and using analytical expression differ by less than 2%, as will be shown later in section 3.3.

3.2.3 Equilibrium between surface and electrical stress

The equilibrium between surface tension and electrical stress at the apex of the forming liquid cone can be expressed as (Mair 1980)

$$\frac{2\gamma}{r_a} = \frac{1}{2}\epsilon_0 E_{a_0}^2 \tag{3.11}$$

where γ is the surface tension, ϵ_0 the permittivity of free space, E_{a_0} is the equilibrium electrical field for a radius of curvature r_a at the apex of the deforming liquid. The vector signs have been removed as the problem is considered to be symmetrical and the electric field lies on the axis of symmetry.

The voltage difference, V_0, between the emitter (capillary combined with liquid surfaces) and the extractor electrode to obtain a radius of curvature, r_a, at the apex of the liquid is given by

$$V_0 = \frac{1}{\kappa}E_{a_0} = \frac{1}{\kappa}\sqrt{\frac{4\gamma}{\epsilon_0 r_a}}, \tag{3.12}$$

where κ is the geometric factor defined in equation 3.9 that depends on the apex radius r_a and is determined through finite element modeling. This equation simply describes the necessary equilibrium voltage to obtain a certain radius at the apex of the liquid. Unlike equation 2.28, which provides a unique expression for the onset voltage, V_0 above needs to be computed for a range of apex radii and the resulting

equilibrium voltage vs. apex radius curve interpreted in order to determine the onset voltage as will be shown in section 3.4.

In the case of a spray in ionic mode a critical electric field on the surface of the liquid needs to be reached before ions start to evaporate and are accelerated toward the extractor electrode. The critical field depends on the liquids properties, but ion evaporation is assumed to start for fields larger than 1 V/nm (Gamero-Castaño and Fernández de la Mora 2000). To determine the critical voltages, V_c, we can reuse the relationships between potential, V_ξ, and electric field E_{a_ξ} computed using FEM for various apex radii r_a. The critical voltage on the emitter necessary to initiate ion evaporation at the apex of the liquid surface is simply given by

$$V_c = \frac{1}{\kappa} E_c \tag{3.13}$$

where E_c is the critical field necessary to initiate ion emission. The intersection between the critical voltage vs. r_a and the equilibrium voltage vs. r_a, $V_{oc} = V_c(r_{a_{oc}}) = V_0(r_{a_{oc}})$ allows the determination of the onset voltage, V_{oc}, for electrosprays operating in ionic mode. As will be shown in section 3.5 this result is valid for cone half-angles smaller than or equal to $49.3°$. For larger angles, going from large to small apex radii, the equilibrium voltage curve reaches a maximum before decreasing again. Possible implications of this behavior will be discussed later (Sec. 3.5).

3.3   FEM validation

Computing the electric field of sharp surfaces having nanometer scale radii surrounded by macroscopic structures requires particular care when setting up the mesh. The objective of this section is not to prove that the FEM model will suit all possible geometries but to demonstrate by means of a specific case for which an analytical solution exists that the results are within expected ranges and thus give us confidence for later investigations.

The test case consists in computing the electric field of a hyperboloid, representing the liquid surface, bound by two parallel plates, shown in fig. 3.5. This rather simple geometry can be computed by superposition of the electric field of two parallel plates and a hyperboloid-plate system. The latter is expressed in prolate spheroidal coordinates (Abramowitz and Stegun 1964), introduced in section 2.1.2.

$$
\begin{aligned}
x &= \alpha\sqrt{(u^2 - 1)(1 - v^2)} \cos\psi \\
y &= \alpha\sqrt{(u^2 - 1)(1 - v^2)} \sin\psi \\
z &= \alpha\, u\, v
\end{aligned}
\tag{3.14}
$$

where $u \in [1, \infty)$, $v \in [-1, 1]$, and $\psi \in [0, 2\pi)$. For the validation study a hyperboloid surface is defined by a constant $v = v_0$ and bound by a cone with half-angle $\beta = \arccos v_0$. The electric field for different α is calculated which defines the distance between the electrode and the focal point of the hyperbola. For $\alpha = 0$ the cone
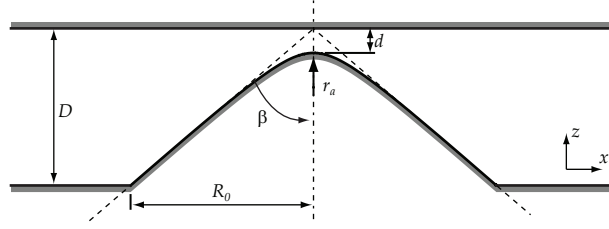
Figure 3.5: Cross-section of the geometry used to validate the finite element model. The liquid is assumed to be a perfect conductor. For zero apex radius the cone touches the electrode, for infinite radius the geometry consists of two parallel plates

therefore touches the electrode. As will be shown later the apex radius and the apex-electrode distance are related to α and v, which allows us to correlate the results from the FEM with the analytical model. The boundary conditions are $V(v_0) = V_0$ and $V(0) = 0$ and yield the following electric field perpendicular to the hyperboloid surface

$$E_v = -\frac{2V_0}{\alpha\sqrt{1-v^2}\sqrt{u^2-v^2}\log\frac{1+v_0}{1-v_0}}. \tag{3.15}$$

The radius at the apex, r_a, and the distance between hyperboloid apex and electrode, d, can be expressed as

$$r_a = \frac{\alpha\left(1-v_0^2\right)}{v_0} \tag{3.16}$$

$$d = \alpha v_0 \tag{3.17}$$

By combining 3.15, 3.16, substituting $v_0 = \cos\beta$ and superposing the field of the parallel plates the field at the apex of the cone becomes

$$E_a = -V_0\left(\frac{2}{r_a\cos\beta\log\frac{1+\cos\beta}{1-\cos\beta}} + \frac{1}{D}\right) \tag{3.18}$$

where D is the distance between the plates.

Figure 3.6 shows the results of $E_a(V)/V$ for a base radius, R_0, of 10 μm (filled circles). These results were obtained in ANSYS using 20-node three dimensional elements, charge based electric elements (SOLID122). The second curve (diamonds) illustrates the difference between the analytical solution and the finite element model using a surface generated from equation 3.4. The agreement is very good, with errors of less than 2% for liquid radii of curvature from 10 nm to 2 μm. The divergence for radii above 10 μm can be explained by observing that for $w < 1$ the spline becomes parabolic. On the other hand for small radii meshing becomes increasingly difficult and the large difference in element size causes an increase in the error. Nevertheless the results show that electric fields can be computed at sharp tips using FEM for dimensions scaling by more than three orders of magnitude.
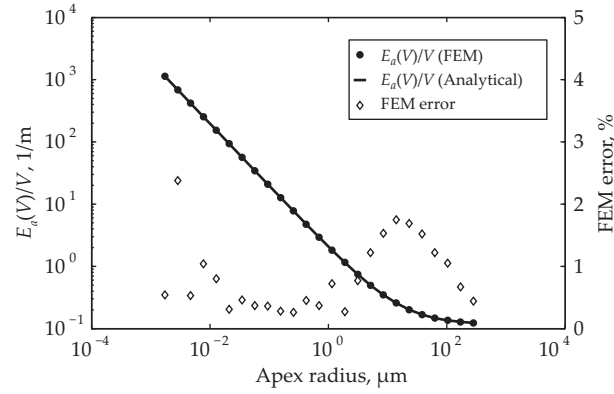
Figure 3.6: $E_a(V)/V$ field computed for the validation model, FEM (filled circles) and analytical results (line) overlap. The error between simulation and analytical solution (diamonds) is plotted on the right axis. The good agreement shows that the FEM model is accurate even though the elements of the mesh covers a size range from 100 microns to 1 nm.

3.4   Results and Discussion

3.4.1   Result interpretation

The method was applied to the geometry illustrated in figure 3.3. The finite element model to determine the relationship between potential and electric field was created in ANSYS following the procedures given in paragraph 3.2.2. Figure 3.7 shows the computed equilibrium voltages for a 20 μm inner diameter capillary placed 40 μm below an extractor electrode with a 120 μm hole. Each point corresponds to a solution of equation 3.11, giving an equilibrium voltage for a given apex radius. Although this is the reverse of another possible approach (which would be to set a voltage, then compute the radius of curvature), the final plot provides the same information: neglecting ion emission, the radius of curvature can be determined for any applied voltage.

With decreasing apex radii ($r_a < 1\mu$m) the equilibrium voltage curve becomes flat and the electric field starts behaving inversely proportional to the square root of the apex radius, $1/\sqrt{r_a}$, leading to the constant equilibrium voltage observed (fig. 3.8). For radii above 1 μm the electric field is distorted by the structure surrounding the emitters.

What happens to the shape of the liquid if the voltage is gently increased from 0 V up to the onset voltage? Based on the observations made during spray experiments (such as the single capillary illustrated in fig. 3.1) the tip apex radius decreases and once the onset voltage is reached the surface snaps-over into a cone-like structure. While remaining below the onset voltage and assuming a quasi-static change in the shape of the liquid, charge relaxation is not an issue and thus the surface remains
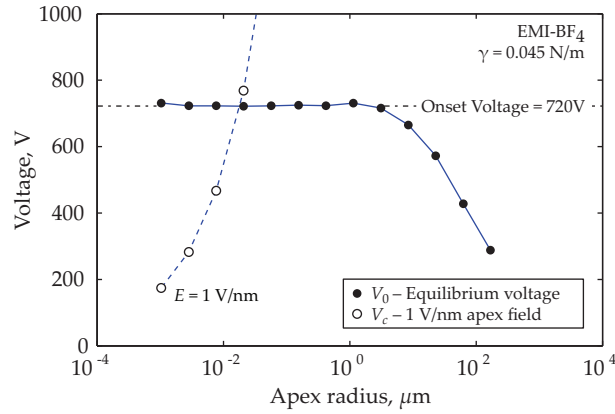
Figure 3.7: Plot of equilibrium voltage vs. apex radius for an emitter with an extractor electrode 40 μm above the capillary tip and with an extractor diameter of 120 μm computed using this method (lines only added for readability). The dashed curve represents an apex field of 1 V/nm. In this case the onset value is the "plateau voltage" of 720 V.

equipotential. Once the onset voltage is reached, in figure 3.7 this occurs for an apex radius below 1 μm, the liquid surface sharpens and a spray is initiated.

At this point it is necessary to make a distinction between droplet and ionic modes of operation. As discussed in paragraph 3.2.3, a critical voltage exists (for ionic sprays) at which the electric field at the apex is large enough to initiate ion emission. In figure 3.7 this critical voltage has been computed using equation 3.13 assuming a field strength of $E_c = 1$ V/nm. The equilibrium and critical voltage plots, V_0 and V_c, intersect at a voltage of 720 V, the onset voltage, and an apex radius of about 20 nm. Note that because the Equilibrium voltage vs. apex radius curve exhibits a large flat region, the same onset voltage would have be found for a critical field for emission of 2 V/nm or 0.5 V/nm.

For electrosprays operating in droplet mode, after the onset voltage is reached, the notion of critical field does not apply. In this case we assume that, above the onset voltage, the deformation into a cone-like structure with a jet occurs faster than charge relaxation. The assumption of an equipotential surface is therefore no longer valid and the surface shape selected in paragraph 3.2.1 no longer reproduces the behavior of the liquid. This snap-over behavior could also explain why for liquids with low conductivities, such as EMI-Tf$_2$N (0.88 S/m), purely ionic modes have been observed when sprayed using a needle (high fluid impedance, limited flow rate) and droplet mode when sprayed using a capillary (Garoz *et al.* 2007, Gamero-Castaño 2008*b*, Castro *et al.* 2007). In the first case the surface remains at equipotential during snap-over, which occurs more slowly than charge-relaxation, while in the second case the surface (around the liquid apex) cannot be assumed to be an equipotential due to the liquid's high flow rate.
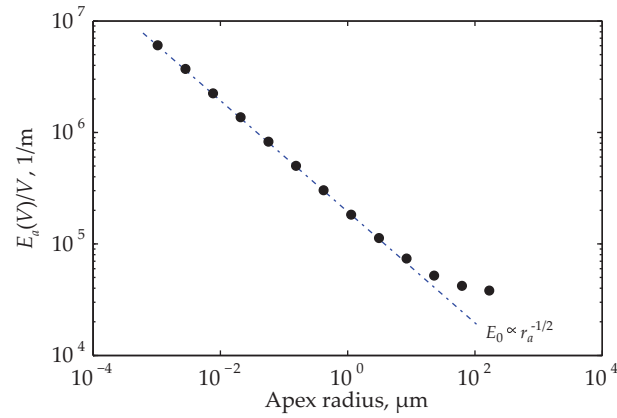
Figure 3.8: $E_a(V)/V$ electric field computed for the investigated MEMS geometry. The relationship $E_a \propto r_a^{-1/2}$ is clearly visible for apex radii of curvature less than 1 μm.

3.4.2 Correlation with other experimental results

To validate the method, the onset voltage was determined for the geometry of emitters reported by Quang Tran Si et al. (Quang Tran Si *et al.* 2007). The investigated configuration is a linear array of five stainless steel capillaries, each with an inner diameter of 0.5 mm and an outer diameter of 1.5 mm. The extractor electrode is placed at 7 mm above the flat tip of the capillaries. In their experimental setup the two external emitters were not spraying to reduce edge effects. Acetone, surface tension of 0.0237 N/m, was fed to the capillaries by means of a syringe pump at a flow rate of 20 μl/min. The operating voltage for the spray was defined for a fully stabilized cone on the central capillary.

For our finite element model a linear array of an infinite number of emitters was chosen, by modeling a single emitter and placing cyclical constraints at the boundary of the model. Meshing turned out to be critical, in particular as in this case the emitter geometry is not axisymmetric and the whole capillary needs to be modeled.

The results of the model for the onset voltage are shown in figure 3.9 together with experimental data by Quang Tran Si et al. As should be expected the onset voltage increases as the capillary distance decreases. The correlation of results is excellent, although the liquid was pumped and it could be argued that the onset voltage could be different for non-forced flows. The difference between the two curves can be explained by the limited number of emitters in the experiment and the edge effects, tending to deform the liquids from an axisymmetric geometry.
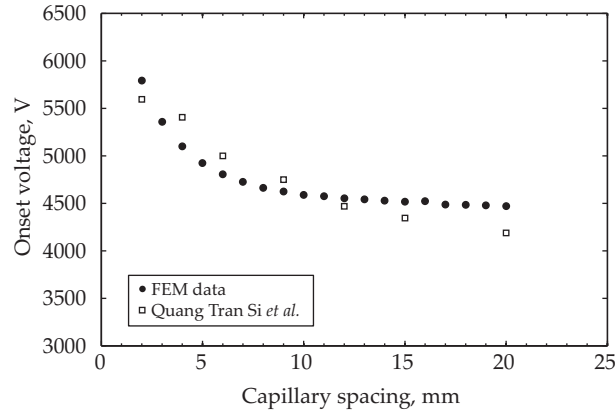
Figure 3.9: Comparison between results obtained with our method and measurements from Quang Tran Si et al. (Quang Tran Si *et al.* 2007).

3.5   Further Discussion

In the previous paragraph (3.4.1) the computed equilibrium apex electric field scaled as $1/\sqrt{r_a}$ with a cone half-angle of 49.3°. This behavior is valid as long as the apex-extractor distance is much larger than the apex radius of curvature, i.e. $d \gg r_a$. To illustrate this figure 3.10 shows the evolution of $E_a(V)/V$ as a function of apex radius. Two configurations were chosen: a liquid deforming on the tip of a needle and one on a flat surface. For both geometries the extractor electrode was placed at 500 μm from the base of the cone and the radius at the base of the cone was 10 μm.

For both geometries the shape of the curves are identical except for a shift in field strength. The three different slopes were obtained by varying the cone half-angle. This is interesting because research by Yarin *et al.* (2001) identified cone half-angles around 33.5° for liquids having nonrelaxing elastic forces. The existence of cone half-angles larger than 49.3° have been observed by Driesel et al. for liquid metal ion sources (Driesel *et al.* 1996*a*). For certain metals, such as gallium, they have measured an angle of almost 54° for very low emission currents. In analogy with the behavior of the field near a sharp point or conical hole (Jackson 1999) we can write

$$E \propto r_a^{\nu-1} \tag{3.19}$$

where ν is the solution of the equation

$$P_\nu(\cos(\pi - \beta)) = 0 \tag{3.20}$$

P_ν being the Legendre Polynomial of order ν.

Table 3.1 summarizes the values $\nu - 1$ extracted from figure 3.10 and compares them to the analytical results obtained solving equation 3.20. The results show a very good agreement between the analytical values and the computed ones. Therefore, for
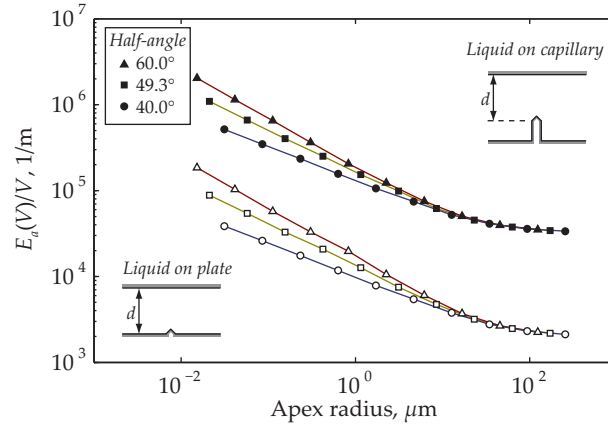
Figure 3.10: $E_a(V)/V$ computation for two emitter geometries and three different cone half-angles. Upper curves: liquid on the tip of a capillary; lower curves: liquid on a flat surface.

an extractor electrode placed far away from the liquid, it can be concluded that once a certain apex radius is reached the behavior of the electric field will only be influenced by the cone-half angle and not by the surrounding geometry. The consequence of this observation is that for a cone half angle of 49.3° the field will behave as $1/\sqrt{r_a}$ and in order to compute the onset voltage one single FEM model having a $w \gg 1$ (i.e. $r_a \ll p_x \tan(\beta)$) is sufficient. This also explains why the commonly used hyperbolic or parabolic surface models provide satisfactory results for slender needles placed far away from the extractor electrode.

The determination of the onset voltage is more complex for tip geometries with cone half-angles smaller or larger than the Taylor cone angle. These geometries require the computation of the entire equilibrium voltage curve. Figure 3.11 illustrates the equilibrium voltage behavior for the capillary geometry (10 μm radius, 500 μm extractor distance). For the Taylor cone angle, 49.3°, we obtain a flat onset voltage curve for small apex radii, while for an angle of 40° the equilibrium voltage increases steadily as r_a decreases. For a cone half-angle of 60° there is a maximum equilibrium voltage for a finite r_a value, i.e. the curve is non monotonic. The three dashed curves in figure 3.11 correspond to a tip field of 1 V/nm and have been computed for each cone half-angle using equation 3.13.

These results are of particular interest for electrospray sources operating in ionic mode and could explain why a difference is observed between onset and extinction voltage. For a 60° cone half-angle the equilibrium curve crosses a maximum which would, in this example, correspond to the onset voltage of approximately 770 V (marked with a red circle in fig. 3.11). If we now assume that the field self-enhances at the liquids apex, the radius will also decrease up to the point where the critical field for ion emission is reached (in fig. 3.11 this is the intersection with the red, dashed curve representing a field of 1 V/nm). At this point the equilibrium voltage

Table 3.1: Comparison of the slopes determined solving eq. 3.20 and extracted from the finite element model.

Geometry[1]	β[2]	ν[3]	$\nu - 1$	FEM[4]
C	40.0	0.422	-0.578	-0.565
S	40.0	0.422	-0.578	-0.567
C	49.3	0.500	-0.500	-0.482
S	49.3	0.500	-0.500	-0.491
C	60.0	0.602	-0.398	-0.390
S	60.4	0.602	-0.398	-0.394

[1] Geometry: (C) Liquid on capillary; (S) Liquid on plate.
[2] Cone half-angle
[3] Solution of equation 3.20
[4] Slope $\nu - 1$ computed from FEM

to sustain the critical field ($\approx$ 580 V) is below the maximum voltage ($\approx$ 770 V) and could therefore explain a difference between extinction and onset voltage. Since this study only considers the quasi-static case no direct information on the dynamic behavior of the liquid can be gained after snap-over.

For a cone half-angle of $30°$ a constant increase of the equilibrium voltage for a decreasing apex radius is computed. In figure 3.11 the 1 V/nm tip field curve crosses at 1650 V. In this case as the voltage is increased no snap-over happens and the knowledge of a threshold field for emission is necessary to determine the onset voltage. For angles below $49.3°$ the method is therefore only valid for sprays in ionic mode where a "critical field" for ion emission is known.

3.6 Conclusions

This chapter has introduced a novel method to compute the onset voltage for ion or droplet emission from a single or from an array of electrospray emitters with complex geometries. The model takes as input the geometry of the capillary and of the extraction electrode as well as the surface tension of the sprayed liquid. The key assumption in this model concerns the shape of the liquid surface that deforms (decreasing radius of curvature at the apex) under the influence of the increasing electric field. Based on experimental data, we chose a family of conic sections to represent the liquid surface.

The equilibrium voltage, representing the balance between surface tension and electric stress, is computed by means of a finite element model for a number of radii of curvature at the liquid apex. This provides a plot of radius of curvature r_a vs. equilibrium voltage V_0, ignoring space charge effects, from which the onset voltage might be determined.
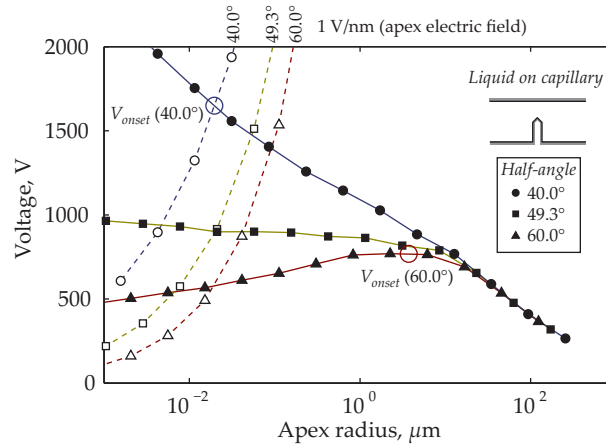
Figure 3.11: Equilibrium voltage curves on the tip of a capillary for three different cone half-angles. The solid lines represent the equilibrium voltage. The dashed lines represent, for each individual cone half-angle, the 1 V/nm field at the apex. For cone angles of 49.3° (Taylor cone angle), the onset voltage is equal to the value of the plateau in the equilibrium voltage. For cone angles below 49.3° (top solid curve) the onset voltage can only be computed if a "threshold field" for emission is known. As example the intersection with the 1 V/nm apex field is marked (upper circle). For angles below 49.3° (bottom solid curve) there is a maximum in the equilibrium voltage vs. r_a curve. In that case the onset voltage is the maximum in the equilibrium voltage curve (lower circle), since as the voltage is ramped up from zero, the radius of curvature will decrease continuously until the equilibrium voltage maximum is reached, at which point the liquid snaps-over to a cone or cusp-like shape and ion/droplet emission begins.

Noting the similarity in the behavior of the scaling of the equilibrium electric field vs. radius of curvature for liquid surfaces deforming within the asymptotes of the Taylor cone half-angle (49.3°) leads to a further simplification of the method. For geometries where the extractor electrodes distance from the capillary tip, d, is significantly larger than the apex radius, $(d/r_a \gg 1)$ the electric field scales as $1/\sqrt{r_a}$ for small apex radii. This leads to a flat equilibrium voltage curve vs. radius of curvature. This has two important consequences. 1) It is not necessary to compute the full critical voltage vs. r_a plot; it suffices to compute the equilibrium voltage for one single apex radius, as long as this apex radius of curvature is sufficiently small $(r_a \ll p_x \tan(\beta))$. The necessary apex radius to compute a reliable result is still several orders of magnitude larger than the one necessary to initiate particle emission. This results in a geometry which is much simpler to mesh when creating a finite element model and explains also why analytical models calculating the equilibrium voltage at the tip of needles work well for high aspect ratio needles or capillaries. 2) having a flat equilibrium voltage vs. r_a curve means that once this "plateau voltage" is reached a snap-over to smaller r_a can be expected. This has several

implications for this method. On one hand it allows predicting the onset voltage of sprays operating in droplet mode without any knowledge of the dynamic behavior of the liquid surface by assuming that once the "plateau voltage" is reached the liquid surface snaps over into droplet emission. On the other hand, as discussed in section 3.4.1, for cone-jets operating in ionic mode the onset voltage is insensitive to the exact value of the critical field for emission. This is important because the critical field for emission is often not well known, yet this method still allows very precise predictions of the onset voltage, with no free parameters.

For other cone half-angles the electric field curves have been found to behave in a similar way as a field near a sharp point or conical hole. This finding could simplify the determination of the onset voltage for other liquid geometries.

The method has been demonstrated on a single and arrays of capillaries. The onset voltages calculated and correlated to the macroscopic systems reported by Quang Tran Si *et al.* (2007) are in excellent agreement. As will be shown later (sec. 5.2) this is also the case for our microfabricated sources. For both cases, the complex geometries preclude determining the onset voltage by analytical means. This onset voltage determination technique is a powerful design tool for electrospray emitters, allowing the onset voltage to be rapidly computed for different geometries and for different liquids, thus enabling for instance high uniformity to be obtained, or geometries to be tuned for specific liquids.

Chapter 4

Thruster layout and fabrication

W<small>HEN</small> designing a microfabricated system a compromise between an optimal functional design and an excellent yield needs to be achieved. As discussed in the previous chapter parameters influencing the design of an electrospray thruster include the electrode to capillary spacing, capillary pitch, extractor electrode radius, the height and the radius of the capillary. The ideal case of a long slender capillary with no structures surrounding it is not only difficult or impossible to microfabricate but requires a large spacing between adjacent capillaries to avoid crosstalk. This simple example shows that on one hand the geometry of the emitter needs to be optimized to achieve the performance targets while on the other the fabrication process should be kept as simple and reproducible as possible.

This chapter will first introduce the design methodology and the different components of the thrust head. It will then present the various process flows to manufacture the capillaries and the extractor electrodes, post processing steps and lessons learned. Finally the assembly, structural, electrical and fludic interface will be discussed.

4.1 Methodology

The flowchart in figure 4.1 summarizes the applied design methodology. The thruster performance was defined based on the needs of missions such as the ESA/NASA Laser Interfereometric Space Antenna (LISA) and has been discussed previously in chapter 2.2.

The first design parameters were derived from experimental results reported in literature. Time-of-flight measurements done by Romero-Sanz *et al.* (2003) with pulled silica capillaries using the ionic liquid EMI-BF$_4$ have shown a spray composed of mainly monomers, dimers and trimers at very low flow rates and for higher flow rates the presence of droplets, providing thus the possibility to throttle thrust by
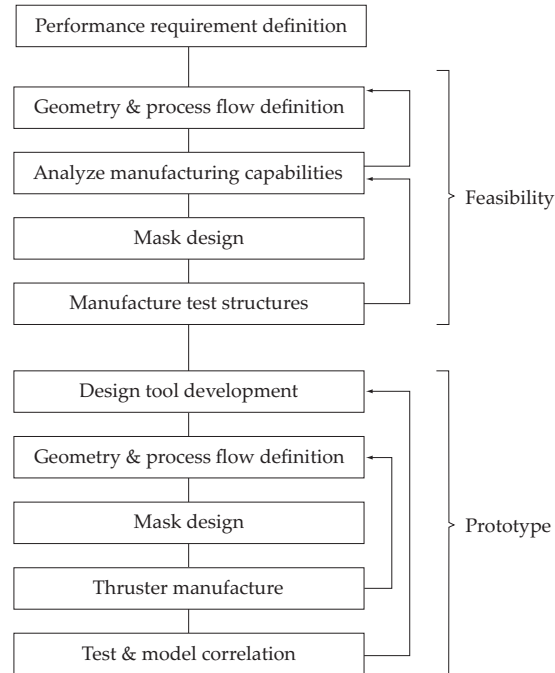
Figure 4.1: Flowchart illustrating the thruster development cycle. The process flow for the nozzles was developed during feasibility phase followed by a prototype phase where the entire integrated thruster was manufactured.

several orders of magnitude. Similar tip dimensions for microfabricated capillaries, as the pulled silica capillaries used by Romero-Sanz *et al.* in his experiments, have been microfabricated by Griss *et al.* (2002). Their process flow features single bulk micromachined silicon capillaries with tapered tips and hole diameters of 18 μm. This initial process flow was modified to allow the manufacture of scalable arrays of capillary emitters *with* integrated extractor electrodes.

Manufacturing capabilities at the University of Neuchâtel and EPFL cleanrooms were then analyzed and a process flow to microfabricate test structures was established. Figure 4.2 shows several SEM photographs of the test structures fabricated during the feasibility phase. Manufacturing yield was gradually improved during the various iterations in the feasibility and prototype phases.

Two series of thruster prototypes were manufactured. After a first test campaign several failure modes and design flaws were identified and improved in a second generation of devices. In addition to thruster modifications the test stand was continuously improved (refer to chapter 5.1). Further the need of an onset voltage model for the microfabricated thrusters was identified and lead to the development of the method introduced in chapter 3.
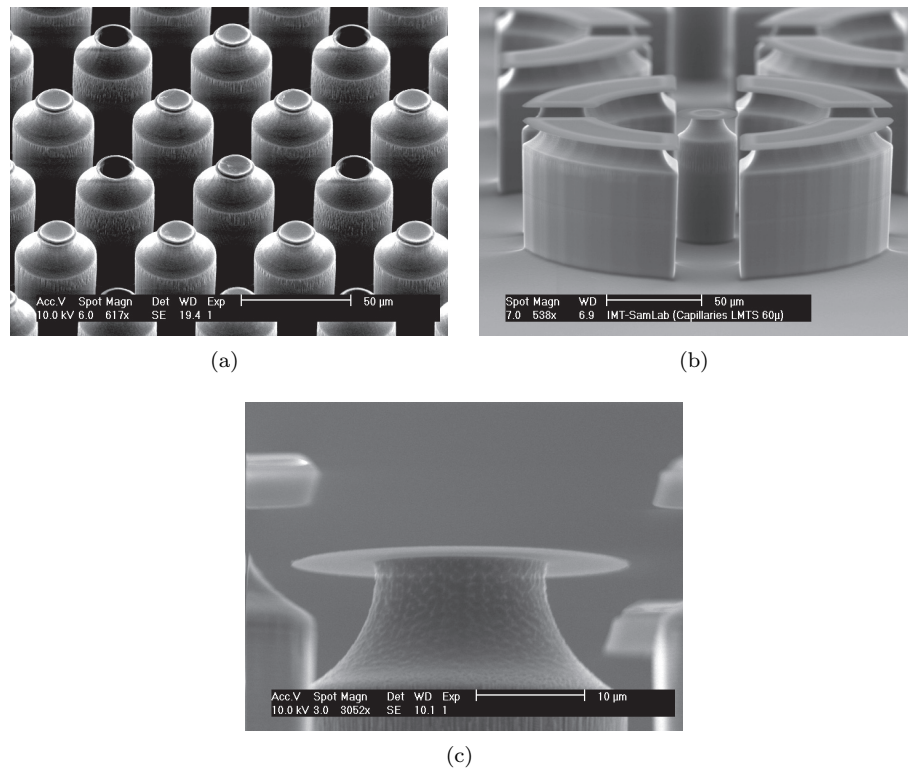
(a)

(b)

(c)

Figure 4.2: SEM photographs of the manufactured test structures. (a) Array of pillars and capillaries, (b) shows a capillary surrounded by a protective structure and (c) is a detail photograph of the tapered tip during manufacturing.
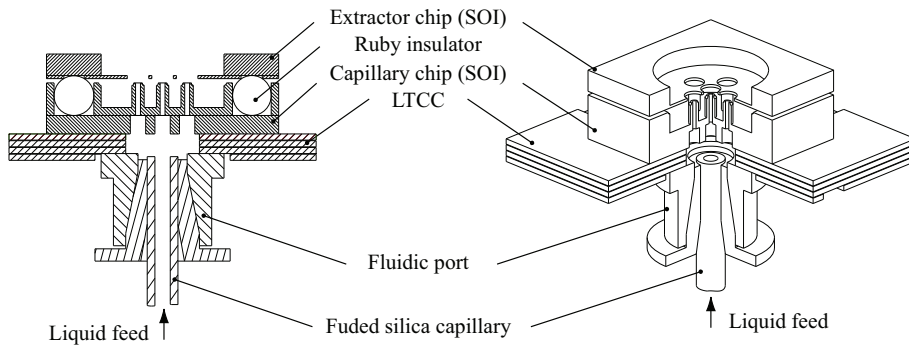
Figure 4.3: Cross section of the assembled thruster (drawing not to scale). The extractor electrode sits on top of the capillary chip (emitter) spaced by ruby balls. The capillary chip and a fluidic interface are glued onto a ceramic support. The whole assembly is hold together by a PEEK interface (not shown).

The first generation of capillary emitters and extractors were designed to be assembled at wafer scale, this approach was not well adapted as the thrusters could not be disassembled and failure modes investigated after testing. The assembly approach was changed in the second generation of devices by adding alignment features for chip scale assembly, a ceramic support to connect the capillary chip with the fluidic system and an interface made of PEEK to easily assemble and disassemble the capillary emitters and extractor electrodes.

4.2   Thruster layout

The thruster consists of an emitter and an extractor which are mounted onto a ceramic package or onto a printed circuit board (PCB). A cross section of the assembly is shown in figure 4.3. The capillaries stand off the silicon surface and face each an individual extractor electrode hole. The intention of this layout is to guarantee homogeneous spray characteristics across the array. The extractor electrode chip is electrically isolated from the capillary one by ruby balls or a micromachined Borofloat (Pyrex) wafer. The ruby balls are used for chip scale assembly and serve to electrically isolate the chips and to align the extractor electrodes with the capillaries. The Borofloat isolator is intended for wafer scale assembly using an anodic bonding process[1].

In early tests the capillary chips were mounted onto a printed circuit board (PCB) substrate and the extractor electrode was directly glued onto the emitter. For the second generation devices a ceramic package and a PEEK interface were developed allowing the disassembly of the thruster after spray tests. Initially, no active pumping of the liquid was foreseen, unfortunately initiating the spray in such a "passive"

---

[1]Although process flow for wafer scale assembly was developed the thrusters were always assembled at chip scale
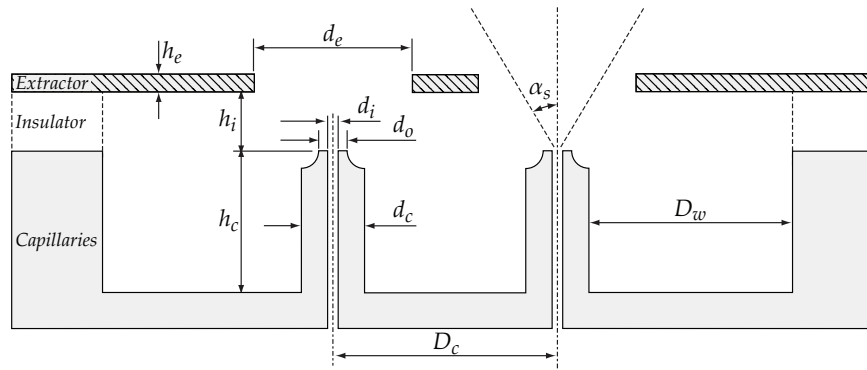
Figure 4.4: Cross-section of the thruster with geometrical parameters. The insulator is either integrated with the extractor electrode (Borofloat) or added during the assembly (Ruby micro-spheres). For simplicity the handle layers of the wafers have been omitted.

Table 4.1: Dimensions of the manufactured capillaries. The various parameters are illustrated in figure 4.4.

Parameter	Dimension	Unit	Description
h_c	70	μm	Capillary height
d_i	24, 28, 32	μm	Capillary inner diameter
d_o	34, 38, 42	μm	Capillary tip outer diameter
d_c	44, 48, 52	μm	Capillary base diameter
D_c	250	μm	Capillary pitch
h_i	50-65	μm	insulator height
h_e	50	μm	electrode height
d_e	150-250	μm	extractor electrode diameter
α_s	30	deg	spray half angle (maximum)

pumping regime was not or hardly possible, therefore a fluidic port was added to connect the emitter through a capillary to a fluid reservoir and actively pump the liquid.

The general thruster geometry is shown in figure 4.4. Dimensional parameters are either fixed by design or imposed by the manufacturing process. On the capillary side these include the capillary standoff height, h_c, the capillary pitch, D_c, and the capillary tip recess, $(d_c - d_i)/2$, while on the extractor side the height of the extractor electrode is fixed.

Manufacturing was done on 4" wafers with several design variations included on one wafer. Table 4.2 lists the various designs. The single capillaries can be used with extractor electrodes ranging from 150 to 250 μm

To manually align the diced emitter and extractor chips a matrix of grooves is included on the extractor electrode and on the emitter chip. Figure 4.5 illustrates the

Table 4.2: Design variations on the 4" wafers. The single emitters can be combined with extractor electrodes having diameters ranging from 150 to 250 μm. Some arrays have extractor electrodes with two different types of extractor electrode diameters allowing for coarse thrust modulation due to a variation in onset voltage.

Type	I.D.	Remarks
Single	24	Extractor el. diam. 150-250 μm
Single	28	Extractor el. diam. 150-250 μm
Single	32	Extractor el. diam. 150-250 μm
Array	20	Extractor el. diam. 200 μm
Array	20	Extractor el. diam. 200 and 250 μm

concept. The distance between emitter and extractor is given by

$$h_i = \sqrt{\left(\frac{d_{sp}}{2}\right)^2 - \left(\frac{l_e}{2}\right)^2} \tag{4.1}$$

where d_{sp} is the diameter of the insulator and l_e the diameter of the groove of the extractor electrode. A matrix of 3×5 holes is placed on the four corners of each chip to allow for different emitter-extractor spacings and to accommodate fabrication tolerances. The three chosen design spacings, h_i, are: 60, 56 and 51 μm. As will be shown later in section 4.6 the resulting spacing is in the order of 90 μm, which means that in the final assembly the ruby balls were not touching the buried oxide layer. Preliminary SEM measurements have also shown accuracies below 2 μm off the electrodes center axis. To acquire representative statistical data future work needs to focus on the test setup and consider aberration effects from the SEM and develop a test procedure to guarantee that the extractor electrode is placed horizontally during the measure. To measure tip-tilt of the extractor electrode a optical profiler could be used.

4.3   Design analysis

The method to evaluate the onset voltage presented in chapter 3 has been applied to the thruster to verify the design. The simulations have been done as input for the second generation of thrusters. The main dimensions are as illustrated in figure 3.3. The results and its implications will be discussed hereafter.

Figure 4.6a shows the dependence of the onset voltage on the distance between extractor and emitter. As expected a linear relationship can be seen as the extractor electrode is moved away. Figure 4.6b plots the onset voltage as a function of lateral sidewall distance from capillary emitter. Although in the microfabricated devices the adjacent structures are capillaries and not solid sidewalls this plot gives an indication
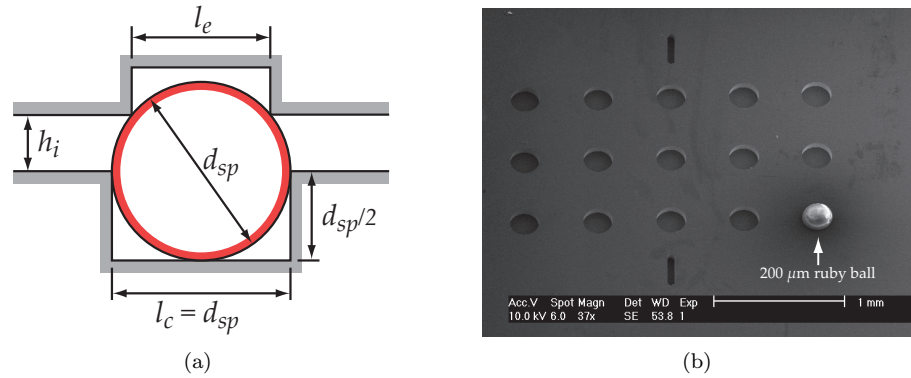
Figure 4.5: Ruby ball spacer for manual alignment of the emitter and extractor chips. (a) Schematic of a ruby ball inside a groove. (b) Marix of 3×5 grooves into which ruby balls are placed.

of the interference between capillaries. An increase in onset voltage is observed as the neighboring structure get closer and start interfering with the emitter. One should also note that the curve behaves in a similar way as experimental results reported in literature (Regele *et al.* 2002, Quang Tran Si *et al.* 2007). For a pitch greater than 200 μm the curve flattens and cross-talk becomes less important. Figure 4.6c shows the influence of extractor hole diameter for three different sidewall distances. Once again it can be seen that the difference between a 200 μm and a 250 μm sidewall distance is very small. Finally the impact of the capillary height is illustrated in figure 4.6d. In this plot it is important to notice that for a sidewall distance of 250 μm the gain in onset voltage between a capillary with 70 μm height and one with 150 μm is only around 50 V.

Resulting from the first generation of thrusters and the feasibility phase a 1:3.5 aspect-ratio between emitter tip diameter, d_i, and the capillary height, h_c, can be safely manufactured on wafer scale. This signifies that for a 70 μm high capillary a 20 μm diameter inner hole can be manufactured. The simulations also show that for these dimensions a pitch value of 250 μm does not cause interference between the emitters.

4.4 Single and arrays of capillary emitters

The process flow to manufacture the capillaries starts by cleaning the wafers at check-out, this "standard cleaning" procedure is also repeated before each oxidation step and includes a 10 min sulphuric acid bath, H_2SO_4, at $120°$C, an optional 1 min dip into buffered HF bath and a 10 min nitric acid bath, HNO_3, at $115°$C. Standard cleaning serves to remove any contaminants on the surface of the wafer that might diffuse into the wafer or contaminate the oxidation oven.

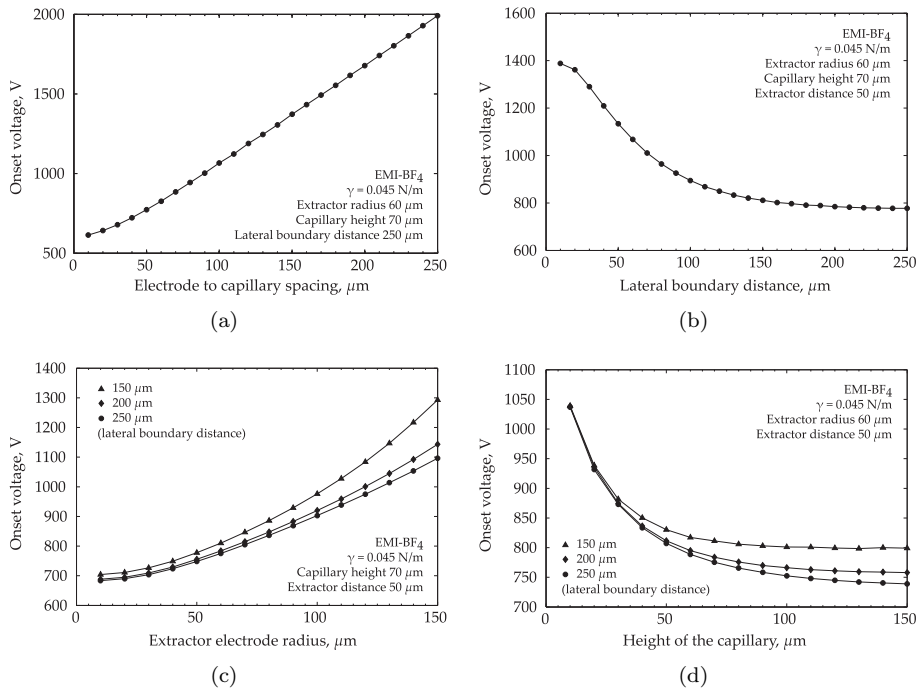The fabrication process, shown in figure 4.7, starts with steam oxidation of a

Figure 4.6: Plot of the onset voltage for a variation in (a) capillary emitter – extractor electrode distance, (b) distance between capillary and lateral sidewall, (c) extractor radius, and (d) height of the capillary emitter (lines are added for clarity).

silicon-on-insulator (SOI) wafer with a 100 μm device layer, 1 μm buried oxide and a 500 μm handle layer. After photolithography using AZ1518 photoresist the exposed fractions of the 1.5 μm thick oxide are removed in a buffered HF solution (a). This oxide layer defines the standoff structures which will protect the capillaries. Next a thin 70 nm buffer thermal oxide is grown (not shown in the figure) acting as stress relief for a subsequent 150 nm LPCVD nitride layer. The latter serves as local protection of the silicon during steam oxidation. Finally an additional 1 μm non-doped CVD oxide is deposited that serves as a hard mask (b). This oxide-nitride-oxide structure is patterned by reactive ion etching using an AZ1518 photoresist layer as mask. The following isotropic RIE (c) and *deep reactive ion etch* (DRIE) (Laermer and Shilp 1994) yield the characteristic outer shape of the capillaries (d). After photoresist stripping and CVD oxide removal the wafers are newly steam oxidized. The resulting 1.5 μm thick oxide serves as mask during the second DRIE which is performed once the nitride has been removed in a phosphoric, H_3PO_4, acid bath (e). This DRIE etches the inner hole of the capillaries (f). Once micromachining of the front side is done the back side of the wafer is etched up to the buried oxide using a combined oxide-photoresist mask (AZ4562). As the DRIE progresses the exposed SiO_2 is gradually removed. This creates a structure with two different heights during
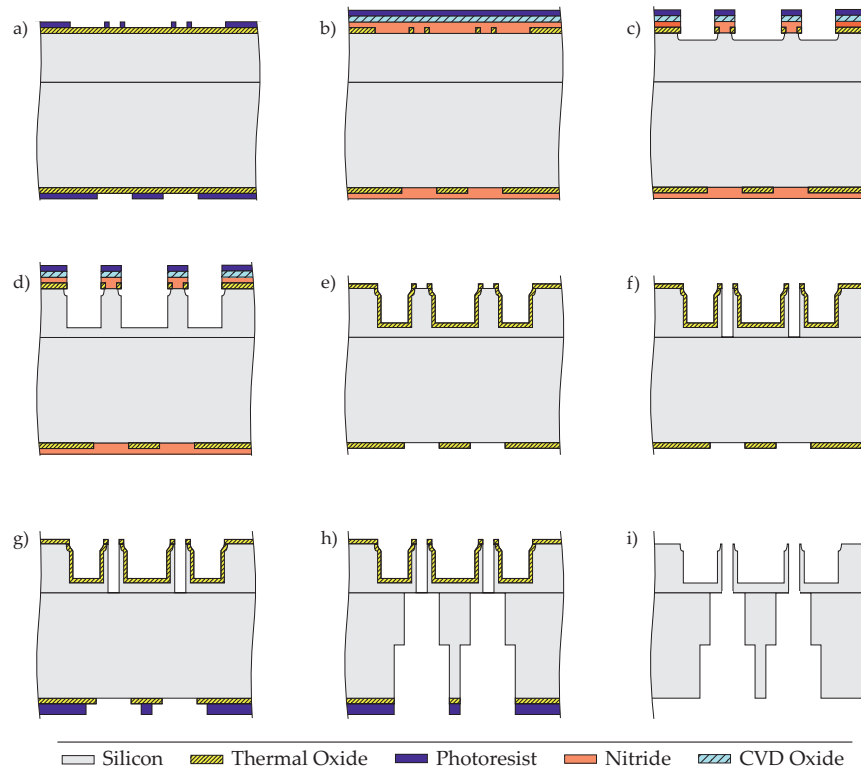
Figure 4.7: Illustration of the process flow developed to manufacture large arrays of capillary emitters. The buried oxide serves as etch-stop

one etch step (h). Finally the buried oxide is removed by means of a HF vapor etch (Overstolz *et al.* 2004) (i). Optionally the whole wafer can be oxidized to improve wetting properties and to change the electrics field behavior at the tip of the capillary.

4.4.1   High yield capillary tip design

Several process improvements were necessary to obtain a high percentage of functional capillaries. In particular the process steps involving the various layers necessary to manufacture the capillary's tapered tips have undergone several iterations. Defects such as bubble formation during CVD oxide deposition and nitride layer lift-up during thermal oxidation have been investigated and removed. This "lessons learned" section will discuss these process improvements in more detail.

A first defect cause was a reaction between doped CVD oxide deposited onto the layer of nitride (Si_3N_4). In subsequent steps this lead to bubble formation. Their exact provenance is not clear and has not been investigated further as the problem was solved by using a 1 μm thick *non* doped CVD oxide.

The second defect was observed on several wafers as an unintentional oxidation of
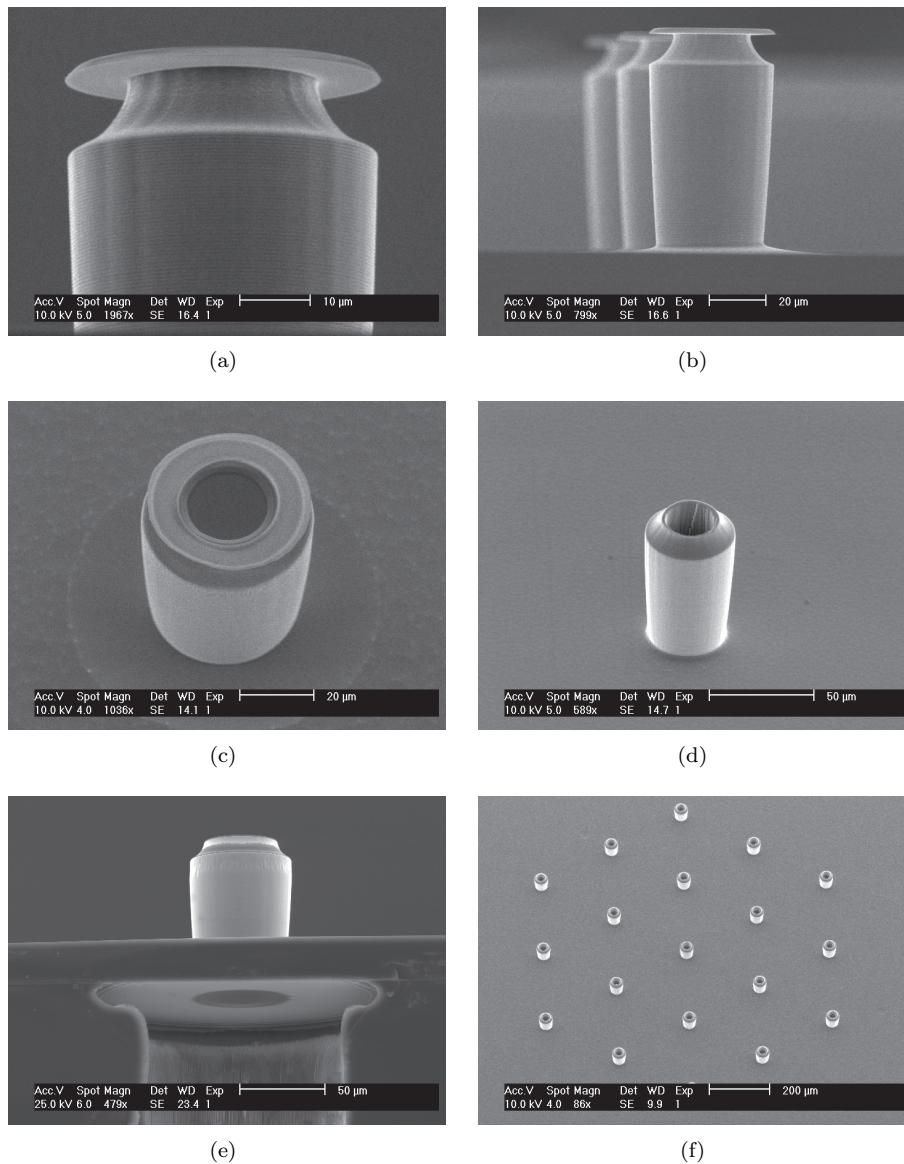
(a)

(b)

(c)

(d)

(e)

(f)

Figure 4.8: SEM photographs of the manufacturing process. (a),(b) Capillaries after the isotropic RIE and anisotropic DRIE step. (c) Capillary after thermal oxidation and nitride removal. The dark surface in the middle of the capillary tip indicates the absence of oxide. (d) Capillary after the second DRIE. (e) Cross section of a capillary. Notching due to overetch at the burried oxide can be clearly seen. (f) Arrays of 19 capillaries arranged in a hexagonal pattern.
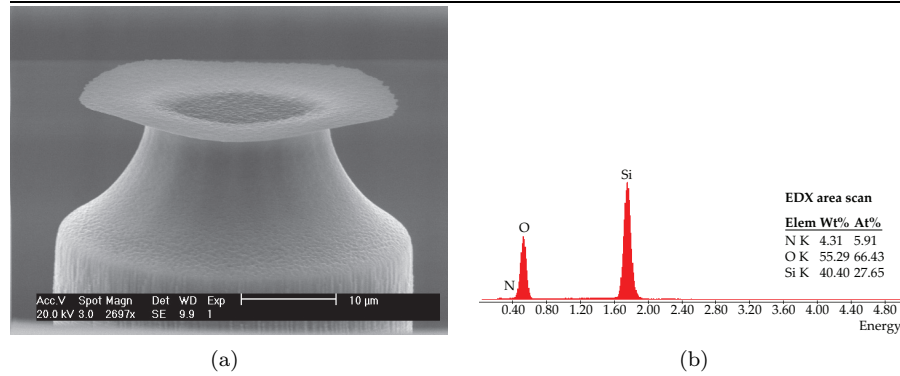
Figure 4.9: Observation of the unintended oxidation of the capillary tip. (a) SEM photograph of the oxide ring surrounding the tip after nitride removal. (b) SEM/EDX analysis of the tip region indicates the presence of SiO_2.

the capillaries tip surface, making a DRIE of the central hole impossible. Figure 4.9 shows a SEM photography of a defective capillary tip after oxidation and nitride removal. The remaining oxide ring is clearly visible. The EDX analysis confirms the presence of SiO_2 on the flat surface of the tip and on the ring surrounding it and indicates an almost complete absence of atomic nitrogen. An initial hypothesis of an oxynitride can therefore be discarded. The oxidation of the tip surface can be explained by a lift-up of the nitride during oxidation, as is illustrated in figure 4.10. The oxide growth pushes the nitride upward until it breaks (good tips) or lifts-up and water vapor penetrates and oxides the surface below the nitride (bad tips).

Additional problems can arise due to the oxidation of the nitride layer and the creation of a nitride at the interface between the silicon and the buffer oxide. This effect has also been observed in MOS manufacturing when applying the LOCOS (Local Oxidation of Silicon) process. Nakajima *et al.* (1979) report an increased defect density in gate oxides for steam oxidation, but none for dry oxidation when applying the LOCOS process. They believe that the following reactions take place

$$
\begin{aligned}
Si_xN_x + H_2O &\rightarrow SiO_x + NH_x \\
Si + NH_x &\rightarrow Si_xN_x + H_2.
\end{aligned}
\tag{4.2}
$$
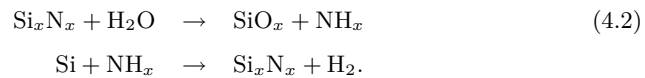
The following simple solutions were found to remove these defects. To minimize the oxidation of the silicon nitride the steam oxidation was done at $950°C$ instead of $1100°C$. To avoid the lift-up of the silicon nitride during oxidation the contact area between the initial SiO_2 ring and the capillary tip was increased by decreasing the duration of the first isotropic plasma etch.
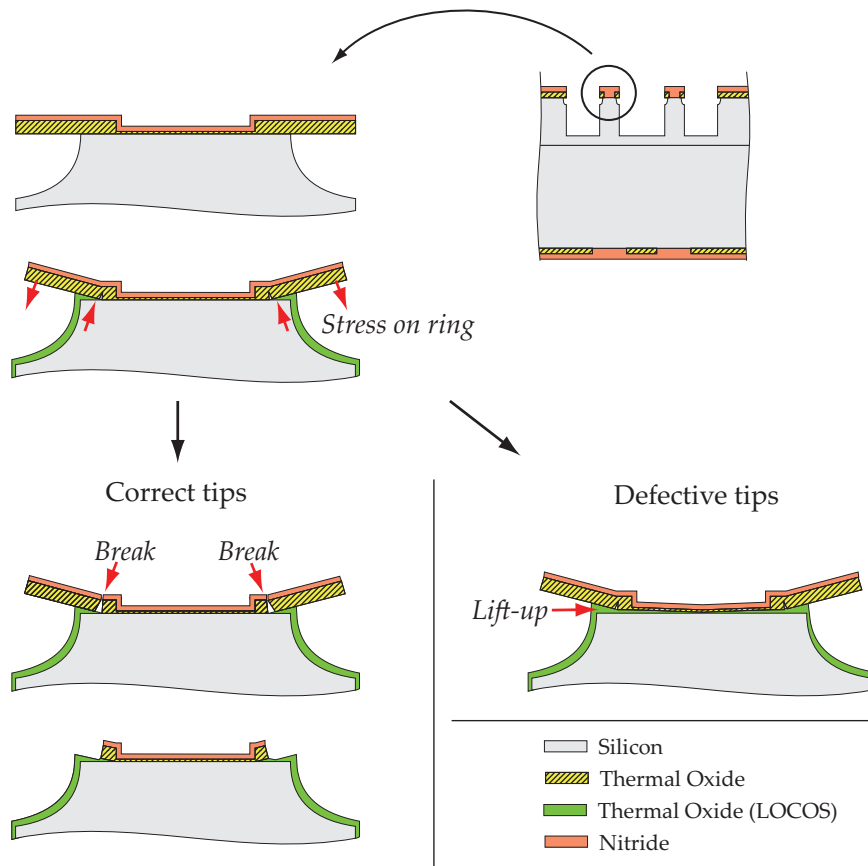
Figure 4.10: Illustration of the break up of the nitride-silicon dioxide ring. If the surface of the silicon ring attached to the capillary tip is too small the ring is lifted up and oxidation occurs below the nitride.

4.4.2 Post fabrication treatments

Hydraulic impedance is important when spraying with arrays of capillaries. As small differences are always present between various emitters in an array of capillaries some emitters will start spraying faster than others. If the hydraulic impedance is too low these emitters will tend to draw liquid from the other capillaries, leading, in the worst case, to chip flooding. To increase the hydraulic impedance microspheres were introduced into the capillaries after the emitter chips were diced.

Tests were done with hydrophilic silica microbeads in water obtained from Bangs Laboratories. A method to fill the capillaries with beads having a mean diameter of 4.7 μm and 0.97 μm was established:

1. Cleaning and drying of chips (optional)

2. Sonication of the beads for 5 minutes to create a dispersion

3. Droplet of isopropyl alcohol is placed on the reservoir side of the chip

4. Droplet of microbeads in water solution placed on the reservoir

5. Sonication of the chip with microbeads for 2 minutes (optional as sonication can cause damage)

6. Drying of the chip under vacuum for 24 hours

7. Silanization of the chip using $SiCl_4$

The result are shown in figure 4.11a and 4.11b. The silanization process serves to hold the beads together in the capillary hole. The SEM photograph in figure 4.11c shows the transformation of the initially round beads into a hexagonal shape. Although the process described above has yield good results for single and arrays of capillaries the sonication of the chip has, in certain cases, caused damaged to the beads. The results is an accumulation of bead debris at the tip during drying and the destruction of the chip (fig. 4.11d). The best solution is to avoid sonication by using smaller beads. If larger beads are needed creating dispersions in a solutions of water and isopropyl alcohol has also led to acceptable results.

4.5 Extraction electrodes

Four different fabrication processes were developed to manufacture the extractor electrodes. As for the capillaries the extractors are microfabricated. All designs feature a dedicated extractor hole for each capillary. In three designs all the capillaries in an array are addressed simultaneously while the fourth allows individual addressing of a single electrode in an array. These four designs can be summarized as follows:

a) Electrode chip with simultaneous capillary addressing (with integrated insulator)

b) Electrode chip with individual capillary addressing (with integrated insulator)

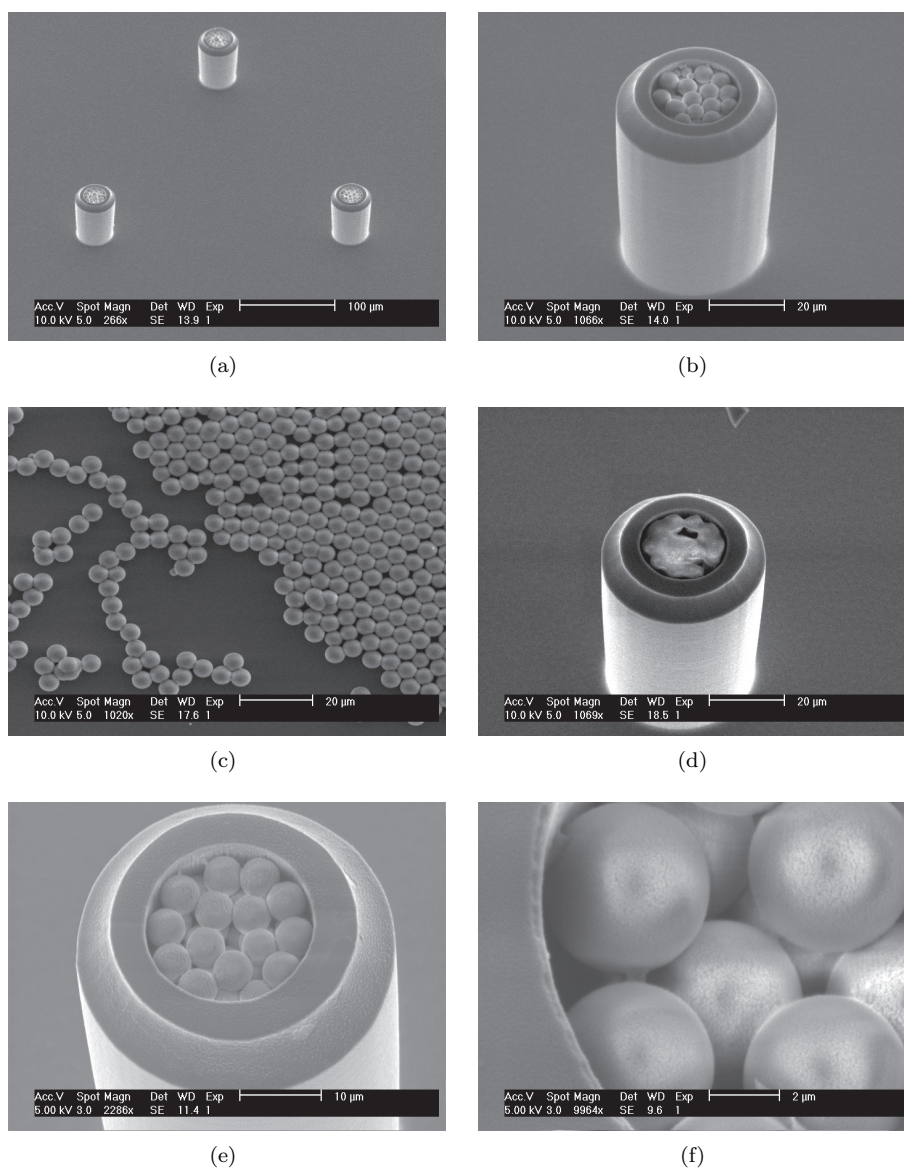c) Electrode chip with simultaneous capillary addressing (without insulator)

(a)

(b)

(c)

(d)

(e)

(f)

Figure 4.11: SEM photographs of the 4.7 μm silica microbeads inside the capillaries. They were introduced to increase the fluidic impedance of the capillaries.

Figures 4.12 and 4.13 summarize the three process flows. Although all electrode designs were tested and shown to operate, configurations (a) and (b) were first generation designs and only limited spray data could be obtained as lifetimes were very short.

4.5.1 Electrodes with integrated insulator

The extractor electrodes with integrated insulators share the common fabrication steps described hereafter. The process is based on a SOI wafer with 50 μm device, 2 μm buried oxide and a 400 μm handle layer. A 50 μm thick device layer was chosen to support the freestanding extraction electrode grid. After wafer cleaning the alignment marks are etched into the silicon. This is done by spinning and patterning a 1.8 μm thick AZ1518 photoresist layer (1) and transferring this pattern 500 nm deep into the silicon by plasma etching. Once completed the photoresist is stripped (2). Now the electrodes are etched trough a DRIE step on the device layer (3). As etch mask a 2.3 μm thick AZ1518 photoresist layer is used. The small pitch of 250 μm between the emitters and the large divergence of the beam ($\approx 30°$ half angle) requires that the capillary to extractor electrode distance is kept small to avoid the spray to hit the border of the extractor electrode. This minimum extractor electrode diameter, d_{min} can be easily calculated

$$d_{e,min} = (h_e + h_i)\tan\alpha_s \qquad (4.3)$$

where h_e is the height of the extractor electrode, in the present case 50 μm, and h_i the height of the insulator. For an extractor electrode diameter of 200 μm the maximum insulator height, h_i, is 123 μm while for a diameter of 100 μm the maximum height is 37 μm. On the other hand the insulating layer between the source and extractor needs to be thick enough to support the large potential difference (several kilovolts) between the electrodes. These two constraints cannot be achieved with a Borofloat or Pyrex wafer of ordinary thickness (usually $>$ 150 μm) or a thick thermal oxide layer ($<$ 3 μm). To circumvent this problem a Borofloat wafer is attached to the extractor electrodes by anodic bonding (4) and thinned down to 100 μm in a HF 20% bath (5). As the surface roughness after the HF bath is not homogeneous an additional chemical mechanical polishing (CMP) step could be added. This would be particularly useful if the whole stack capillaries-insulator-extractor were to be assembled at wafer level through a second anodic bonding step (not done within this thesis).

Electrode chip with simultaneous capillary addressing

In this configuration all the emitters are addressed simultaneously by applying the same potential to the entire extractor electrode chip. Once the front side has been prepared (steps 1-5) the handle layer is etched by applying a 11 μm thick AZ4562 photoresist layer, patterning it and performing a DRIE up to the buried oxide (6a). Using bulk silicon as etch mask for the Borofloat, as suggested by Corman *et al.* (1998), the wafer stack is placed in a HF 20% bath. The hydrofluoric acid removes
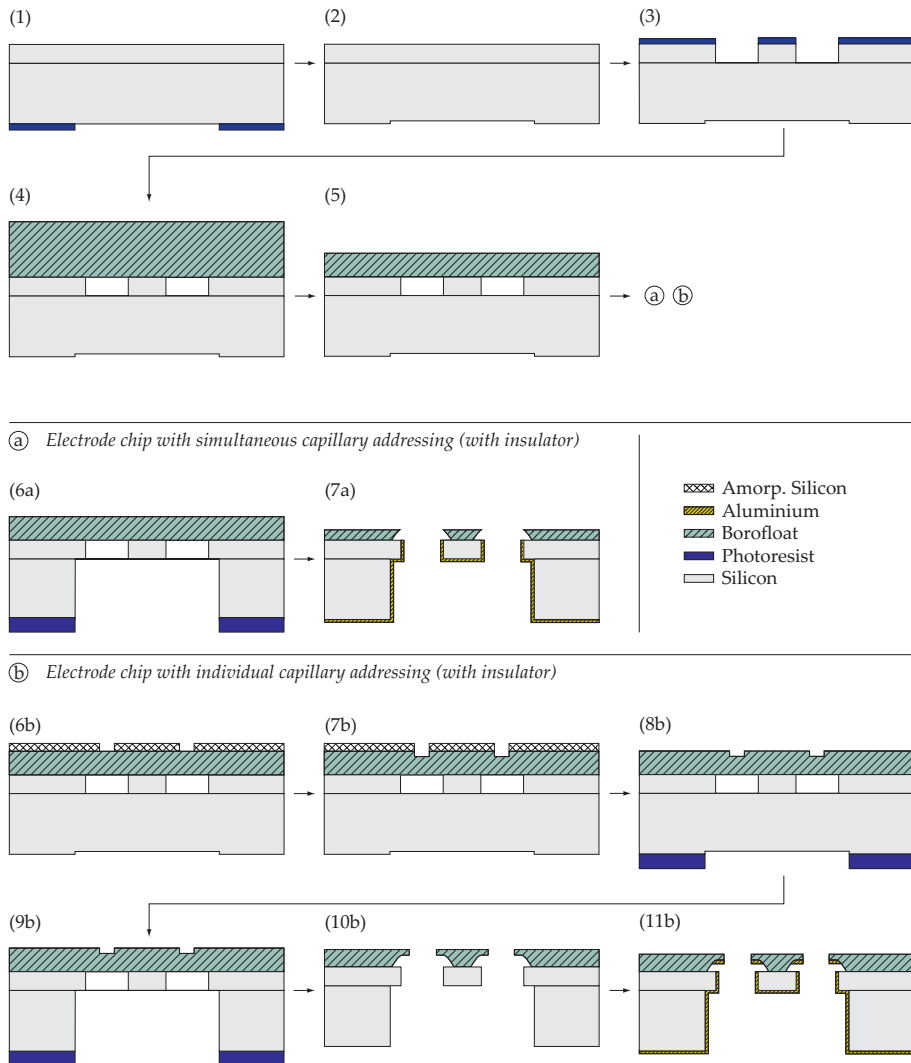
Figure 4.12: Manufacturing process flow of the extractor electrodes with integrated Borofloat insulator for wafer scale assembly: (a) common electrode, (b) individual addressable electrodes.
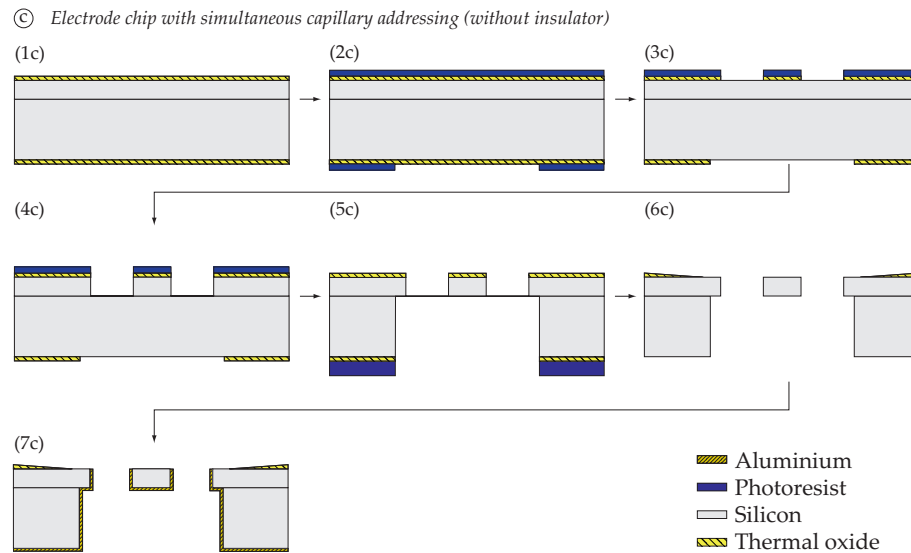
Ⓒ *Electrode chip with simultaneous capillary addressing (without insulator)*

(1c) (2c) (3c)

(4c) (5c) (6c)

(7c)

	Aluminium
	Photoresist
	Silicon
	Thermal oxide

Figure 4.13: Manufacturing process flow of the extractor electrodes without insulator for chip level assembly: (c) common electrode

the buried oxide layer and attacks the Borofloat from both sides. The stack is left in the hydrofluoric acid bath until the extractor holes in the Borofloat have been opened and the desired insulator height is reached. Finally the handle layer is metallized by evaporating aluminium onto it (7a), this provides an optimal electric contact with the support structure. Figure 4.14a shows a cross section of the assembled thruster. As the device was broken in two for this SEM photograph, the device layer containing the capillary has been broken off the buried oxide and vertically displaced, neverthteless the insulator-extractor electrode stack can be clearly seen. One should also notice the lateral underetch of the Borofloat which is 1.5 times larger than the vertical one.

Electrodes with individual addressing

From an operational point of view the possibility to address emitters individually is very appealing. In this second design a process flow was investigated in which the electrodes are not formed by the bulk silicon, but by evaporating a metal layer onto the Borofloat using the silicon as shadow mask to define the individual electrodes. The first five manufacturing steps (1-5) are done as described above. To serve as a shadow mask the silicon needs to be recessed with respect to the Borofloat, a 2 μm thick amorphous silicon layer is therefore deposited onto the Borofloat and patterned (6b). The Borofloat is then etched 15 μm deep with a DRIE procedure (7b), shown in figure 4.14b and the amorphous silicon is removed in a KOH bath (8b). The handle layer is now structured using a thick AZ4562 photoresist as mask and performing a DRIE (9b) and, as for the common addressable electrodes, placed in a HF 20% bath to attack the Borofloat and open the extractor electrode holes (10b). Finally a layer

of aluminium defining the electrodes is deposited (11b).

A SEM photograph of the resulting extractor electrode is shown in figure 4.14c. The grooves in the device layer of the silicon leading to the extractor electrodes (detail shown in figure 4.14d) define the shadow mask for the metal deposition, the electrical contact is done through wire bonding. Figure 4.15 shows a fully assembled thruster glued onto a printed circuit board, electrical contact is achieved through gold bond wires.

4.5.2   Electrodes without insulator

As mentioned before electrodes without insulator were designed for the second generation devices. This configuration was chosen to simplify chip scale assembly and disassembly during testing. A matrix of groves was engraved onto the capillary and extractor wafer to allow a simple manual alignment procedure using 200 μm diameter ruby balls. The electrodes in this chip design are all addressed simultaneously.

Fabrication starts once again with a SOI wafer (50/2/400) and an oxidation (1.5 μm) step after the standard cleaning procedure (1c). Alignment marks are then transferred into the silicon dioxide on the handle layer of the wafer in a buffered HF (2c), using a 1.8 μm thick photoresist (device layer is protected by a photoresist). The same procedure is then repeated on the device layer (3c) and then a DRIE is done up to the buried oxide (4c). The handle layer is now etched up to the buried oxide with another DRIE and an AZ4562 thick photoresist mask (5c). Finally the buried oxide is removed from the handle layer side by vapor etching (6c) and metalized with a layer of aluminium to decrease contact resistance (7c).

4.6   Packaging & Assembly

Extractor electrodes with integrated insulator were first generation devices intended for wafer scale assembly, but for the first tests these wafers were diced and assembled manually at chip level. The missing alignment features and the necessary gluing step led to low alignment precision. Further the investigation of failure causes required the destruction of the thruster to separate extractor electrodes from the capillaries. Based on this experience a new method was sought to perform rapid and precise chip level assembly. The solution was found by including grooves on the chips and placing ruby balls into them (as previously described).

Figure 4.16 shows SEM photographs of an assembled second generation thruster using ruby balls as insulators. The assembly is done manually by placing the 200 μm diameter ruby balls into the groves on the chips using a stereomicroscope and tweezers as aids. The height profile of the thruster has been taken with an optical profiler. As the thickness of the extractor electrode is 50 μm the spacing between capillary and the extractor electrode is around 90 μm (fig. 4.17). This is an important deviation from the initially calculated value of 60 μm. Complementary profile data for multiple chips, before and after testing, show that the ruby balls stand off the capillary chip
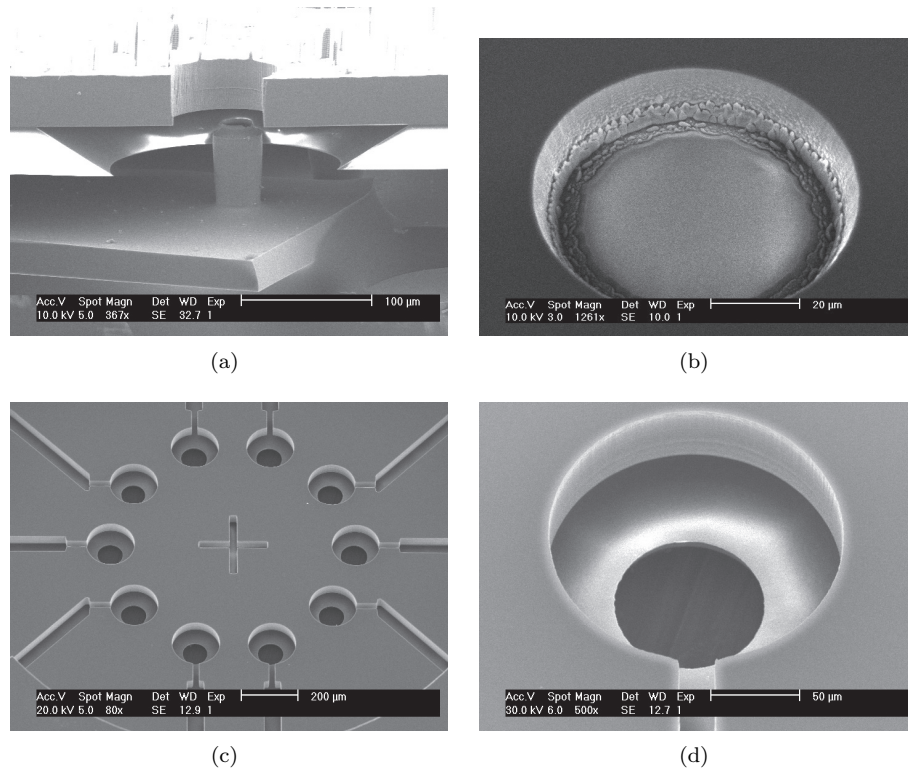
(a)

(b)

(c)

(d)

Figure 4.14: SEM photographs of the extractor electrodes with integrated Borofloat insulator. (a) Cross section of an assembled thruster with common addressable extractor electrode. The insulator appears white due to charging. During sectioning the capillary device layer on the capillary chip broke off and was displaced upwards. (b) DRIE of the Borofloat, the hole has a depth of approximately 15 μm. (c) Matrix of 10 individually addressable extractor electrodes. The electrodes are evaporated onto the Borofloat insulator using the silicon wafer as shadow mask. The grooves serve to connect the electrodes with a wire bond pad. (d) Detail of an extractor electrode hole. The grove on the bottom of the picture connects the electrode to a wire bond pad.
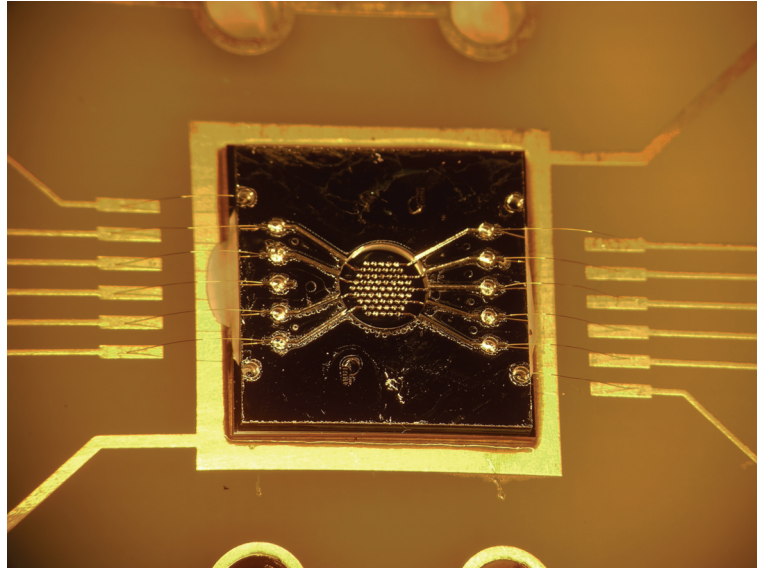
Figure 4.15: Photograph of a fully assembled thruster with individually addressable extractor electrodes. Contact between the printed circuit board and the extractor electrode is done through a gold bond wires.

by 115 μm (instead of 100 μm). Assuming a similar error on the extractor side the 30 μm difference becomes reasonable.

4.6.1   Glass-Ceramic Package

Although a printed circuit board made of epoxy provides a simple interface for testing in a laboratory environment it will not satisfy the environmental constraints a thruster will undergo in space. In particular the harsh thermal environment in space requires an active control of the thrusters temperature to avoid the fuel to freeze or a drift of thruster performance. To integrate a heater, thermal sensor, high voltage electric connections and fluid handling into a miniaturized package a packaging technology known as *Low Temperature Co-fired Ceramic* (LTCC) was chosen (Gongora-Rubio *et al.* 2001). This technology consists in stacking sheets of glass-ceramic tapes, each containing structural or electric features, into a three dimensional structure. After pressing the stack together, this laminated structure is then sintered in an air furnace at 850-900°C.

The features on each layer may include holes, capacitors, resistors, electrical connections or vias. Holes are either drilled by laser or mechanical punching. Electrical features such as resistors are deposited through screen printing of pastes having various properties. The properties of the LTCC sheets include a heat conductivity of 3.3 W·m^{-1}K^{-1}, a density of 3.1 g·cm^{-3} and feature a breakdown voltage of 1 kV/25 μm and are therefore well adapted to high voltage operation.

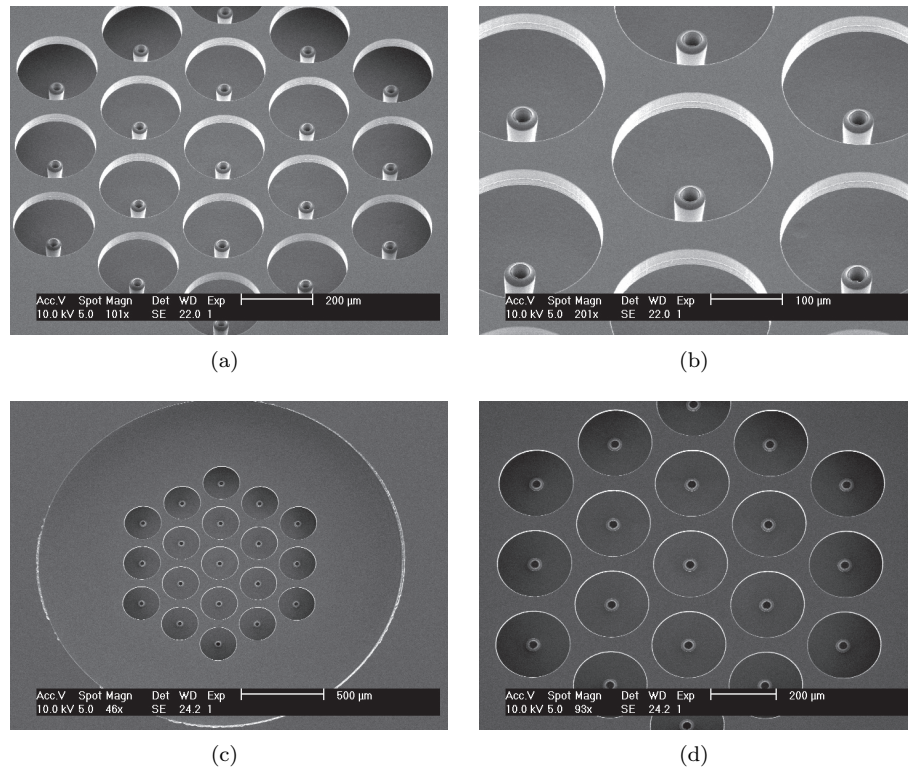The developed prototype package consists of five ceramic sheets and includes an

Figure 4.16: SEM photographs of assembled second generation thrusters. Alignment has been achieved by placing 200 μm diameter ruby balls into groves in the capillary and extractor chip.
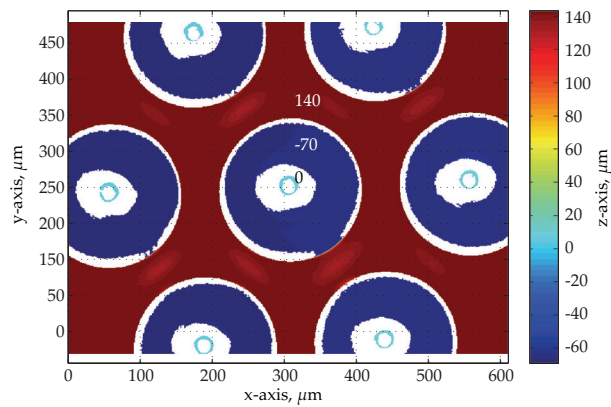

Figure 4.17: Height map of the integrated chip acquired with a Wyko NT 1100 optical profiler. The downstream part of the extractor electrode is at 140 μm. The capillary tip is at zero and stands-off 70 μm. The extractor electrode thickness is 50 μm and thus the capillary tip to extractor distance is 90 μm.

1 cm

(a)   (b)
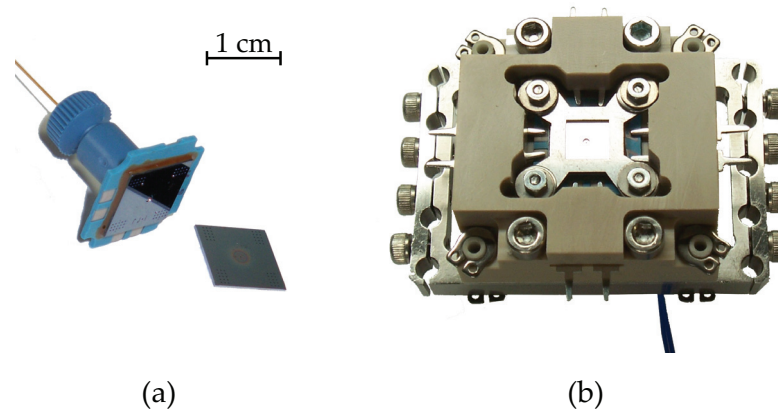
Figure 4.18: Photograph of (a) the capillary chip and fluidic interface integrated onto the LTCC support and (b) a fully integrated thruster using the PEEK interface.

interface for an Upchurch Nanoport, a network of PTC resistors (for device heating and temperature measurement) and a fuel presence sensor. The PTC resistors have been integrated to heat the emitters and measure their temperature. They have been applied onto a ceramic sheet by serigraphy and are, once the ceramics have been stacked and sintered, buried within the device and thus electrically separated from the fuel and the chip. A fill detector has also been included to measure the fill status of the thruster. The LTCC onto which capillary chip has been glued (EPOTEK H70S) is shown in figure 4.18a.

4.6.2   PEEK Support structure

The support structure allows to integrate the LTCC with the glued capillary chip and the extractor electrode into a thruster assembly. The support then connects to the mechanical, electric and fluidic interfaces of the vacuum chamber. The structure is manufactured from PEEK, a semicrystalline thermoplastic exhibiting good chemical resistance and is compatible with ultra-high vacuum applications. The mechanical design has been done in such a way that the load on the extractor electrodes is minimized to avoid mechanical fracture of the ruby balls or the alignment grooves and thus premature failure of the thruster. The picture in figure 4.18b shows a fully integrated thruster.

4.7   Conclusion

In this chapter the manufacturing process of the micro-thruster has been reviewed. A design and a manufacturing process have been developed for the capillary chips, from which the liquid is emitted. The extractor electrodes are an integral part of the thruster and three different concepts have been presented and manufactured allowing

either chip level or wafer level assembly of the microfabricated parts of the thruster. These design variations of the extractors allow either individual or common addressing of the individual electrodes.

The process flow of the capillary emitters has undergone several improvements. By choosing conservative dimensions in the final design (e.g. aspect ratio of 1:3.5 for the capillary stand-off height) high manufacturing yield and reproducibility has been achieved and large arrays of emitters have been manufactured at wafer scale with barley no defects. Further, a post-processing procedure to increase the hydraulic impedance of the capillaries by introducing silica beads into the capillaries and fixing them through a silanization step has been introduced.

Design maturity of the extractor electrode is excellent for the electrode without insulator for chip level assembly (see fig. 4.13, design–c). These second generation devices have been successfully tested and shown to be robust during thruster operation. Of the first generation of devices the electrode design capable to simulataneously adress all emitters (fig. 4.12, design–a) is also very mature. An open question remains how to improve the surface quality of the Borofloat wafer after HF 20% etching in order to perform wafer scale assembly by anoding bonding the emitter-insulator-extractor stack togeter. The third extractor design (fig. 4.12, design–b) remains still experimental. The thin membrane of Borofloat after the DRIE is very fragile and wire bonding has been rather difficult and in spray tests the devices have only exhibited a very short lifetime. An improvement could be the replacement of the DRIE step with a wet etch. Preliminary investigations to develop an amorphous silicon mask capable to withstand the hydrofluoric acid bath have been promising for two deposited layers each having a thickness of 300 nm.

Finally a package compatible with the harsh environment found in space has been introduced. The developed prototype package, using LTCC technology, allows to design a compact and multi-functional interface for the thruster, while integrating electrical and micro-fluidic functions into it. Integration of the thruster assembly (using the PEEK interface) has been straightforward and led to excellent reproducibility.

Chapter 5

Experimental results

THRUSTER performance is presented in this chapter. It starts by introducing the experimental setup which was built during the thesis to characterize the beam energy and current. The results obtained with first generation devices are then presented and correlated with the developed onset voltage model.

The middle part of the chapter focuses on tests conducted with second generation devices. Beam energy and current measurements for single capillaries are reported for different thruster configurations and the results of a first life test are presented and failure modes analyzed.

Finally operational issues are discussed at the end of the chapter including liquid priming and cleanliness issues, two key factors for the success of spray testing.

5.1   Experimental setup (EPFL)

The test bench consists of a vacuum chamber for thrust performance characterization and a second chamber for fuel storage (figs. 5.1 and 5.2). The latter is also necessary to degas the ionic liquid before filling the thruster and thus to avoid bubble formation due to the water vapor and other contaminants present in the the liquid. Both chambers are connected through a silica capillary tube to transfer the liquid from the reservoir to the thruster. The main chamber used for thruster characterization consists of a six-way cross onto which a turbomolecular pump (Varian Turbo-V 551, 550l/s) is directly attached through an ISO 160 interface. The base pressure attained in the main chamber is below 3×10^{-7} mbar and in the fluid reservoir below 5×10^{-3} mbar.

For spray testing the emitter capillaries are connected to a high voltage source and operated at positive and negative voltages. Switching is either done manually or by means of a high voltage switch designed to change between a positive and negative source at a frequency of $f < 1$ Hz (fig. 5.3). The core of this system are two Meder (H12-1A83) high voltage reed relays switching between the positive and negative power supplies. In this simple setup no precautions are taken to avoid relay bouncing, but a third relay is used to avoid both sources being on-line simultaneously

and two 10 kΩ resistors further serve to protect from short circuits. Finally a simple voltage divider provides a monitoring feedback of the output voltage signal and serves as bleed resistor.

During all tests the extractor electrodes are grounded and the emitter capillaries biased to high voltage. The electrospray current is measured by means of a Faraday cup (Kimball Physics FC-72A) attached to a picoammeter (Keithley 487) which has a built-in high speed amplifier allowing to display the current signal in real time on an oscilloscope. A grid placed in front of the Faraday cup and biased to -50 V serves to suppress secondary electrons. To analyze the energy spread of the beam a retarding potential grid is placed in the flight path. As high voltage sources two Stanford Research Systems (PS350, ±5 kV) and a FuG Elektronik (HCN 35-6 500, ± 6.5 kV) power sources are used.

The liquid feed system consists of a reservoir placed in a separate vacuum chamber connected to the main chamber through a silica capillary (360 μm o.d., 150 μm i.d.). The setup allows to lower the feed capillary into the reservoir by means of a linear motion feedthrough. For the various liquid interfaces Upchurch Scientific fluidic elements are used and to remove any remaining bubbles trapped in the liquid a Teflon AF capillary tubing is inserted into the flowpath. For long term testing a gate valve allows to seal off the reservoir from the vacuum pump. To pressurize the reservoir and push the liquid through the capillary into the thruster a nitrogen purge valve with gradual control is installed.

Pressure within the system is monitored by three Bayert-Alpert Pirani combination gages (Inficon BPG400). The high voltage sources and the pressure gages are connected to a LabVIEW based data logging and control system. Monitored signals include chamber pressures, voltages and spray current at a slow rate (< 0.33 Samples/s). Additionally an installed data acquisition card permits also to monitor and record output voltage and current at higher acquisition rates (> 1 kSample/s).

5.1.1 Beam parameters - characterization tools

The beam current is measured by means of a *Faraday Cup* (FC). It consists of a metal cup which is placed in the charged beam's path. The cup is held at a constant potential, at ground in the present case, $V_{os} = 0$ V. The current is related to the charge in the following way

$$I_F = \frac{N}{t}q. \tag{5.1}$$

In the expression above N/t corresponds to the number of charged particles per time unit, q is the particles charge and I_F is the generated current. Figure 5.4 shows a simplified schematic of the current-to-voltage converter circuit inside the Keithley 487 Picoammeter. The output voltage V_{OUT} is

$$V_{OUT} = -I_F \cdot R_F + V_{os}. \tag{5.2}$$

As an example for a 200 nA range the instrument's internal resistance, R_F, is 10 MΩ resulting in a maximum output voltage of $V_{OUT} = -2$ V.
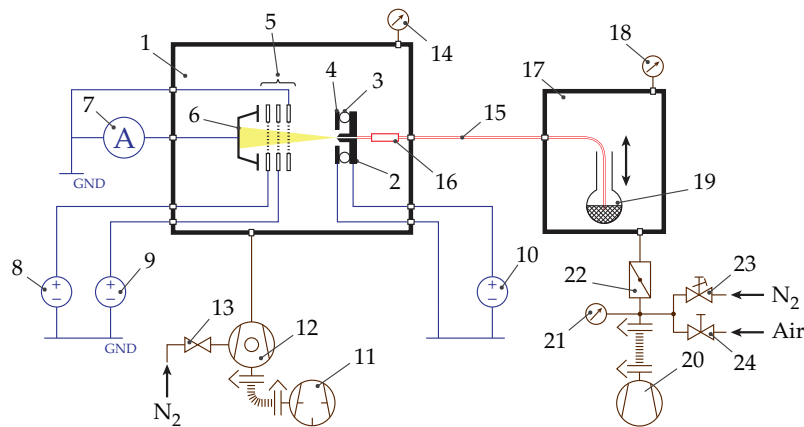
Figure 5.1: Schematic of the test bench for thruster characterization at EPFL. The main chamber into which the thruster is mounted allows the characterization of beam current and retarding potential analysis. The second vacuum chamber contains the liquid reservoir and can be pressurized. The liquid is pumped from the reservoir to the thruster through a 150 μm inner diameter silica capillary. A detailed list of test rig elements is given in table 5.1.

Table 5.1: Table listing the various test bench elements shown in figure 5.1.

|	Thruster characterisation		Liquid feed system
1	Vacuum chamber	15	Feed capillary
2	Capillaries	16	Liquid outgassing tube
3	HV insulator (ruby balls)	17	Vacuum chamber
4	Extractor electrodes	18	Pressure gauge
5	Retarding potential measurement	19	Liquid reservoir
6	Faraday cup	20	Pumping station
7	Picoammeter	21	Pressure gage
8	Voltage source (supression grid)	22	Gate valve
9	Voltage source (retarding grid)	23	Nitrogen valve
10	Voltage source (emitter)	24	Air valve
11	Roughing pump		
12	Turbomolecular vacuum pump		
13	Nitrogen valve		
14	Pressure gauge		
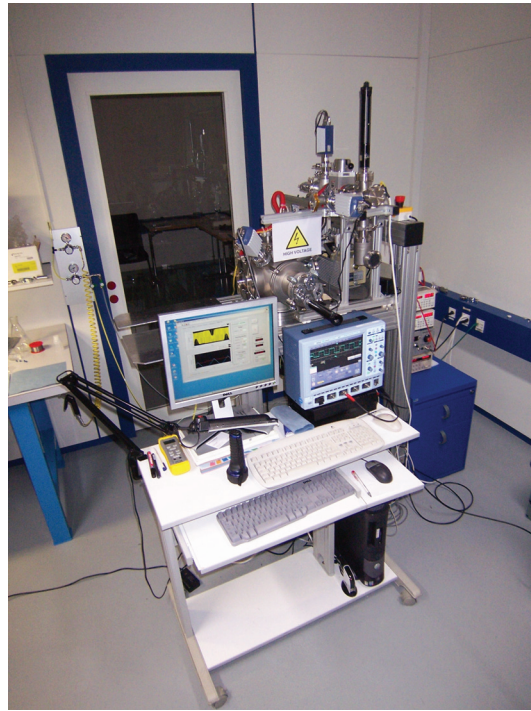
Figure 5.2: Photograph of the test bench showing the test rig including the LabView based control and data monitoring system.
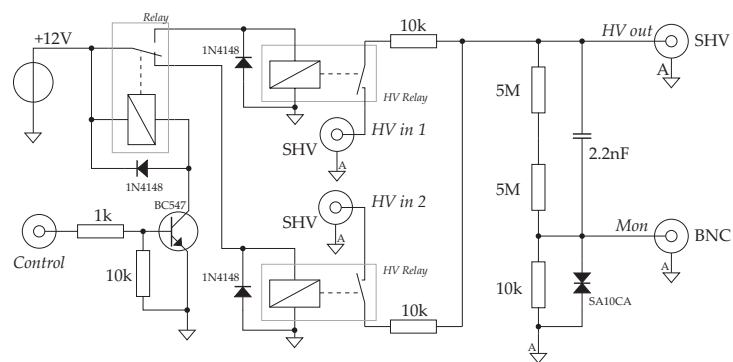

Figure 5.3: Electrical diagram of the high voltage switch. Two reed relays from Meder (H12-1A83) allow switching voltages up to 10 kV. Switching is controlled by an external impulse. To avoid both HV sources being on-line simultaneously a third mechanical relay is added. The switch also provides a voltage monitor output signal.
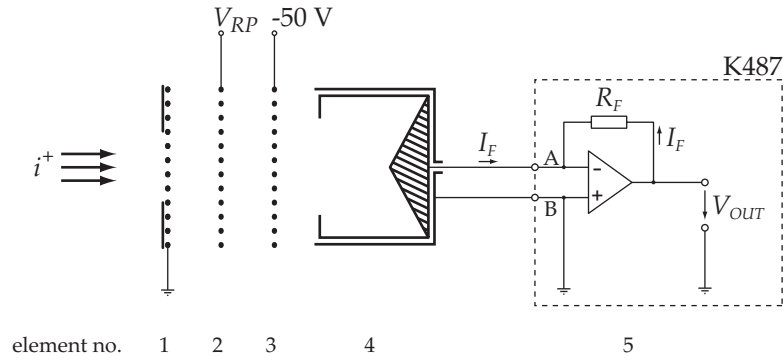
Figure 5.4: Illustration of the retarding potential analyzer (RPA). The first grid (1) establishes the ground plane. The retarding potential is applied to the second grid (2) and the third grid (3) suppresses secondary electron emissions from the Faraday cup (4). The current to voltage converter (5) inside the Picoammeter is shown schematically. Input impedance is practically zero as point A behaves as a virtual ground.

The *retarding potential analyzer* (RPA) allows to determine a particles energy. The retarding potential grid acts thereby as a barrier only allowing particles to pass having a greater kinetic energy than the stopping potential

$$\frac{1}{2}m_0 v_e^2 > qV_{RP}, \tag{5.3}$$

where m_0 is the particles mass, v_e its speed, q the charge and V_{RP} the retarding potential. Differentiating the measured particle current $i(t)$ with respect to V_{RP} yields the energy density distribution of the beam. For the experiments reported in this work a single grid design was chosen for the RPA, as shown in figure 5.4.

The single grid system does not represent a perfect equipotential plane and causes the retarding potential to 'sag' between the grid wires leading to a deviation from the applied retarding voltage and thus affecting the resolution of the RP measurement. The largest deviation occurs at the center between grid wires and has been described analytically by Enloe and Shell (1992)

$$\frac{\Delta V_{RP}}{V_{RP}} = 1 - \left(\frac{2\pi(h_p/a) - \ln 4}{2\pi(h_p/a) - 2\ln\left(2\sin\left(\pi r_w/a\right)\right)} \right), \tag{5.4}$$

where h_p is the distance between grounded and biased planes, a the distance between the centers of the wire and r_w the radius of the grid wires. In the present test setup this sag ($\Delta V_{RP}/V_{RP}$) might therefore be as much as 5%. This means that for an retarding potential of 1000 V the maximum resolution is around 50 V.
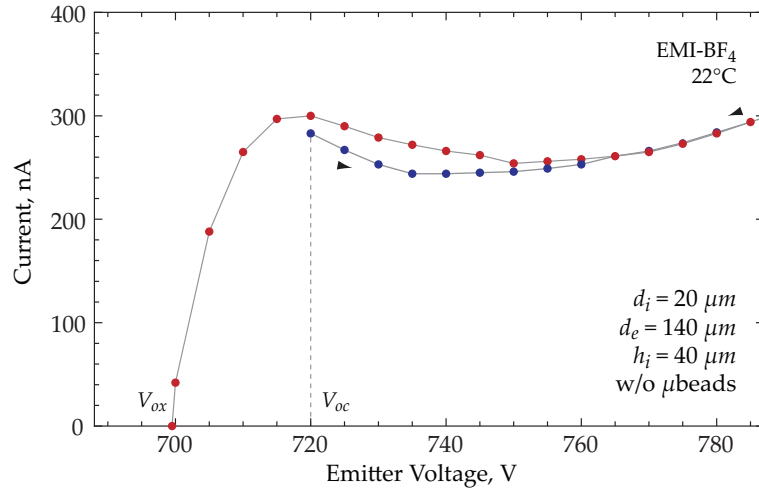
Figure 5.5: Current-voltage curve of a capillary emitter with 20 μm i.d. and a 140 μm diameter extractor electrode spaced 40 μm from the emitter. The sprayed liquid is EMI-BF$_4$ which is passively fed to the capillary (lines between data points only added for readability).

5.2 First generation devices

The first generation of thrusters were operated by simply placing a droplet on the backside of the chip. The main difficulty of this approach is spray initiation as the liquid does not tend to wet the tip's surface and the electric field is not able to "draw out" the liquid. All chips from which results were obtained had been initially filled with EMI-BF$_4$ and were, after unsuccessful operation, then rinsed in acetone and isopropyl alcohol. As these first generation devices could not be disassembled it is assumed that after cleaning the remaining contamination (glue, ionic liquid, etc.) on the tip of the capillary aided the wetting process during the second spray attempt.

Figures 5.5 and 5.6 show current-voltage plots for single 20 μm inner diameter capillary emitters spraying EMI-BF$_4$ with a 140 μm diameter extractor electrode spaced at 40 and 25 μm, respectively. The measurements were done by first increasing and then decreasing the voltage. Once the onset voltage is reached the spray initiates and emission starts. In figure 5.5 the difference between the onset, V_{oc}, and extinction voltages, V_{ox} is clearly distinguishable.

The observed decrease in current has been previously documented (Gamero-Castaño and Fernández de la Mora 2000, Jhuree *et al.* 2007) and we have characterized its energy distribution in later experiments with second generation devices. The most likely explanation is that the emitted particles are initially ionic and once the voltage is increased large solvated ions and droplets start to be emitted. As it is also likely that this transformation is linked to the formation of a jet at the apex of the liquid charge transport time becomes critical and causes a limitation of the current.
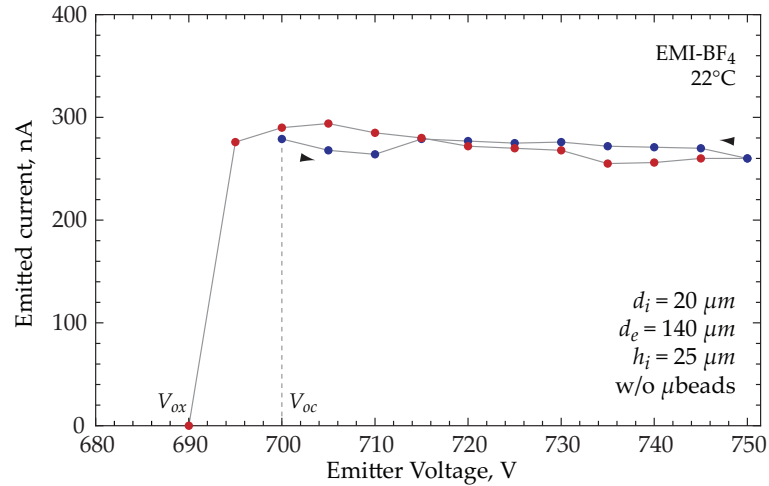
Figure 5.6: Current-voltage curve of a capillary emitter with 20 μm i.d. and a 140 μm diameter extractor electrode spaced 25 μm from the emitter. The sprayed liquid is EMI-BF$_4$ which is passively fed to the capillary (lines between data points only added for readability).

The observation of jumps in the current-voltage plot of a double capillary emitter with different extractor electrode diameters has served as inspiration to develop the onset voltage model presented previously in chapter 3. The trace shown in figure 5.7 was recorded with a chip having two 20 μm i.d. capillaries and an electrode spaced at 40 μm from the capillary tip. The difference in onset voltage is caused by two different extractor electrode diameters, one at 115 μm and one at 140 μm.

Onset voltage data obtained with first generation devices has been compared to values computed with the method presented in chapter 3 and to the analytical model assuming a hyperboloidal tip emitter. The results are summarized in table 5.2 and show very good agreement between the onset voltage model and the experimental data.

5.3 Single capillaries

The characterization of single capillaries has been the principal objective of the experimental phase. Only by understanding the operational characteristics and failure modes of these single emitter devices does upscaling to larger arrays become possible. In particular debugging failures and continuously improving device lifetime from a few seconds to several hours has been a great challenge. During the test campaign with second generation devices several interesting results were recorded and will be presented hereafter. Despite these advances a large domain of beam parameters are still unexplored and performance repeatability and thruster reliability remain an issue. In this section current-voltage curves and beam energy measurements are presented.
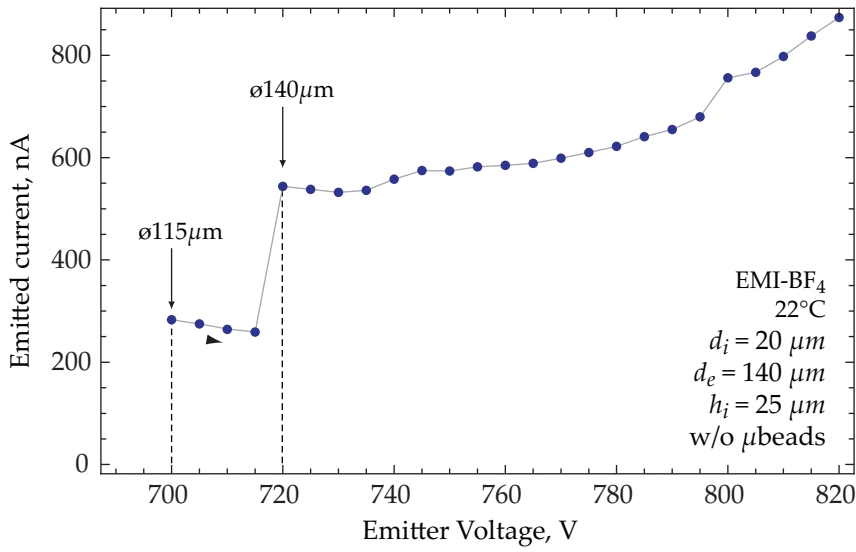
Figure 5.7: Current-voltage curve of two capillary emitters with 20 μm i.d. spaced at 40 μm from the emitter with an extraction hole diameter of 115 μm and 140 μm. The jump in current at 700 and 720 V can be attributed to different onset voltages. The sprayed liquid is EMI-BF$_4$ which is passively fed to the capillaries (lines added for readability).

Table 5.2: Comparison of the onset voltage between experimental, simulation and analytical results for our microfabricated ES arrays. The simulation results have been obtained with the method presented in chapter 3 of this paper, while the analytical ones using the hyperboloid surface algorithm.

Source-extractor distance[a](μm)	Extractor diam. (μm)	Onset Voltage (V)		
		Exp.[b]	Sim.[c]	Analyt.[d]
5	90	550-570	530	171
25	140	670-690	700	472
40	120	700	720	582
40	140	700-720	755	582

[a] Capillary height 70 μm, capillary diameter 20 μm.
[b] Range of experimentally measured onset voltages at room temperature with EMI-BF$_4$.
[c] Simulations using the model described in chapter 3. A surface tension of 0.045 N/m was used for the simulation.
[d] Analytical model assuming hyperboloid emitter surface, from ref. Martínez-Sánchez (2004).

The first part compares results obtained with capillaries filled with microbeads and capillaries without (Sec. 5.3.1). Allowing to draw a first conclusion on the effect of flow impedance on the beam composition. The second part then focuses on different beam behaviors observable with capillaries filled with microbeads (Sec. 5.3.2) and their energy distribution at different emitter voltages (Sec. 5.3.3). The section concludes with the results of a life test and discusses device degradation and failure modes (Sec. 5.3.4). Operational issues (liquid priming, cleanliness, among others) are discussed later in section 5.5. The flow rate data of the results presented hereafter have not been omitted by negligence, but by the absence of calibrated data (especially for capillaries filled with microbeads). Reservoir pressure data has also been omitted in most cases as most test results were obtained after formation of bubbles in the feed system.

5.3.1 Comparing capillaries with and without microbeads

Current-voltage measurements for capillaries without and with microbeads have been compiled in figures 5.8 and 5.9. The first figure illustrates the results obtained with a capillary without beads, while the second was obtained from a capillary filled with 5 μm microbeads. While the current of the capillary without beads increases steadily with increasing voltage, the one with the beads crosses a maximum around 1050 V and decrease rapidly at voltages above, thus behaving similarly to the first generation devices. The error bars indicate the standard deviation of the current values at different voltage levels (during one measurement cycle). The capillary with microbeads starts to show current instabilities above 1200 V leading to a decrease in repeatability and accounting for the larger standard deviation.

The comparison of the beam energy distributions of both capillary types shows the difference in beam composition. The current vs. retarding voltage for the capillary without beads is shown in (fig. 5.10a). The solid lines represent the interpolating spline used to compute the energy density distribution (derivative of current vs. retarding potential) shown in figure 5.11a. The broad energy spread, with one large peak well below the emitter voltage of 1000 V should be noticed. Lozano (2006) suggests that large energy distributions indicate the presence of a jet at the apex of the liquid cone implying the presence of droplets and that the large energy distribution is due to a drop in voltage in the jet due to the limited charge relaxation speed. Indeed the analysis of the thruster after spraying clearly reveals droplet reflection by the retarding potential grid. Figure 5.12 illustrates the droplets observed on the top of the extractor electrode after spray testing. During this test the retarding potential analyzer, having a single retarding grid, was placed 10 mm away from the emitter to capture the entire beam current. The effect of the grids can be clearly seen in figure 5.12a. A detail of the shape and size of the liquid droplets on top of the extractor is shown in figure 5.12b. From their size and distribution the conclusion can be drawn that agglomeration of small droplets has occurred over time.

Figures 5.10b and 5.11b show the current vs. retarding voltage and density distribution for a capillary with microbeads. In this second case a much smaller energy
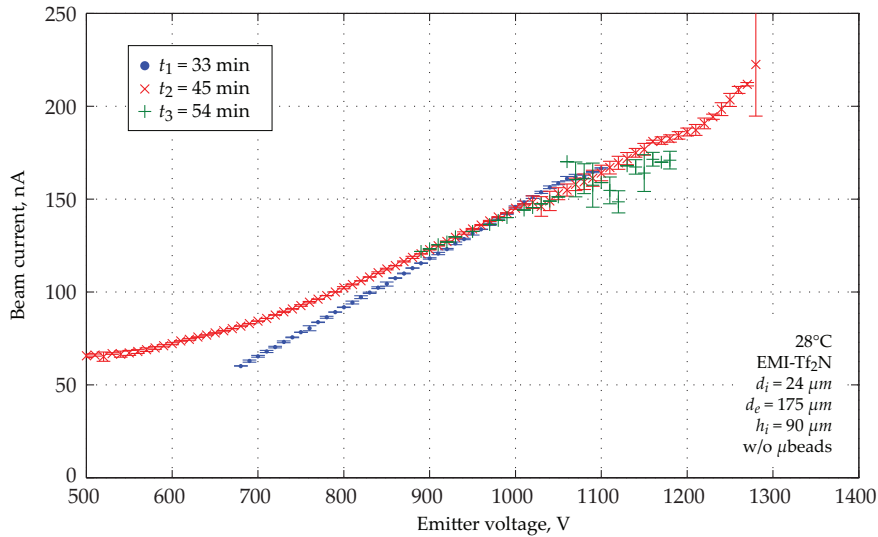
Figure 5.8: Current-voltage curve of a capillary emitter with 24 μm i.d. and a 175 μm extractor electrode spaced at 90 μm from the capillary tip *without* microbeads. The sprayed liquid is EMI-Tf$_2$N. The current-voltage characteristics were taken at three different times during the test. The thruster was operated in an unipolar regime. The error bars indicate the standard deviation at each voltage level for the three sequences.

distribution is observed and the main peak shows an energy deficit around 70 V. These measurements are comparable to similar ones done with externally wetted needles where purely ionic operation was seen (Lozano 2006). One effect of the potential 'sag' between retarding potential grid wires is the presence of particles seeming to have energies above the emitter voltage (900 V). The current obtained from this emitter is about half as much as the one from the capillary without beads.

For both capillaries the current tends to decrease over time while beam energy distribution stays identical. Multiple causes could be at the origin of this behavior. At spray start an initial "burn-in" time can be observed where the spray characteristics change over the first minutes. This fluctuations can be most likely linked to the fact that the tip surface is not immediately wetted. As the test duration increases a decrease in current can also be attributed to the contamination of the Faraday cup, particularly true for droplet mode where the grid wires block off parts of the beam and droplets agglomerate over time (fig. 5.13). As will be shown later in section 5.3.4 extractor electrode erosion might also contribute to this effect.

Another effect are electrochemical reactions leading to the buildup of a deposit on the electrode (in contact with the liquid) if the polarity is not switched regularly. Lozano and Martínez-Sánchez (2004) have previously observed this effect and reported a brownish coloration of their emitter needle. They suggest that an electrochemical process is at its origin. Due to the limited diffusion speed of ions toward the electrode they suggest the formation of a double layer at the electrode-liquid interface and model
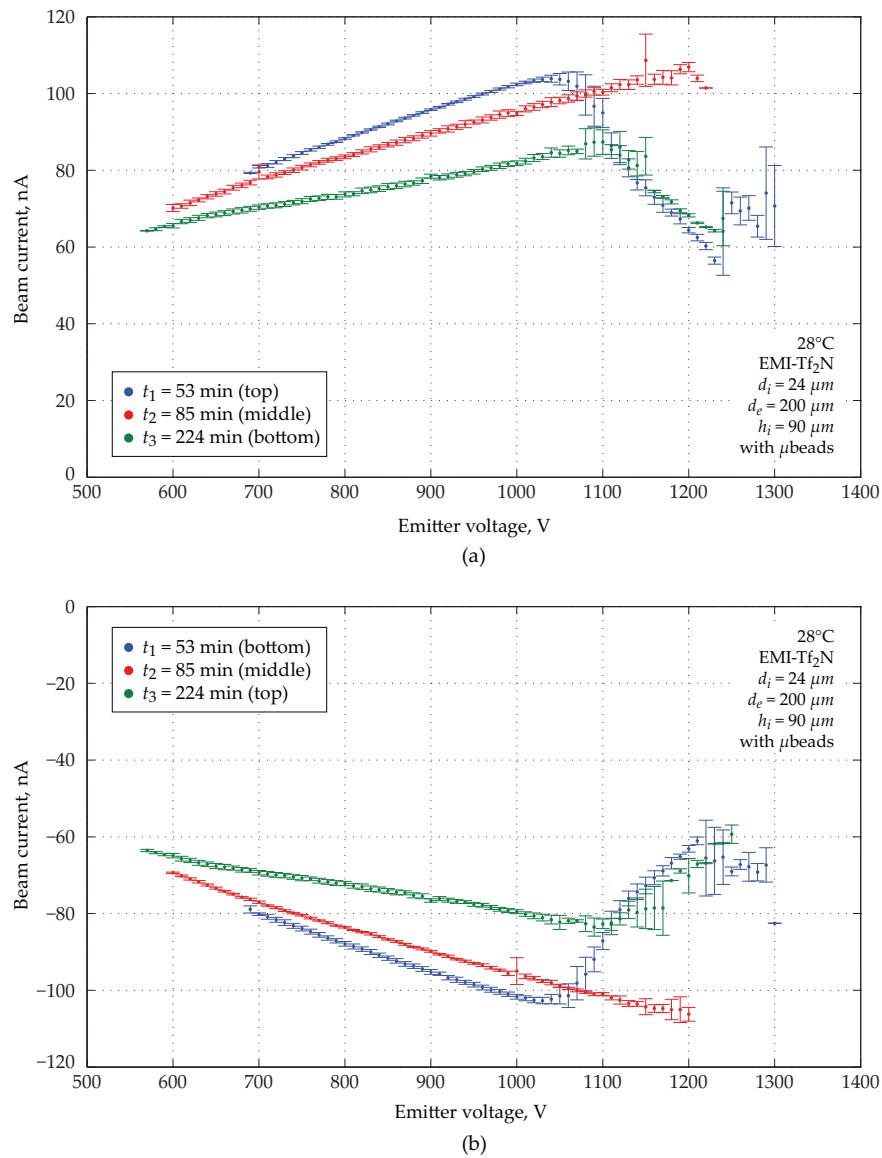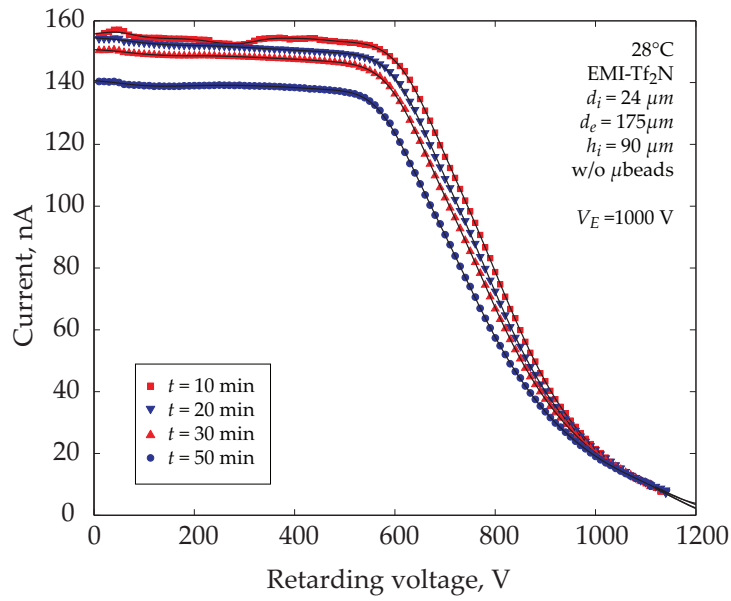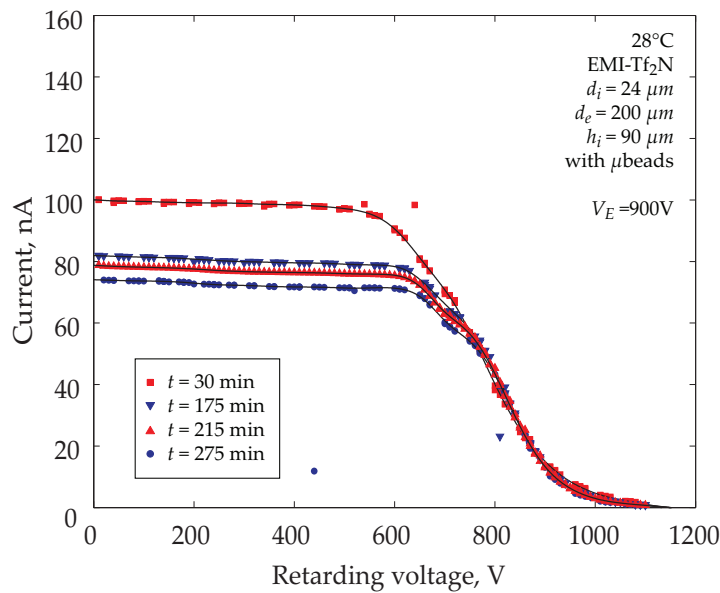
Figure 5.9: Current-voltage curve of a capillary emitter with 24 μm i.d. and a 200 μm extractor electrode spaced at 90 μm from the capillary tip filled with 5 μm microbeads. The sprayed liquid is EMI-Tf$_2$N. The current-voltage characteristics were taken at three different times during the test. The thruster was operated in a bipolar regime with a switching period of 4 seconds. The error bars indicate the standard deviation at each voltage level for the three sequences. The positive current is shown in (a) while the negative is shown in (b).
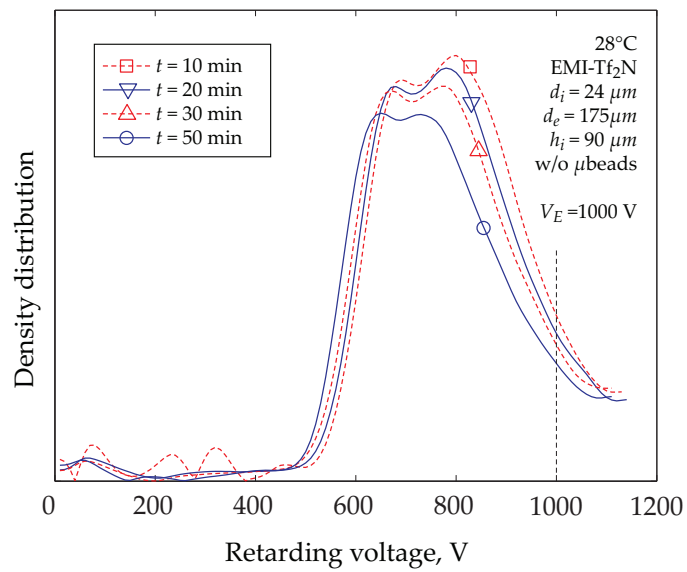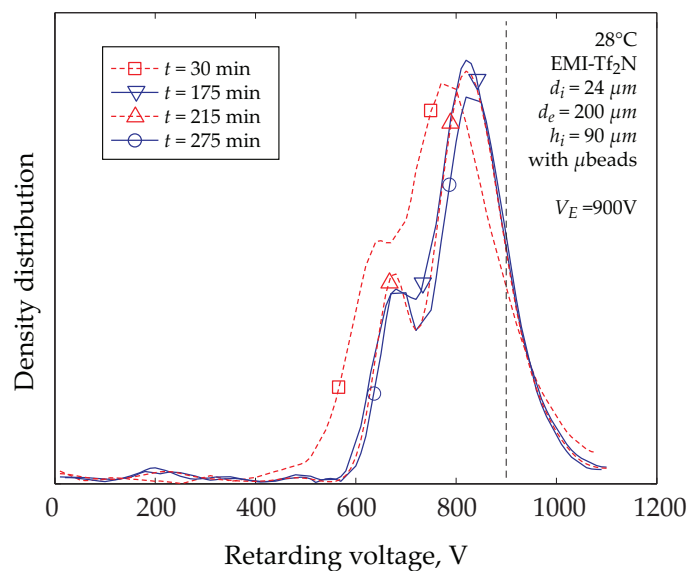
(a)

(b)

Figure 5.10: Comparison of the current vs. retarding voltage trace of a capillary without (a) and with (b) microbeads. The measurements were taken at different times during the test. The solid lines show the interpolating spline used to compute the density distribution function. The thruster configurations are identical to the ones in figs. 5.8 and 5.9.

(a)

(b)

Figure 5.11: Density distribution function for a capillary without (a) and with (b) microbeads. The measurements were taken at different times during the test. The thruster configurations are identical to the ones in figs. 5.8 and 5.9. The large energy deficit and broad peak in (a) indicate a jet at the apex of the liquid cone and the presence of droplets. The energy deficit in (b) is smaller and indicates operation in ionic regime. The markers are for annotation purposes only.
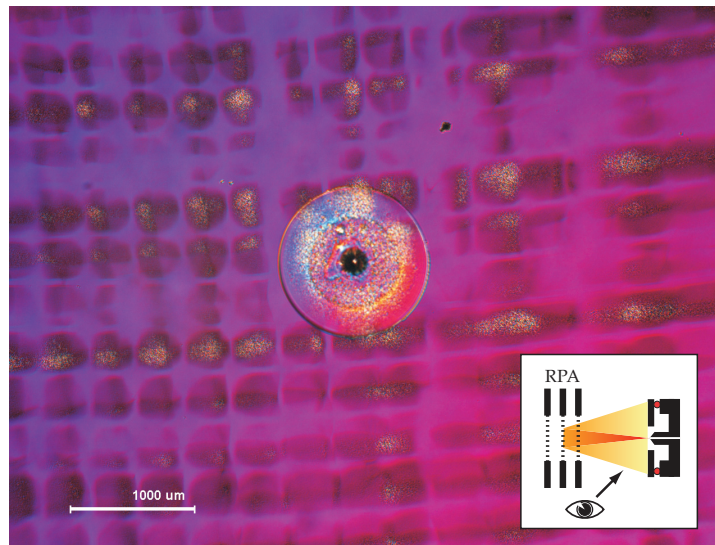
(a)
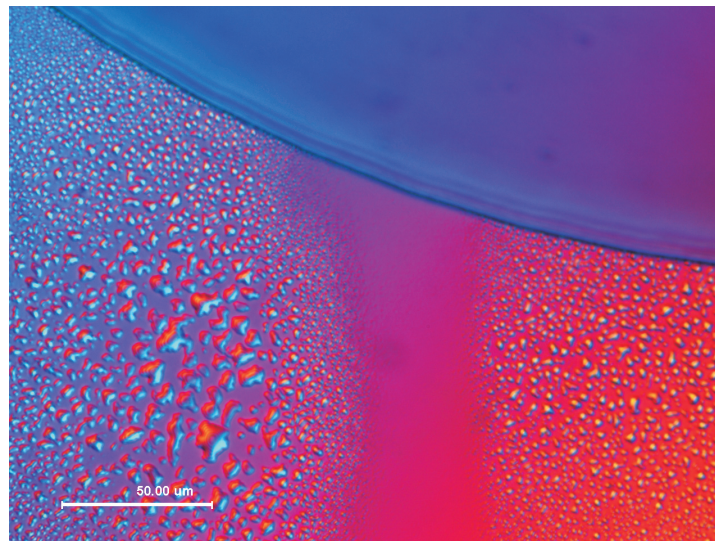
(b)

Figure 5.12: Droplets observed after spraying with a 24 μm i.d. capillary without microbeads and using a retarding potential grid to analyze beam characteristics. (a) shows the droplets which have been reflected. The shape of the grid is clearly visible, (b) detail of the deposited droplets. The shape of the droplets leads to the conclusion that multiple droplets have agglomerated over time. The truster configuration is identical to the ones described in figure 5.8.
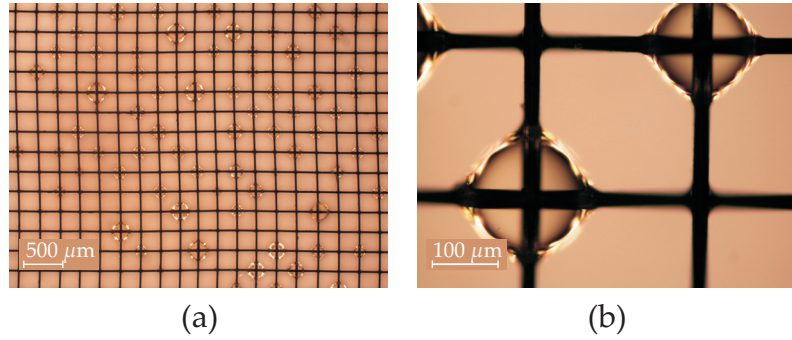
(a)   (b)

Figure 5.13: Photograph of the Faraday cup after spraying. Figure (a) shows an overview and (b) a detail of the grid. An agglomeration of droplets can be clearly seen at the wire cross section.

this double layer structure as a parallel plate capacitor. The critical time to raise the potential above the electrochemical window of the liquid (as high as 6 V for ionic liquids) is

$$t_w^{\pm} = \epsilon\epsilon_0 \frac{V_w^{\pm} A_e}{I\delta_{dl}}, \tag{5.5}$$

where I is the current, $V_w^{\pm}$ the electrochemical window limit, δ_{dl} the double layer thickness and A_e the electrode surface in contact with the liquid. For EMI-Tf$_2$N the thickness of the double layer is close to the anion diameter $\delta_{dl} \approx 4.58 \times 10^{-10}$ m, the dielectric constant $\epsilon = 12.2$ (Kobrak 2008) and the electrochemical window has a value of $V_w^+ = V_w^- \approx 2.25$ V. For the emitters without oxide the chip can serve as electrode and the computed time before electrochemical reactions set in is around $t_w^{\pm} \approx 16$ sec. For chips covered with oxide only the electrodes on the LTCC chip can be used and $t_w^{\pm}$ falls below 4 seconds. Of course the computed values with this simplistic model might be off by a factor of two. Ideally a safety margin larger than a factor of 10 would be chosen when selecting the switching speed but the data acquisition system and the switch limit the maximum speed at which switching can occur. For the bipolar tests a switching frequency between 1 Hz and 250 mHz was chosen with satisfactory results.

5.3.2   Spray modes

This section analyzes the various 'stable' modes that have been observed during spray testing, including pulsation, bistable and stable cone jet modes.

Bistable mode

While operating an EMI-Tf$_2$N spray and switching the polarity with a frequency of 250 mHz continuous jumps of the current were observed between two distinct levels. The capillary used in this experiment was filled with 5 μm beads and had a 200 μm diameter extractor spaced at 90 μm from the capillary tip. The operating voltage of

Table 5.3: Beam parameters extracted from bistable spray operation shown in figure 5.14. The configuration during this test was a 24 μm i.d. capillary with a 200 μm diameter extractor spaced at 90 μm from the capillary tip filled with 5 μm microbeads.

Peak no.	μ, nA	σ, nA	FWHM, nA
1	-58.4	1.69	3.99
2	-12.1	0.57	1.18
3	12.6	0.50	1.35
4	63.5	1.41	3.31

the emitter was 900 V. Figures 5.14a and 5.14b show the raw data acquired during the retarding potential measurement for two different timescales. The recorded current data points are marked as dots while the interpolating line is kept gray in figure 5.14b. The four current levels, two positive and two negative, can clearly be distinguished and appear as peaks in the histogram shown in figure 5.15. The two smaller current peaks (-12.1 and 12.6 nA) are practically symmetric around zero volts while the larger ones (-58.8 and 63.5 nA) are not. Table 5.3 summarisez these current values listing the median, the standard deviation and the FWHM for an approximated Gaussian distribution.

Figures 5.16a and 5.16b show the fitted retarding potential curve and the normalized density distribution of both modes. The 'high' current curve (mode 1) was acquired while increasing the retarding voltage while the 'low' current one (mode 2) during its decrease. No external action was taken to switch between these modes, as the emitter 'locked' into one or the other. The low current mode exhibits a much larger energy spread than the high current one. The energy distribution of the high current mode with a single peak and a rather small energy deficit could be the indicator of a "perfect cone", whereas the low current mode has a broad energy distribution which might indicate the presence of a jet at the liquid apex and could be the sign of droplet emission.

A more intriguing fact is the difference in current between the positive and negative beams, which would lead in the long term to charge build-up. A simple explanation would be given by a larger loss of particles of negative polarity in the retarding potential analyzer due to the suppression grid (biased at -50 V) or a larger beam angle (depositions on RPA elements have been observed).

Onset delays in bipolar operation

During the same test a mono-stable mode with turn-on delay when switching from one polarity to another has been observed. Switching delays have previously been observed and documented by Lozano and Martínez-Sánchez (2005*b*). Figure 5.17a shows a typical current trace for an emitter voltage of 1050 V where the switch delay is around 135 ms for the positive and 145 ms for the negative polarity. In
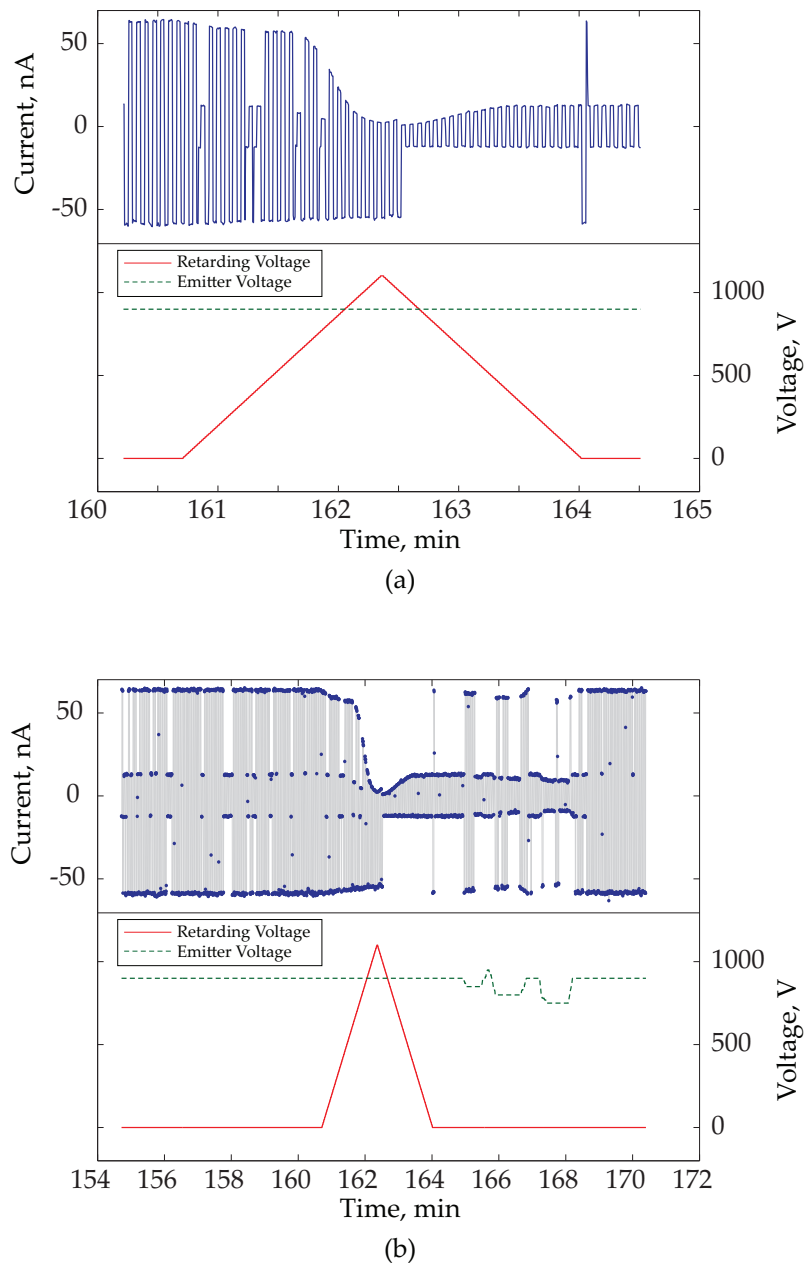
(a)

(b)

Figure 5.14: Bistable spray mode. (a) and (b) show the raw data taken during retarding potential measurement (two timescales). Signals in (a) have been interpolated, whereas in (b) the current sample points are marked with a dot (sample rate 0.333 Samples/s). Four stable current levels can be observed (two positive and two negative). The emitter during this test consisted of a 24 μm i.d. capillary filled with 5 μm microbeads having a 200 μm diameter extractor spaced at 90 μm from the capillary tip.
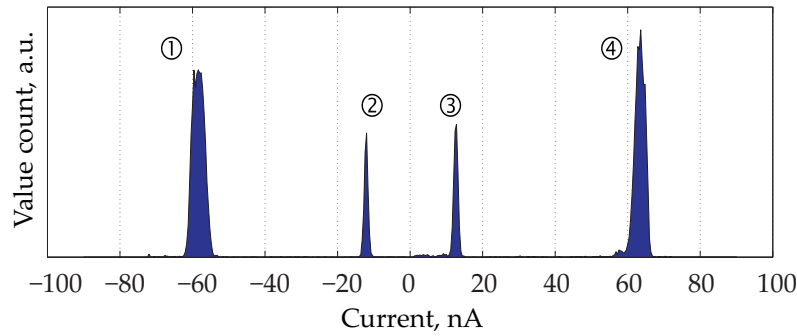
**Figure 5.15:** Histogram of the bistable spray mode. The plot shows the four distinct current peaks.

comparison figure 5.17b shows the behavior of the spray at 1200 V. Although a small overshoot is visible the switching delay has disappeared. The origin of the delay could be caused by the voltage which is too low to immediately deform the liquid into a cone thus letting a small droplet form at the tip of the capillary (due to the pressure difference between test chamber and the reservoir). Once a sufficiently large droplet has formed the electric stress sharpens the liquid into a cone. As this droplet contains a larger volume than the final cone a current overshoot is noticed. This hypothesis is strengthened by the observation of an even larger overshoot if the emitter voltage is turned off for a few seconds and then turned back on. In case of a spray without starting delay (as shown in figure 5.17b) the voltage is sufficiently high to immediately extract the liquid and for the spray to initiate.

Spray pulsation

Spray pulsations have also been observed, but not been investigated in detail as they are only of limited interest for propulsion purposes and are likely to damage the thruster. Pulsation modes have been mainly observed when 'starving' the liquid supply but also between two stable voltage levels. Figure 5.18a shows a current trace of a pulsating spray. In this case the duration between pulses is around 20 ms. A mix between stable mode and pulsations is shown in figure 5.18b. This trace taken at the end of life of a capillary is a likely indication of one stable and a secondary pulsating emission site.

5.3.3   Energy properties

The energy properties of an EMI-Tf$_2$N spray at different emitter voltages while switching the polarity with a frequency of 250 mHz was investigated. The capillary used in this test had an inner diameter of 24 μm and was filled with 5 μm beads and had a 200 μm diameter extractor electrode spaced at 90 μm from the capillary tip. The retarding potential was taken for various emitter voltages. Figure 5.19a shows the current vs. retarding voltage measurements. The solid lines represent the interpolating
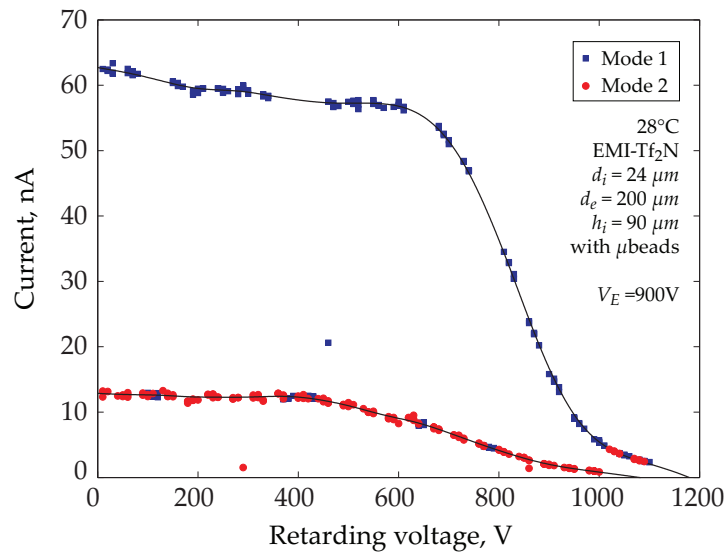
(a)
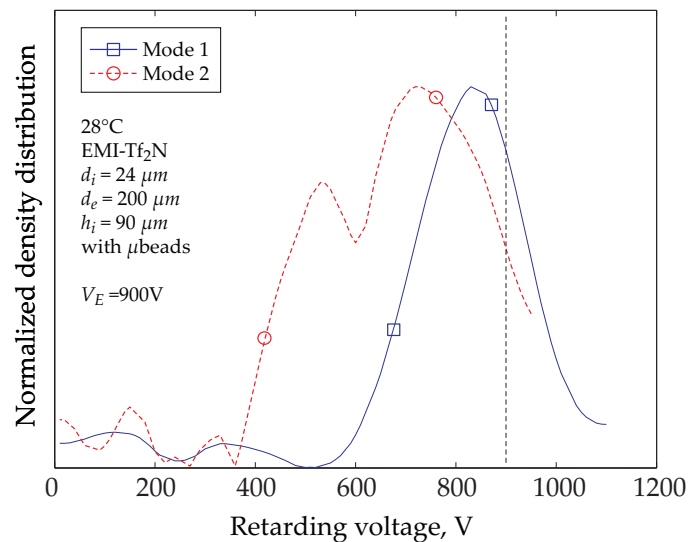
(b)

Figure 5.16: Bistable spray mode at 900 V emitter voltage. (a) and (b) plot the spray current as a function of the retarding voltage. The black lines are the fitted splines which have been used to compute the normalized density distribution. The configuration during this test was a 24 μm i.d. capillary with a 200 μm diameter extractor spaced at 90 μm from the capillary tip filled with 5 μm microbeads. In mode 1 the energy deficit is small indicating operation in the ionic regime while in mode 2 a broad distribution is observed indicating droplet operation. The squares and circles in (b) are for annotation purposes only.
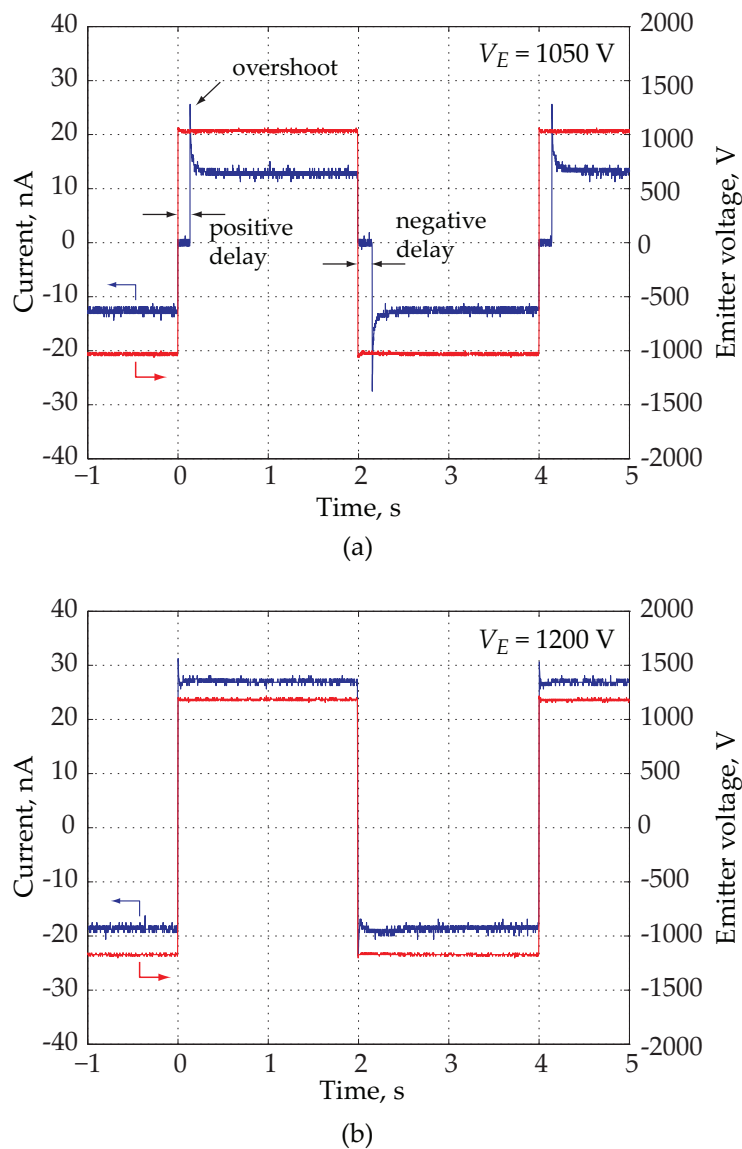
Figure 5.17: Current and voltage traces for EMI-Tf$_2$N sprays in the stable cone-jet mode (a) with switching delay (at 1050 V) and (b) without switching delay (at 1200 V). The emitter during this test was a 24 μm i.d. capillary filled with 5 μm microbeads having a 200 μm diameter extractor spaced at 90 μm from the capillary tip. The traces were taken after several hours of testing.
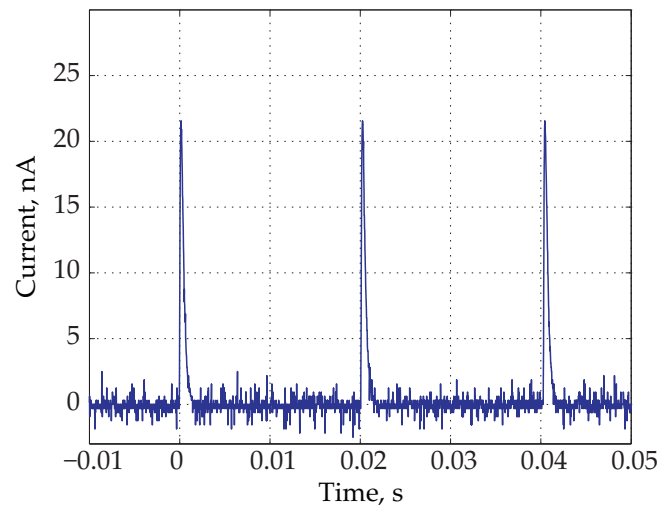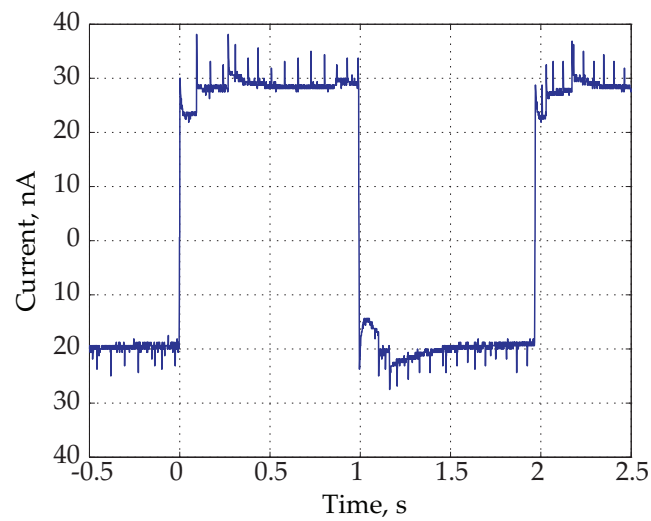
Figure 5.18: Traces of droplet modes at (a) low flow rates (at 1000 V) and (b) capillary end of life (at 1700 V), most likely indicating multiple emission sites.

spline used to derive the density distribution functions (shown in fig. 5.19b).

The change in beam energy distribution and current levels above a voltage of 1100 V is clearly visible. This broadening becomes clear in figure 5.20 where the density distributions are aligned by subtracting the emitter voltage from the retarding voltage ($V_{RP} - V_E$). At higher voltage measurements could not be taken anymore and beam instabilities set in. Lozano (2006) has observed a similar behavior of the beam with a coarse resolution RPA (single grid) spraying EMI-Tf$_2$N from a needle comparable to our measures for retarding voltages below 1200 V. His tests also show, when using a higher resolution RPA and performing time-of-flight analysis, that the beam is composed mainly of solvated ions (monomers, dimers and trimers).

The similarity between the results measured with the tungsten needles and the microfabricated emitters leads to the conclusion that the latter are most likely spraying in ionic mode. This hypothesis is further supported when comparing the energy distribution of the micromachined source (fig. 5.19) with mixed mode (droplets-ion) operation recorded by Gamero-Castaño (2008a) spraying EMI-Tf$_2$N from a silica capillary (fig. 2.9). In these sprays the larger 'ionic' peak is shifted well below the emitter voltage and a broad energy distribution at voltages *above* attributed to droplets can be observed.

The origin of the secondary peaks, marked in figure 5.20, still remains unclear as they are quite large for the microfabricated sources. In his higher resolution RPA experiments Lozano (2006) attributes them to the in-flight fragmentation of solvated ions. Although this might be an explanation for the presence of these peaks in the case of micromachined sources time-of-flight analysis would be needed to confirm the absence of droplets.

5.3.4   Life test

An extended life test was carried out spraying for over 60 hours. Figure 5.21 summarizes the whole current and control data acquired during the test. The test duration has been divided into six segments.

Section 1 - Startup and bistable mode: The spray was initiated by keeping a constant pressure on the feed system (single 1 m long silica capillary with 150 μm inner diameter) after spray startup bistable spray operation was observed. The pressure was then raised, by steps of approximately 10 mbar, but despite this increase the general tendency was a reduction of the current. Figure 5.22 shows the scatter plot of current vs. pressure (for a constant voltage of 900 V). The color gradient indicates the evolution in time going from dark shades to light ones. The solid lines have been introduced to show the trend of the current. When the pressure is constant the current gradually decreases, but when increasing quickly from one pressure level to the other the voltage increases.

Section 2 – Switch delay mode: During this part of the experiment the spray stabilized into switch delay mode as described in detail in section 5.3.2. The current readings have been plotted as a cloud of points in figure 5.23 as a function of time. The
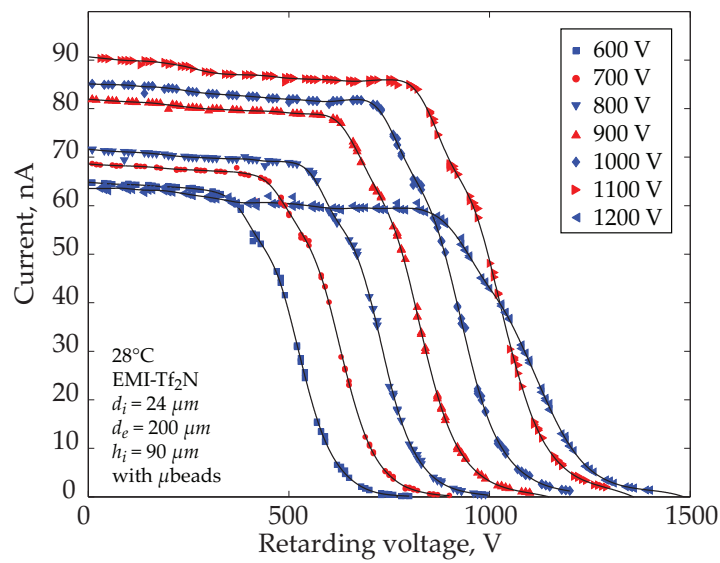
(a)
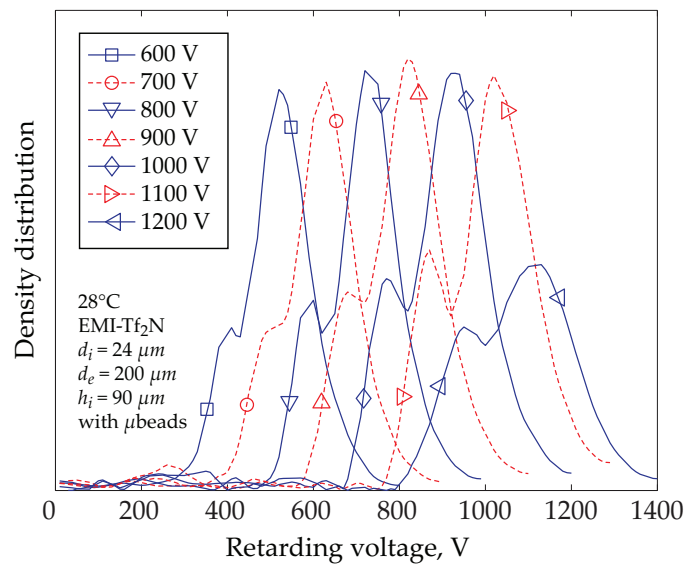
(b)

Figure 5.19: Retarding potential measurements for a 24 μm i.d. capillary with a 200 μm extraction electrode spaced at 90 μm from the capillary tip, filled with 5 μm microbeads and spraying EMI-Tf$_2$N. (a) shows the current vs. retarding voltage data where the lines are the interpolating splines for emitter voltages ranging from 600 to 1200 V. (b) shows the corresponding retarding potential distribution.
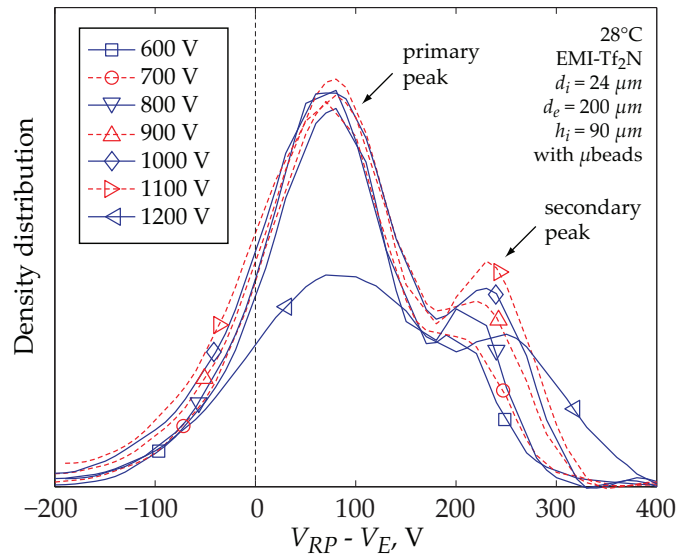
Figure 5.20: Retarding potential distribution measurements at constant flow rate for a 24 μm i.d. capillary with a 200 μm extraction electrode spaced at 90 μm from the capillary tip and filled with 5 μm microbeads spraying EMI-Tf$_2$N. The emitter voltage is subtracted from the retarding voltage to show the similarity of energy distributions for different emitter voltages. The change in beam properties for voltages above 1200 V is clearly visible.

initially small overshoot increases over time while the bulk current decreases. There were no external changes which could explain the sudden jump in current around 20 hours.

Section 3 – Stable mode: The microfabricated emitter was operated in a mode without switching delay during nine hours at a 0.5 Hz switching frequency (as illustrated in fig. 5.17b). This stable regime was reached by increasing the voltage to 1200 V. Retarding potential analysis and current voltage characteristics were recorded at the beginning, middle and end of this section. The results are shown in figures 5.24 and 5.25, they show barely any change in beam characteristics over time. Contrary to the test results shown in figure 5.9 instabilities in figure 5.25 set in around 950 V and it was not attempted to find a stable region below. On the other hand in figure 5.9 instabilities were observed for voltages above 1100 V, in this case voltages above were not investigated. Although a direct comparison between both emitters should be done with care, as a difference in hydraulic impedance and pumping conditions exist, both devices exhibit a minimum in current around 1050 V and show instability regions. Concluding different regions of stable operations might exist and future work should therefore focus on the determination of these stable regions and try to understand the change in behavior of the source between them.

Figure 5.26a plots the current points over the 9 hours of stable spray operation. The positive and negative peak are clearly visible. In figure 5.26b and 5.26c. The
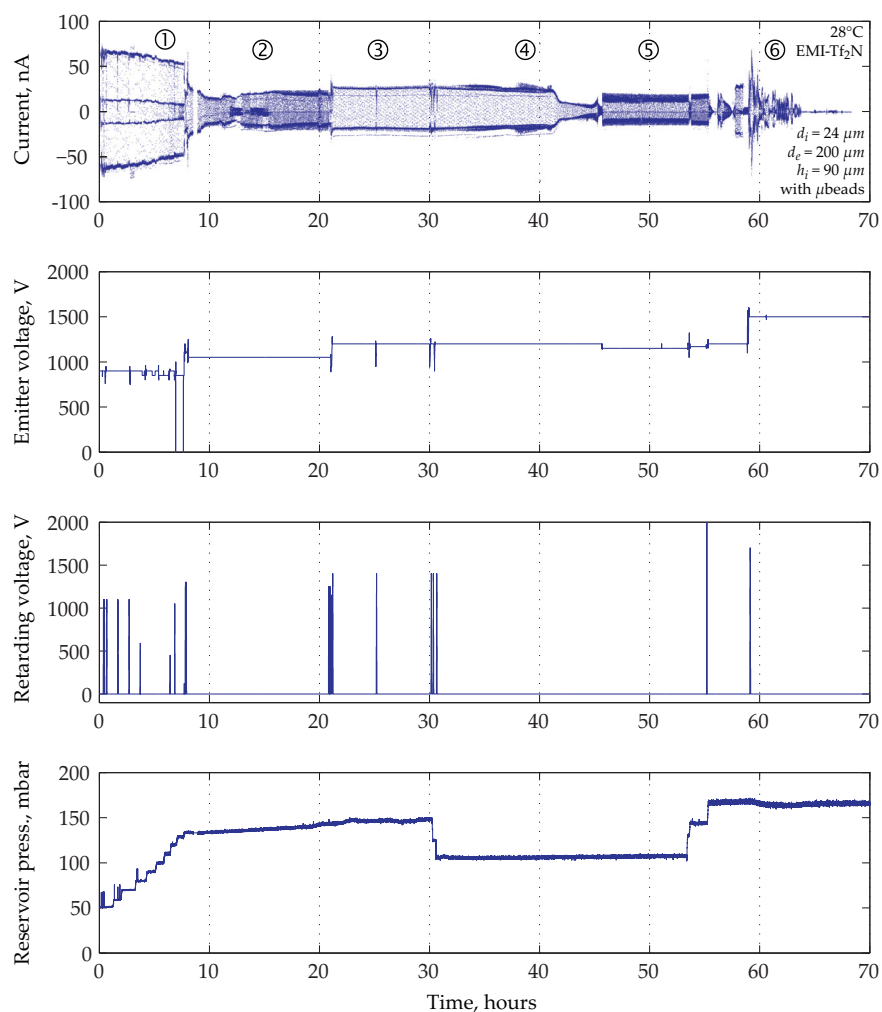
Figure 5.21: Plot of the spray current and test parameters during extended spray testing. The top trace shows the evolution of the current over the 64 hours of testing. Samples were acquired at sample rate of 300 ms. For this test a single emitter with a 24 μm i.d. capillary filled with 5 μm microbeads having a 200 μm diameter extractor electrode spaced at 90 μm from the capillary tip was used. The ionic liquid EMI-Tf$_2$N was used as fuel.
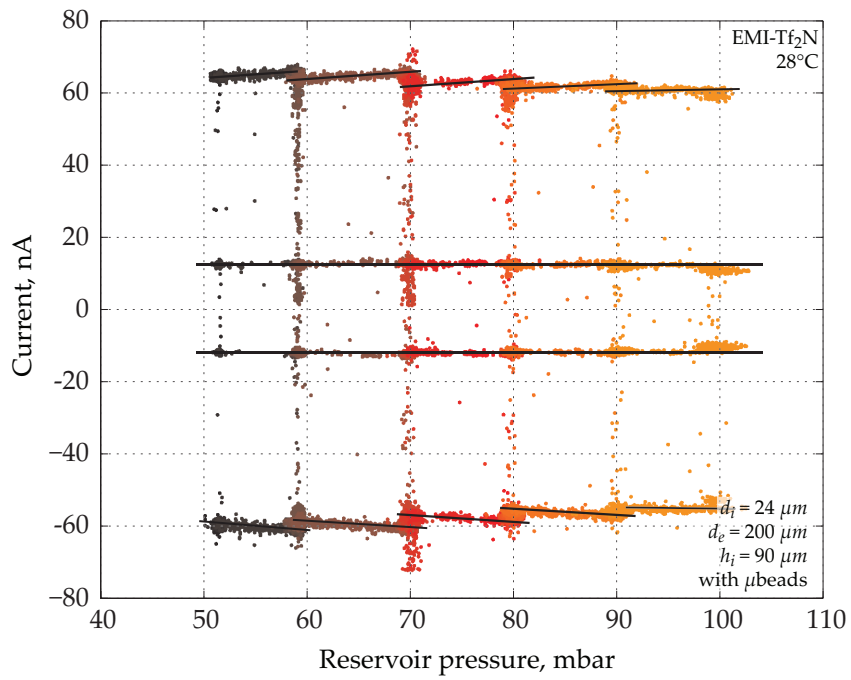
Figure 5.22: Scatter plot of current vs. pressure at the beginning of the life test. The points were acquired over approximately 5 hours. The color gradient indicates the time evolution and goes from dark to light shades. Thruster configuration is as in figure 5.21.
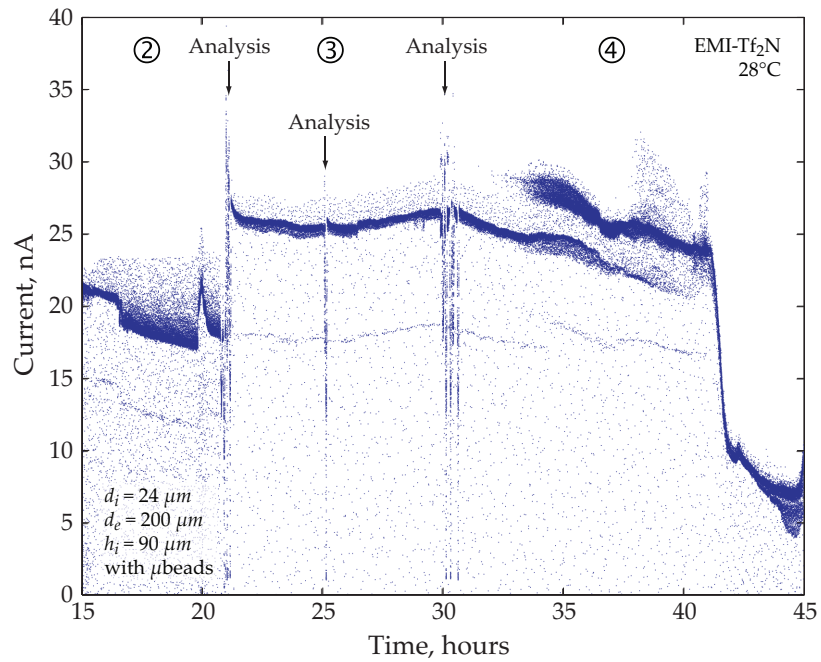
Figure 5.23: Detailed current plot recorded as a function of time for sections 2-4 of the life test. The spray operates mainly in mode 1 and only a few mode 2 points are visible. At each analysis point an RPA and voltage-current characteristic was recorded. Thruster configuration is as in figure 5.21.

detailed distributions of the positive current peak and negative one are shown.

Section 4 – Performance decay: At the start of this section the pressure was decreased from 150 mbar to 100 mbar. This leads to a steady decay in current and the appearance of a novel delay mode with large overshoot. Around 40 hours into the test a dramatic decrease in current occurs.

Section 5 and 6 – End of life: In this phase the recovery of the emitter was attempted but no more stable spray was achieved.

Several mechanisms can affect spray performance and thruster lifetime. Microscope and SEM photographs of the capillary emitter and extractor electrode after spray testing show degradations of the capillary and extractor electrode, and include

- degradation of the capillary;

- sputtering of the extractor electrode;

- liquid decomposition;

- microbead release;

- degradation of the electrode submerged in the liquid.

The photographs shown in figure 5.27 clearly shows sputtering of the electrode and capillary tip damage. It is likely that the latter has occurred at a single event such as the current spike at the end of section 5 (around 55 hours). Evidence for capillary damage during a single event is the large debris that can be seen at the far right of figure 5.27a. The smooth edges of the extractor electrode, on the other hand, lead to the conclusion that sputtering (or arcing) occurred continuously and has been a long term process. Electrode erosion could certainly account for the variations observed in sections 1-4 and would lead to the conclusion that erosion sets in immediately and a measurable drift should be observable after a few hours of spraying. The only stable mode where no decrease in current occurs is in section 3. The energy peaks measured in this section are right below the emitter voltage implying most likely ionic operation. From observations of the droplet depositions on both sides of the electrode and the evolution of the current, the conclusion can be drawn that the presence of droplets, being emitted continuously or due to a switching delay lead to a faster decrease of electrode lifetime. Electrode degradation could also be initiated by micro-beads leaving the capillary in the spray breaking off parts of the electrode or creating small craters in the extractor electrode (as can be observed in fig. 5.27b).

Liquid degradation has been observed as a change in color of an initially transparent liquid into a yellowish one. The reason for this decomposition is probably due to a small leakage current into the reservoir. This certainly leads to a change in viscosity and could also impact on spray current. Electrochemical decomposition is observed on the LTCC electrodes as a black deposit, but none on the silicon. Subsequent tests have shown blackening of the electrode in a matter of seconds by simply applying a single droplet of ionic liquid onto the electrode and biasing it to 20 V demonstrating the incompatibility of the silver/palladium electrode with the ionic liquid EMI-Tf$_2$N. Finally the glue used to bond the silicon chip to the LTCC (EPOTEK H70E) seems
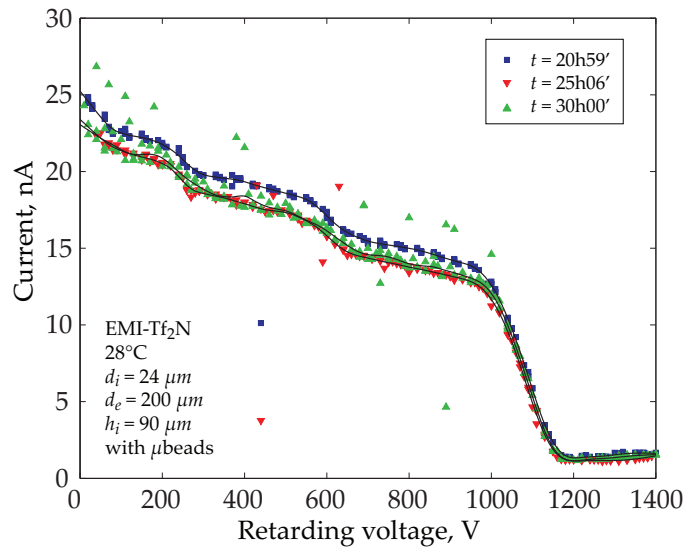
(a)
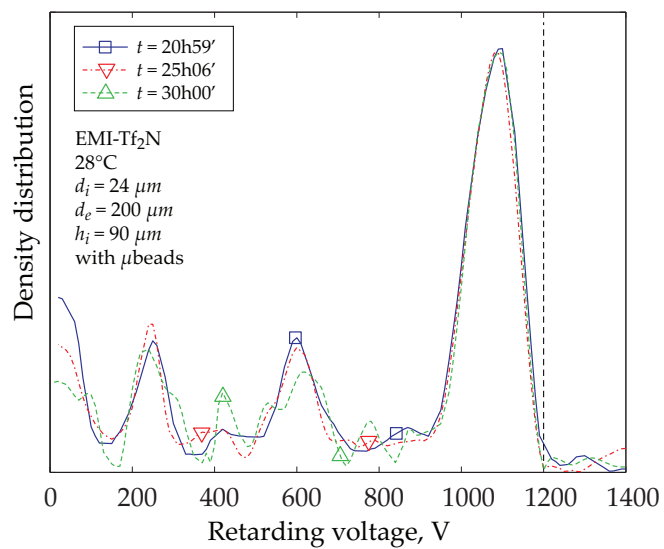
(b)

Figure 5.24: Retarding potential density distribution during section 3 of life test. (a) shows the current vs. retarding voltage data. The solid line represents the interpolating spline used to compute the density distribution in (b). Thruster configuration is as in figure 5.21 with an emitter voltage of 1200 V.
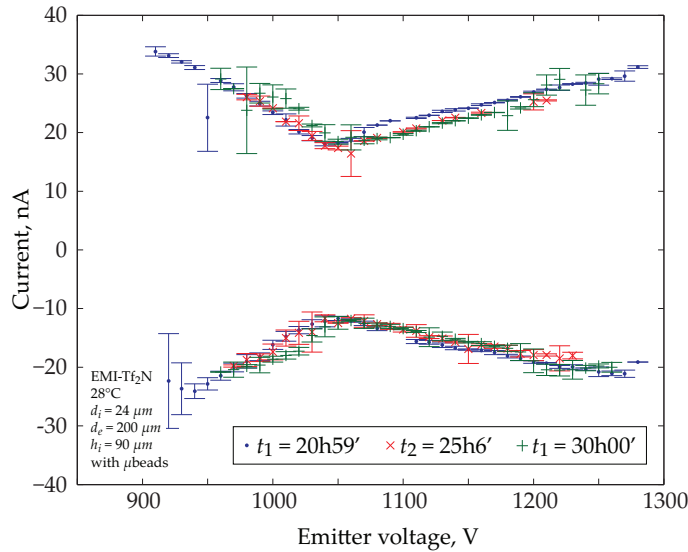
Figure 5.25: Current-voltage curve during section 3 of the life test. The data was acquired immediately after the retarding potential analysis shown in figure 5.24. Thruster configuration is as in figure 5.21.

not to be suited for long term exposure to EMI-Tf$_2$N as infiltration of liquid could be observed during post spray analysis.

5.4 Arrays of capillaries

Tests were also carried out with capillary arrays. Spray data was obtained at EPFL while time-of-flight traces were recorded at Queen Mary, University of London, in collaboration with Dr. K.L. Smith and Prof. J. P. W. Stark. Figure 5.28 shows the current trace for an array of 19 evenly spaced emitters. The pitch between the capillaries was 250 μm, the capillary were filled with 5 μm microbeads and had an inner diameter of 24 μm, the extractor electrode diameter was 200 μm with the electrode spaced at 90 μm from the capillary tip. Deposits on the upstream side of the suppression grid show that not all the current has been collected by the Faraday cup. Assuming a loss 25% of beam current for the 12 external capillaries results in a current per capillary of approximately 25 nA which is reasonably close to the spray current observed with single capillaries. Although the current is stable over short periods of times (fig. 5.29a) large fluctuations and current spikes (fig. 5.29b) can be observed, leading to the flooding of the chip.

The overall setup to perform time-of-flight is similar to the one at EPFL and is shown in figure 5.30. The drift length is $L_{TOF} = 410$ mm and interrupted by a potential barrier which is controlled using a high-speed switch pulse generator (DEI PVX-4110) with a rise/fall time < 60 ns.

The charge to mass ratio of a particle can be computed from its velocity and
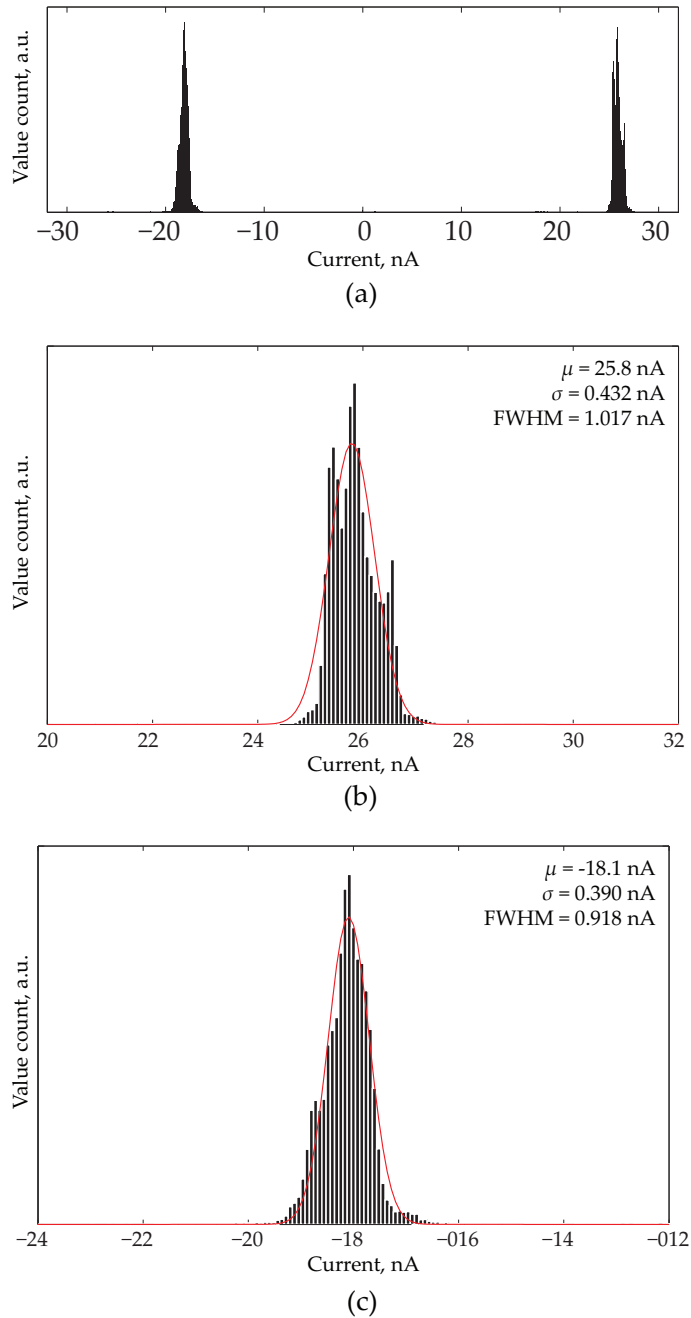
Figure 5.26: Histogram of the current value count during section 3 of the long term test. The two principal peaks at -25.8 nA and -18.1 nA are clearly visible in (a). The FWHM shows a maximum current fluctuation of less than 5% over the 9 hour test. (b) shows distribution details for the positive current peak and (c) details for the negative peak.

(a)   (b)

(c)   (d)
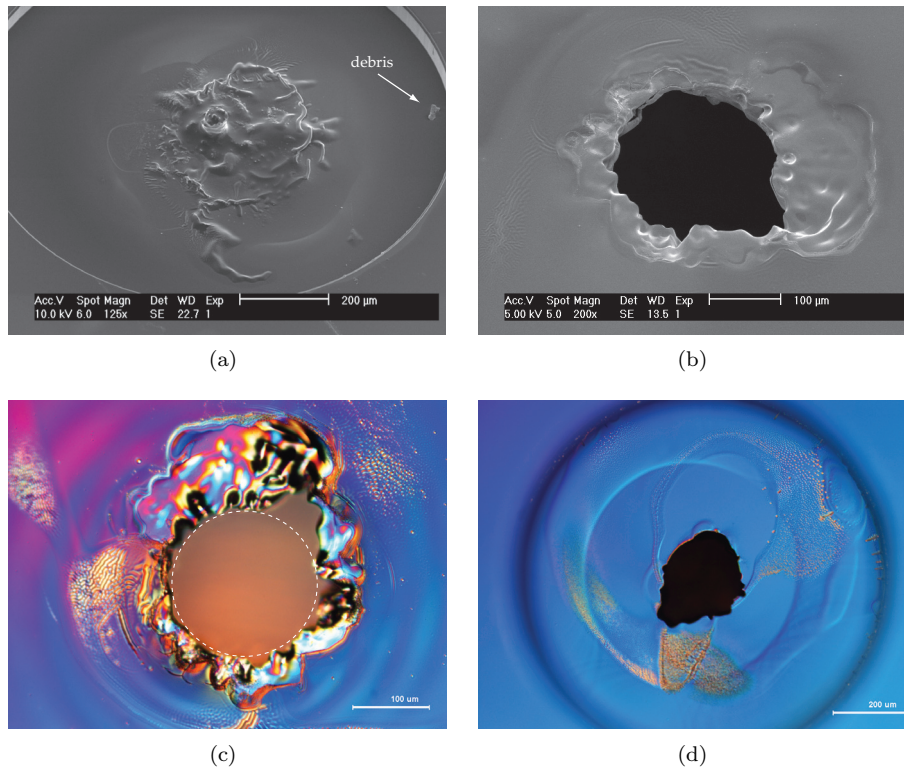
Figure 5.27: Images of the capillary and extractor electrode after a 64 hour test. A SEM photograph of the capillary (a) shows that parts of the tip were broken off, while (b) shows the complementary SEM photograph of the extractor electrode side facing the capillary. The original diameter was 200 μm. Light microscope images of the downstream (c) and upstream side (d) of the electrode show the sputtered electrode and liquid deposits due to the non-symmetry.
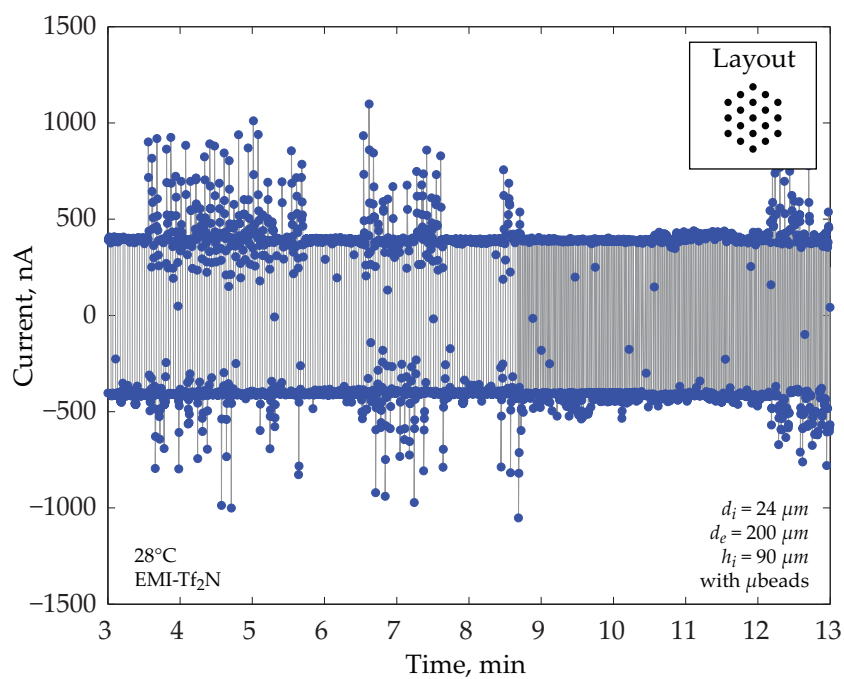
Figure 5.28: Current trace for a 19 capillary array. During this experiment the capillary configuration was 24 μm inner diameter, filled with 5 μm microbeads and with a 200 μm extractor electrode spaced at 90 μm from the capillary tip. The sprayed liquid was EMI-Tf$_2$N. The inital switch frequency was 0.25 Hz and was changed (at 8.5 min) to 0.5 Hz.
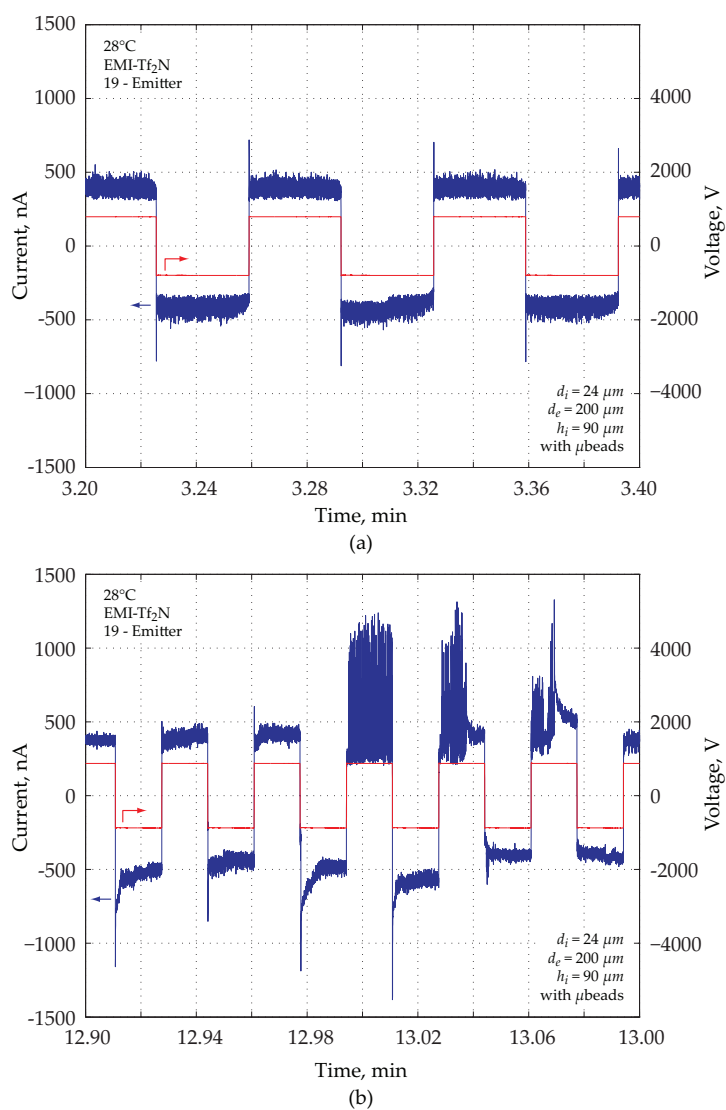
Figure 5.29: Current and voltage traces for EMI-Tf$_2$N sprayed from a 19 emitter array filled with 5 μm microbeads, 24 μm i.d. and a 200 μm extractor electrode diameter spaced at 90 μm from the capillary tip. Both measurements were taken at 1000 V, but while (a) shows stable operation, large current spikes can be seen in (b).
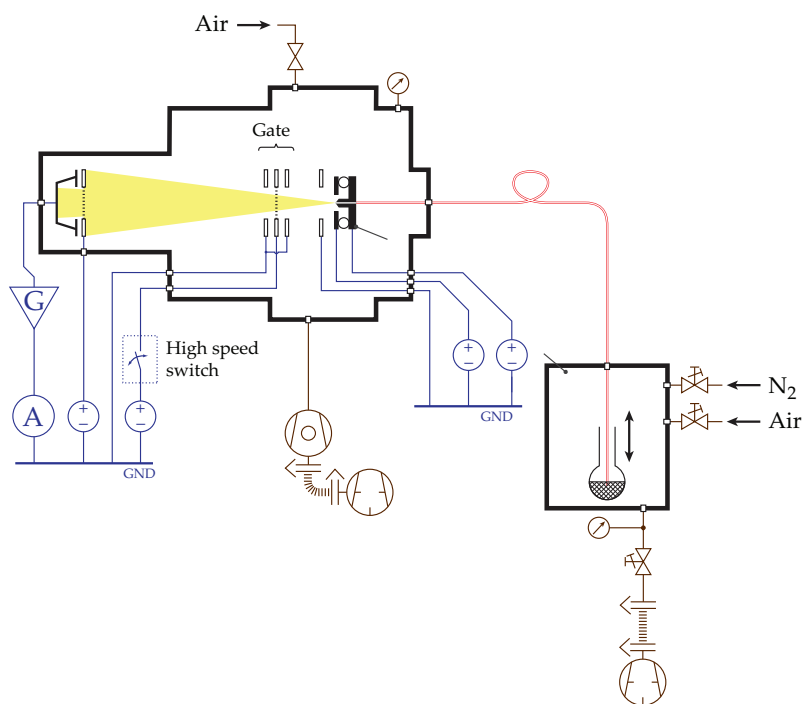
Figure 5.30: Time-of-flight measurement setup at Queen Mary, University of London. A high switch speed is used to commute a retarding potential barrier blocking the beam and thus allowing TOF traces to be recorded. The flight length is $L_{TOF} = 410$ mm.

beam potential

$$\frac{q}{m} = \frac{1}{2\Phi_B} \left(\frac{L_{TOF}}{t_{TOF}} \right)^2 , \tag{5.6}$$

where L_{TOF} is the flight distance, Φ_B is the beam potential and t_{TOF} is the drift time.

The TOF measurements were only carried out (due to time constraints) with arrays filled with 5 μm microbeads and traces were taken for various emitter voltages. Measurements are traced as current vs. time in figure 5.31a and as current vs. computed atomic mass in figure 5.31b. The masses of the EMI$^+$ monomer, and the (EMI-BF$_4$)EMI$^+$ dimer are indicated with dotted lines. To compute figure 5.31b the applied emitter voltage was used, assumed to be close to the beam voltage, and thus a shift to longer flight durations and higher atomic masses should be taken into account and explains also why the current decreases before reaching the theoretical drift time. For all voltages an ionic beam is observed with a decrease in dimer current as emitter voltage increases.

In the TOF traces of figure 5.31 no droplet current is observed. As multiple sources are emitting particles it is unlikely that all charged droplets are lost to the walls except if all the droplets are emitted off-axis which is unlikely. Density distribution and TOF measurements at increasing separation from the beam axis done by Gamero-Castaño (2008a) for capillary emitters show that in mixed mode droplets are present for all emission angles (fig. 2.9) further confirming the hypothesis of absence of droplets in our measurements.

The specific impulse and thrust can be computed from the time-of-flight traces (Guerreo *et al.* 2007)

$$T = \frac{2\Phi_B}{L_{TOF}} \int_0^\infty i(t) \, \mathrm{d}t \tag{5.7}$$

$$I_{sp} = \frac{L_{TOF}}{2 \, g_0} \frac{\int_0^\infty i(t) \mathrm{d}t}{\int_0^\infty i(t) \, t \, \mathrm{d}t} \tag{5.8}$$

where $i(t)$ is the current collected at the Faraday cup as function of time. The time $t = 0$ corresponds to the moment where the shutter cuts-off the beam. Table 5.4 compares the specific impulse and thrust computed from experimental results with the theoretical values for the EMI-BF$_4$ monomer and dimer. To remove the large current oscillations in of the TOF trace (recorded after switching the gate), the current traces were filtered using a second order Butterworth low pass filter. The thrust estimations are only given indicatively as a part of the current was lost to to the walls. Finally the beam voltage, Φ_B, was assumed to be identical to the emitter voltage, V_E.

Plot 5.32 is derived from table 5.4 and allows to draw the conclusion that the measured specific impulse lies between the theoretical value computed for a beam composed of solely monomers or dimers, giving good confidence that the required $I_{sp} > 8'000$ s (table 2.3) can be reached with an acceleration electrode biased at a voltage below 10 kV.
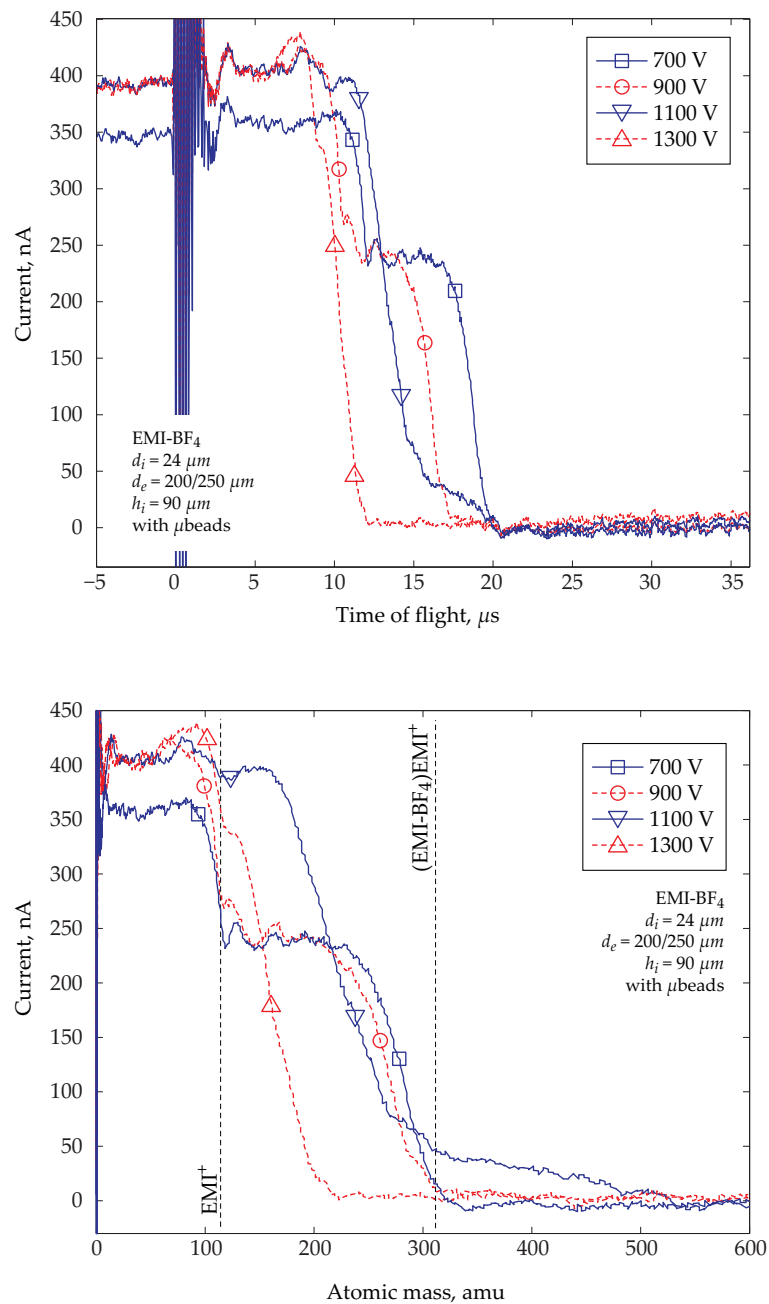
Figure 5.31: Time-of-flight traces recorded with a 19-emitter array with capillaries having a 24 μm inner diameter, filled with 5 μm microbeads with an extractor electrode with 200 μm holes spaced at 90 μm from the capillary tip. (a) shows the raw flight data for four different voltages, while (b) computes the corresponding atomic masses assuming the beam voltage to be equal to the emitter voltage. The equivalent flight times for the EMI$^+$ monomer and the (EMI-BF$_4$)EMI$^+$ dimers are marked as dotted lines.

Table 5.4: Specific impulse and thrust calculation obtained from the experimental TOF traces recorded with a 19-emitter array. The experimental data is compared to theoretical values for monomers and dimers of the ionic liquid EMI-BF$_4$.

V_E,[a] (V)	I_F,[b] (nA)	Specific impulse, I_{sp} (s)			Thrust, T (μN)		
		exp.[c]	monomer[d]	dimer[e]	exp.[c]	monomer[d]	dimer[e]
703	345	2363	3560	2133	0.021	0.014	0.023
803	352	2588	3805	2280	0.022	0.015	0.025
910	390	2765	4050	2428	0.026	0.018	0.030
1006	380	2795	4258	2552	0.027	0.018	0.031
1104	392	2819	4461	2674	0.031	0.020	0.033
1204	383	3674	4659	2792	0.026	0.020	0.034
1303	392	3727	4847	2905	0.028	0.021	0.036
1404	394	3709	5031	3015	0.031	0.022	0.037

[a] Emitter voltage
[b] Current measured at Faraday cup
[c] Value calculated from experimental data
[d] Theoretical value for EMI$^+$ monomer
[e] Theoretical value for (EMI-BF$_4$)EMI$^+$ dimer

Figure 5.32: Plot of the specific impulse and thrust calculation obtained from the experimental TOF traces recorded with a 19-emitter array. The experimental data is compared to theoretical values for monomers and dimers of the ionic liquid EMI-BF$_4$.

5.5   Operational issues

Early tests have shown that successfully spray testing requires the correct storage of the liquid. As consequence several measures were taken to decrease contamination.

5.5.1   Liquid priming

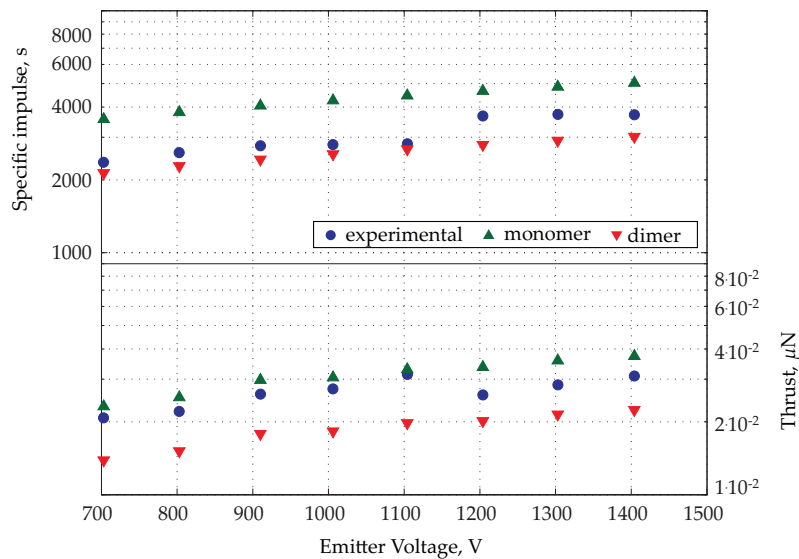During liquid priming the fluid is pumped from the reservoir through several capillary segments up to the emitter chip. The situation is illustrated in figure 5.33. The first segment links the liquid reservoir chamber, at pressure p_1, to the thruster characterization vacuum chamber held a low pressure, p_0. This first capillary has an outer diameter of 360 μm and an inner one of 150 μm (Upchurch, FS-115) and has a total length of 2 m. It is interconnected to a Teflon AF capillary through an Upchurch Microtight Union (P-720). Teflon AF has an exceptionally large permeability to gases such as CO_2, O_2, N_2 and H_2 and has a good resistance to solvents. Commonly used for degassing in column liquid chromatography a 35 cm long section has been inserted into the system to remove bubbles. Finally a third, 26 cm long capillary section (360 μm o.d., 150 μm i.d.) links the degassing segment to the LTCC chip support. The latter is interfaced through an Upchurch NanoPort interface (N-124S).

To estimate the time for the liquid to reach the capillary tip a fill model has been developed. As the diameter of the capillary segments varies a simple finite element model has been established (neglecting elasticity of tubes and fluidic connectors). The filling time of each element is (fig. 5.34)

$$\Delta t_j = \frac{\pi r_j^2 \Delta x_j}{Q_j} \tag{5.9}$$

$$x_j = \sum_{k=1}^{j} \Delta x_k \tag{5.10}$$

where Δt_j is the duration the liquid takes to fill segment, Δx_j the length of the segment, r_j the radius of the capillary and Q_j the volumetric flow rate at x_j. Q_j can be calculated assuming a Poiseuille flow

$$Q_j = \frac{\Delta P_j}{Z_j} \tag{5.11}$$

To compute the pressure difference we will assume a constant increase of the tubing height from the reservoir to the emitter capillary

$$\Delta P_j = p_{1,j} - p_0 - \frac{x_j}{\sum_{k=1}^{n} \Delta x_k} \rho g h. \tag{5.12}$$

The reservoir pressure $p_{1,j}$ can be controlled by the operator to increase or decrease filling speed, the characterization chamber pressure, p_0 stays constant. The last term represents the gravity effect on the liquid, where ρ is the density of the liquid, g the gravitational constant and h the height difference between the reservoir and the
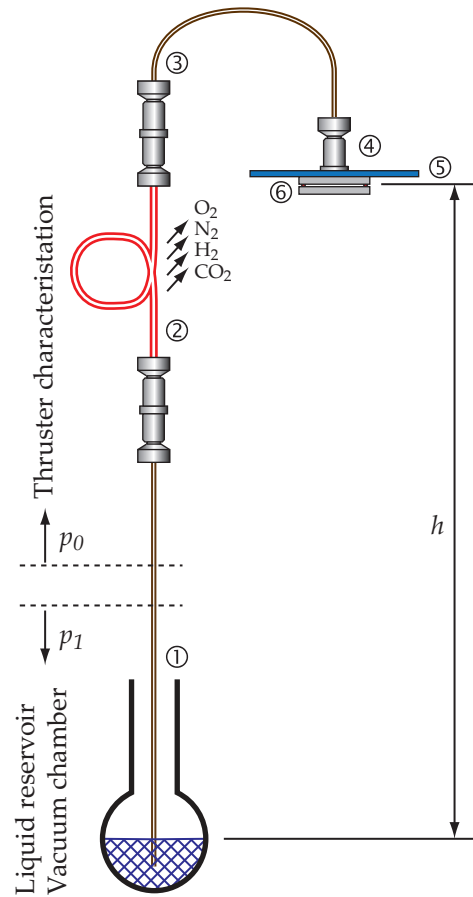
Figure 5.33: Liquid feed system. The emitter capillary is linked to the fluid reservoir through three capillary segments. Segments 1 and 3 are 150 μm i.d. silica capillaries. Segment 2 is a Teflon AF tube with 254 μm i.d. used as degassing segment to remove bubbles. The last segments 4-6 correspond to the volumes of the NanoPort adapter, the ceramic support and the emitter chip. The thruster characterization chamber is at low pressure, p_0, while the reservoir is at pressure p_1. The height difference between reservoir and the emitter is h.
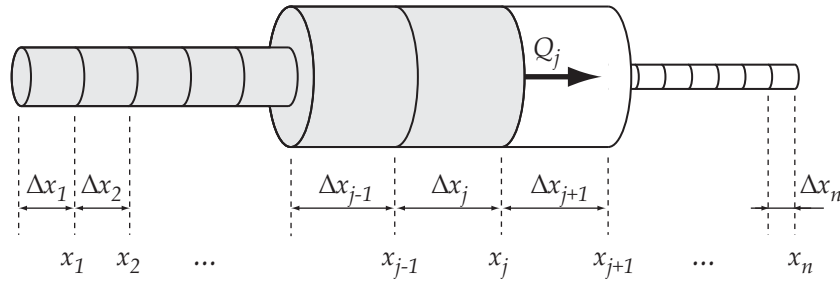
Figure 5.34: Schematic of the finite element model used to determine the flow rate and fill duration of the capillary. The model calculates the time Δt_j necessary to cross each element Δx_j.

emitter chip. The total fluid impedance in equation 5.11, Z_j, is the sum of the liquid impedance of the various elements

$$Z_j = \frac{8\mu}{\pi} \sum_{k=1}^{j} \frac{\Delta x_k}{r_k^4} \tag{5.13}$$

and the total flow time can therefore be expressed as

$$t = \sum_{j=1}^{n} \Delta t_j = \sum_{j=1}^{n} \left[\frac{8\mu r_j^2 \Delta x_j}{\Delta P_j} \sum_{k=1}^{j} \frac{\Delta x_k}{r_k^4} \right] \tag{5.14}$$

The large dispersion in dimensions across the fluid system requires particular care when first filling (priming) the system. If a high flow rate is chosen liquid overflow might occur once the capillary tip is reached while for a low flow rate the filling process will take too much time ($\gg$ day). In the ideal case the pressure difference across the capillaries interface is below the capillary pressure and the liquid stops when reaching the tip. For a fluid-"air"interface this capillary pressure can be calculated using the Young-Laplace equation

$$\Delta p = \frac{2\gamma}{r_t} \geq \Delta P. \tag{5.15}$$

Based on the finite element model the "fill strategy" summarized in table 5.5 has been defined. It is assumed that the pressure effect due to the height difference between the liquid and the reservoir increases steadily, which is not the case in reality.

In this long flow path setup the drops in flow rate induced by the operator by lowering the pressure of the liquid reservoir during tests have regularly caused the liquid to breakup inside the tubing. Therefore an alternative vacuum chamber setup was built for the liquid reservoir with a short 1 m single capillary. Although in this configuration no AF tubing is introduced for liquid outgassing no disturbing joints are present and bubbles can be avoided by careful insertion of the capillary into the ionic liquid.
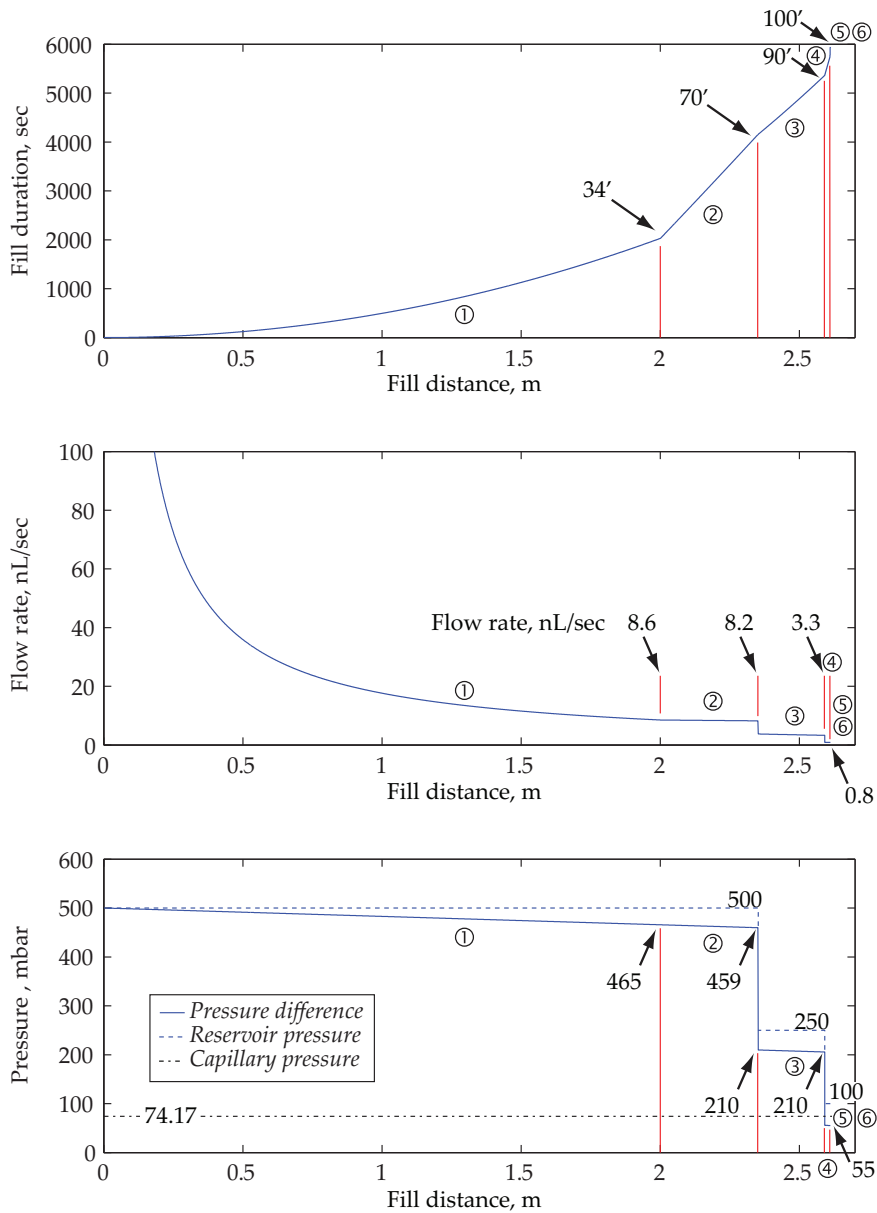
Figure 5.35: The three graphs show the computed filling time, flow rates and pressure difference using the flow model developed in this chapter for a 24 μm i.d. capillary. The results have been obtained using the fill procedure detailed in table 5.5. The jumps in flow rate are due to a change in reservoir pressure. It is assumed that the capillary mounts steadily from the reservoir to the emitter (which is not the case in the actual test setup).

Table 5.5: Filling procedure defined for a feed system with Teflon AF tubing. The reservoir pressure is gradually decreased as the liquid approaches the capillary.

No.	Pressure p_1 mbar	i.d. μm	Length mm	Comment
1	500	150	2000	Silica capillary
2	500	254	350	Degassing (Teflon AF)
3	250	150	240	Silica capillary
4	100	150	20	NanoPort interface
5	100	500	1	LTCC and Chip reservoir
6	100	24	0.1	Capillary emitter
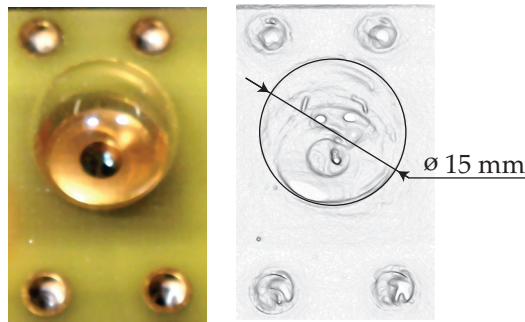
Figure 5.36: Bubble formation on the reservoir of an assembled thruster when no precautions are taken. The picture shows an expanding bubble during outgassing.

5.5.2 Cleanliness

Initially the fluid handling system was not available and filling of the ionic liquid occurred directly onto the assembled chips. As ionic liquids such as EMI-BF$_4$ or EMI-Tf$_2$N tend to absorb water from the air causing bubble formation during degassing special precautions need to be taken. These bubbles, such as the one illustrated in figure 5.36, can cause various problems. They can create a short between extractor electrodes or block-off a capillary emitter. As research progressed several improvements were made to the test setup and stringent cleanliness requirements introduced in order to avoid contamination of the fuel and failure of the thrusters. The test preparation procedure described hereafter has been adopted.

The feed capillary is first lifted out of the reservoir. The test chamber and reservoir are opened and the capillary tubing is rinsed with ethanol, as suggested by Anderson *et al.* (2006). The capillaries are then flushed for several minutes with dry nitrogen. The vacuum chambers are closed (without the thrust head) and pumped down. This step serves to degas the ionic liquid in case of any contamination and dry out any remaining solvent in the feed capillary. The reservoir is then filled to ambient

<div align="center">(a)   (b)</div>
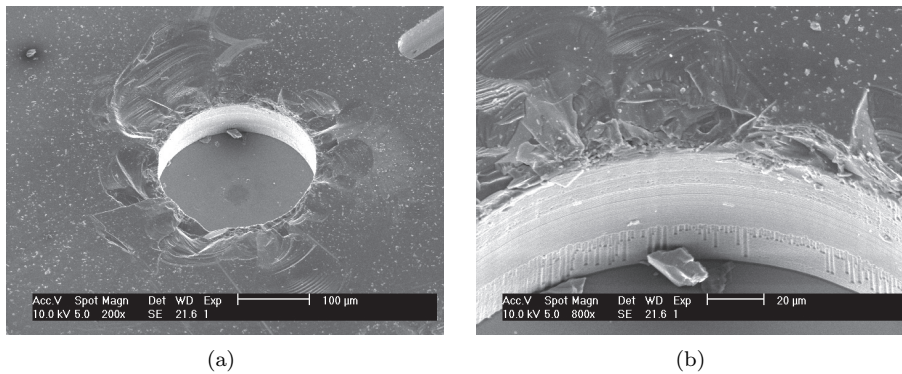
Figure 5.37: SEM photographs of one thruster failure mode. (a,b) grooves for the ruby balls on the capillary chip. Edge chipping and silicon splinters can clearly be seen.

pressure with dry nitrogen and the system is flushed for about 6 hours[1]. Finally the whole system is pumped down again for 15 hours. The attainable base pressures (without bakeout) are below 5×10^{-3} mbar for the reservoir and 3×10^{-7} mbar for the characterization chamber. With the fluidic components completely dry the thrust head is inserted and the feed capillary connected. To start a test, the vacuum chamber containing the ionic liquid is pressurized and the feed capillary lowered into the reservoir using the linear feed-through.

5.5.3   Other issues

Electrochemical decomposition of the EMI-BF$_4$ has been observed during testing. Decomposition can occur when a liquid spill shorts the capillary with the extractor electrode, resulting in total loss of the thruster. A second case observed by Lozano and Martínez-Sánchez (2005b) for needle emitters operating in ionic mode consists in the accumulation of the ionic species not being sprayed at the tip of the emitter and reacting with the needle material. The latter can be solved by alternating the emitters polarity, whereas spill can be controlled by increasing the fluid impedance of the source. For EMI-Tf$_2$N the situation is similar, as already discussed it tends to react quickly with the AgPd electrode on the LTCC. To minimize or avoid these issues bipolar operation using the high voltage switch has been added.

Chipping of the the ruby ball insulator grooves has been observed creating small silicon splinters that can create a short between emitter and the extractor electrode (figs. 5.37a and 5.37b). As the grooves are slightly undersized chipping occurs due to excessive pressure on the ruby balls. By introducing the PEEK support these defects have practically been eliminated.

---

[1]An increase of the pressure in the characterization chamber is observed indicating no obstruction of the capillary system.

5.6 Conclusion and Discussion

In this chapter spray results obtained with microfabricated capillary electrospray emitters have been presented. Sprays have been characterized for single capillaries filled with microbeads and capillaries without them. Spray results and time-of-flight data has also been recorded with 19-emitter arrays. Tests with single capillaries show that, as the voltage is increased, the spray current reaches a maximum to decrease sharply for voltages above. Energy density distributions recorded at different voltage levels show similar energy distributions up to the maximum current and a broadening of the beam energy distribution for voltages above. These retarding potential measurements of single emitters spraying the ionic liquid EMI-Tf$_2$N at different voltages (below the current maximum) show well defined energy peaks at a retarding voltage 70 V below the emitter voltage. It is generally assumed that a broad energy spread indicates the presence of a jet and thus the likely explanation of this behavior is that the beam rapidly changes above the maximum current from ionic to mixed mode. If the limited resolution of the RPA is taken into account an energy distribution and deficit similar to the one observed by Lozano (2006) in his experiments can be expected. The current behavior below the current maximum is linear. Above the current becomes instable, thus higher voltages were not tested to avoid emitter damage. Nevertheless high specific impulse can be reached by adding an additional acceleration electrode, while keeping the extractor electrode voltage in a region of stable spray regime. Assuming an ionic beam, the conclusion can be drawn that a scaling law for the current is more likely to be a behavior described by a charge separation equation, like equation 2.49, than a $I \approx (KQ)^{1/2}$ law. But contrary to full charge separation this scaling law should account for the variation in the distribution of solvated ions and space charge might also need to be considered as has been done for liquid metal ion sources (Mair 1984).

Interestingly the onset voltage computed for the second generation thrusters[2] using the model developed in chapter 3 is 1130 V for a 175 μm, and 1160 V for a 200 μm extractor electrode opening. Contrary to these computed onset values a spray current is measured for capillaries with and without microbeads for voltages as low as 500 V. An important difference to the first generation devices used to validate the onset voltage model is the active pumping (forced flow) of the liquid into the capillaries in the second generation thrusters. Pumping the liquid leads to the formation of a droplet at the tip of the capillary causing a significant decrease in the extinction voltage and is a likely explanation for the observed large deviation between measured values and onset voltage model predictions. In the case of measurements done using a capillary without microbeads spraying occurred in droplet mode (fig. 5.8) and the polarity was kept constant. This operating regime allows for a long jet to form which considerably lowers the extinction voltage. On the other hand for capillaries with microbeads the hypothesis of a liquid droplet forming at the tip of the capillary for

---

[2] The tested second generation thrusters were composed of a single capillary with 32 μm o.d., 24 μm i.d. and had a capillary tip to extractor electrode spacing of 90 μm. These emitters were spraying EMI-Tf$_2$N in a forced flow mode.

voltages below onset is also confirmed. Measurements show a switching delay and current overshoot when the thruster is operated at a voltage of 1050 V, while at 1200 V switching occurs without any delay and no current overshoot can be observed (fig. 5.17).

A life test demonstrating over 60 hours of device operation has shown the importance of operating the thruster in a stable regime. This first long duration test has also permitted to identify failure modes such as extractor electrode sputtering and degradation of the submerged electrode biasing the ionic liquid. It is likely that the tendency to sputter the extractor electrode is caused by the sharp corners of the extractor electrode which once damaged lead to a change in beam axis and further damage (runaway process). To obtain rounded extractor electrode edges an alternative manufacturing process using photoresist reflow and pattern transfer through plasma etching, as is done for microlenses (Schilling *et al.* 2000), has been investigated but not been finished in time to be tested within this work.

Finally the time-of-flight results reported for the operation of emitter arrays show a beam composed mainly of monomers and dimers and a specific impulse larger than 3500 s has been computed. Such an ion source with the reported characteristics, allowing a high specific impulse at 'low' voltages, shows the potential of electrosprays as alternative low thrust propulsion systems and strongly encourages future research in the field.

Chapter 6

Conclusion

RESEARCH results on a novel miniature electrospray thruster have been reported in this thesis contributing to the field of electrospray propulsion. Its highlights include a novel process flow for the microfabrication of the thrusters (Chapter 4), a design tool to predict its onset voltage (Chapter 3) and experimental results (Chapter 5) reporting its performance values.

Fabrication

A microfabricated electrospray thruster has been developed and successfully tested. The microfabrication process yields arrays of capillary emitters in silicon and complementary extractor electrodes. The chosen design path allows to integrate microfabricated extractor electrodes providing an individual extractor opening for each capillary. Alignment of the extractor electrode has been achieved by including a matrix of grooves on the capillary and the extractor chip allowing to place 200 μm ruby balls into them and to passively align the chips. This simple assembly method allows fast thruster assembly and disassembly while providing an alignment accuracy better than 2 μm (at chip level). An alternative way to integrate the extractor electrodes at wafer level has also been investigated and presented. In this case a Borofloat wafer is added as insulator between the extractor electrode and the capillary emitter. To increase the flow resistance of the capillaries 5 μm silica beads are added and fixed trough silanization using $SiCl_4$. The developed LTCC package with integrated heaters has proven to be a reliable support but several design improvements are needed in the future.

Onset voltage modeling

A design tool to predict the onset voltage of electrospray thrusters with complex geometries has also been introduced. The model takes into account the geometrical parameters of the thruster and the surface tension of the sprayed liquid and allows to compute the onset voltage of small aspect-ratio structures as can be found with

microfabricated devices. Test results for passively fed devices show good agreement with experimental data.

Experimental results

Experimental data acquired with the microfabricated thruster has shown various electrospray operational regimes, ranging from stable cone-jet to pulsating modes. The energy density distribution of the thruster is comparable over a wide voltage range and shows a single prominent peak close to the emitter voltage. Time-of-flight data obtained with an array of 19 emitters shows the presence of mainly monomers and dimers in the beam The maximum calculated specific impulse is 3727 s. A first life test demonstrates that stable operation is possible for several hours if the thruster is operated in the correct regime and shows that electrode sputtering is a key issue.

6.1   Future research

Future research should focus on the control of the fluidic impedance of the thruster. Although the silica beads have provided good results for prototype testing their fixation inside the capillaries needs to be improved. An alternative solution is the growth of a metal foam inside the capillary. This foam could fulfill a double function by increasing the fluidic impedance of the capillaries on one hand and on the other providing a good electric contact.

The LTCC support needs to undergo a major revision, in particular the use of an alternative material for the electrode submerged in ionic liquid. The current silver/palladium electrode does not provide the necessary long term stability for constant thruster operation. When powered a black deposit forms after a couple of minutes. Further breakdown between the heaters and the HV supply lines has been observed and should be further investigated. In this case the distance between the high voltage conductors and heaters needs to be increased. In addition functionalities such as electrodes to measure fill status could be added and the emitter chip should be placed directly at a high potential. The long term material compatibility of all used materials should be tested, various materials have shown incompatibilities, these include certain stainless steels, epoxy and silicone glues.[1]

A better understanding should also be gained on the stability of the ionic liquids used as fuel. A yellowish coloration after testing is a clear sign of their degradation. Its origin is not clear, but most likely due to leakage currents into the reservoir. To avoid leakage currents a first measure would be to improve the electrical isolation of the elements in contact with the liquid (capillaries, reservoir, feed-throughs, among others). This investigation should be combined with a general review of the pumping system. Ideal would be to integrate the fluidic system into the principal vacuum chamber and to mechanically push the liquid into the feed system using a piston.

Further research is necessary to characterize the different operational modes of

---

[1]Incompatible glues are Dow Corning Q5-8401 and EPO-TEK H70E.

the capillaries. A test series should be devised to characterize several capillaries under the same conditions. As certain operating ranges lead to a faster degradation of the thruster a limited range of parameters should be explored in each test to avoid a drift in performance and to identify modes with low impact on thruster lifetime. To increase extractor lifetime, the individual hole diameters could be further increased (requiring a larger pitch size), alternative coating techniques investigated to decrease sputter rate or a microfabrication process developed where the edges of the extractor electrode are rounded.

In conclusion the thruster prototypes presented in this thesis have shown the feasibility of a small electrospray thrust system with high specific impulse. The stable beam characteristics over several hours show that if the thruster is operated under the right conditions stable operation can be achieved. The main objective of future work should be to increase reliability and lifetime, increasing the technology readiness level of the system and taking it from a laboratory prototype to a fully qualified thruster.

Bibliography

Abramowitz, M. and Stegun, I. A., eds (1964), *Handbook of Mathematical Functions with Formulas, Graphs, and Mathematical Tables*, Dover, New York.

Alexander, M. S., Paine, M. D. and Stark, J. P. W. (2006), Pulsation modes and the effect of applied voltage on current and flow rate in nanoelectrospray, *Analytical Chemistry* **78**, 2658–2664.

Anderson, R. J., Plett, G., Anderson, M. and Ziemer, J. (2006), Testing fundamental properties of ionic liquids for colloid microthruster applications, *in* Proc. 42nd AIAA/ASME/SAE/ASEE Joint Propulsion Conference and Exhibit, Sacramento, California, number AIAA 206-4646.

Bailey, A. G. (1973), Investigation of a single spraying site of a colloid thruster, *Journal of Physics D: Applied Physics* **6**(2), 276–288.

Bailey, A. G., Bracher, J. E. and von Rhoden, H. J. (1972), A capillary-fed annular colloid thruster, *in* Proc. 9th International Electric Propulsion Conference, Florence, Italy, number 490.

Boas, M. L. (2006), *Mathematical Methods in the Physical Sciences*, John Wiley & Sons, Inc.

Bonhôte, P., Dias, A.-P., Papageorgiou, N., Kalyanasundaram, K. and Grätzel, M. (1995), Hydrophobic, highly conductive ambient-temperature molten salts, *Inorganic Chemistry* **35**(5), 1168–1178.

Bronstein, I. N., Semendjajew, K. A., Musiol, G. and Mühlig, H. (2005), *Taschenbuch der Mathematik*, 6th edn, Verlag Harri Deutsch.

Castro, S., Larriba, C., De La Mora, J., Lozano, P., Sümer, S., Yoshida, Y. and Saito, G. (2007), Effect of liquid properties on electrosprays from externally wetted ionic liquid ion sources, *Journal of Applied Physics* **102**, 94310.

Chen, D.-R., Pui, D. Y. H. and Kaufman, S. L. (1995), Electrospraying of conducting liquids for monodisperse aerosol generation in the 4 nm to 1.8 μm diameter range, *Journal of Aerosol Science* **26**(6), 963–977.

Chiu, Y.-H., Austin, B., Dressler, R., Levandier, D., Murray, P., Lozano, P. and Martinez-Sánchez, M. (2005), Mass spectrometric analysis of colloid thruster ion emission from selected propellants, *Journal of Propulsion and Power* **21**(3), 416–423.

Cloupeau, M. and Prunet-Foch, B. (1990), Electrostatic spraying of liquids: Main functioning modes, *Journal of electrostatics* **25**(2), 165–184.

Corman, T., Enoksson, P. and Stemme, G. (1998), Deep wet etching of borosilicate glass using an anodically bonded silicon substrate as mask, *Journal of Micromechanics and Microengineering.* **8**(2), 84–87.

Demmons, N., Hruby, V., Spence, D., Roy, T., Ehrbar, E., Zwahlen, J., Martin, R., Ziemer, J. K. and Randolph, T. M. (2008), ST7-DRS mission colloid thruster development, *in* Proc. 44th AIAA/ASME/SAE/ASEE Joint Propulsion Converence and Exhibit, Hartford, Connecticut, number AIAA 2008-4823.

Driesel, W., Dietzsch, C. and Mühle, R. (1996*a*), In situ observation of the tip shape of AuGe liquid alloy ion sources using a high voltage transmission electron microscope, *Journal of Vacuum Science & Technology B: Microelectronics and Nanometer Structures* **14**(5), 3367–3380.

Driesel, W., Dietzsch, C. and Möser, M. (1996*b*), In situ HV TEM observation of the tip shape of lead liquid metal ion sources, *Journal of Physics. D, Applied Physics* **29**(9), 2492–2500.

Drozin, V. G. (1955), The electrical dispersion of liquids as aerosols, *Journal of Colloid Science* **10**(2), 158–164.

English, W. N. (1948), Corona from a water drop, *Physical Review* **74**(2), 179–189.

Enloe, C. L. and Shell, J. R. (1992), Optimizing the energy resolution of planar retarding potential analyzers, *Review of Scientific Instruments* **63**(2), 1788–1791.

Faux, I. D. and Pratt, M. J. (1979), *Computational geometry for design and manufacture*, Halsted Press (Wiley).

Fenn, J., Mann, M., Meng, C., Wong, S. and Whitehouse, C. (1989), Electrospray ionization for mass spectrometry of large biomolecules, *Science* **246**(4926), 64–71.

Fernández de la Mora, J. (2007), The fluid dynamics of Taylor cones, *Annual Review of Fluid Mechanics* **39**, 217–243.

Fernández de la Mora, J. and Loscertales, I. (1994), The current emitted by highly conducting Taylor cones, *Journal of Fluid Mechanics* **260**, 155–184.

Gañán Calvo, A., Dávila, J. and Barrero, A. (1997), Current and droplet size in the electrospraying of liquids, scaling laws, *Journal of Aerosol Science* **28**(2), 249–275.

Gañán Calvo, A. M. (1994), The size and charge of droplets in the electrospraying of polar liquids in cone-jet mode, and the minimum droplet size, *Journal of Aerosol Science* **25**(Suppl. 1), 309–310.

Gañán Calvo, A. M. (2004), On the general scaling theory for electrospraying, *Journal of Fluid Mechanics* **507**, 203–212a.

Gamero-Castaño, M. (2008*a*), Characterization of the electrosprays of 1-ethyl-3-methylimidazolium bis(trifluoromethylsulfonyl) imide in vacuum, *Physics of Fluids* **20**(3), 032103.

Gamero-Castaño, M. (2008*b*), The structure of electrospray beams in vacuum, *Journal of Fluid Mechanics* **604**, 339–368.

Gamero-Castaño, M. and Fernández de la Mora, J. (2000), Direct measurement of ion evaporation kinetics from electrified liquid surfaces, *Journal of Chemical Physics* **113**(2), 815–832.

Garoz, D., Bueno, C., Larriba, C., Castro, S., Romero-Sanz, I., De La Mora, J., Yoshida, Y. and Saito, G. (2007), Taylor cones of ionic liquids from capillary tubes as sources of pure ions: The role of surface tension and electrical conductivity, *Journal of Applied Physics* **102**, 064913.

Gassend, B. L. P. (2007), A Fully Microfabricated Two-Dimensional Electrospray Array with Applications to Space Propulsion, PhD thesis, Massachusetts Institute of Technology.

Gassend, B., Velásquez-García, L. F., Akinwande, A. I. and Martínez-Sánchez, M. (2008), Fabrication of a fully integrated electrospray array with applications to space propulsion, *in* Proc. 21st IEEE International Conference on Micro Electro Mechanical Systems, Tucson, Arizona, IEEE, pp. 976–979.

Gongora-Rubio, M. R., Espinoza-Vallejos, P., Sola-Laguna, L. and Santiago-Avilés, J. J. (2001), Overview of low temperature co-fired ceramics tape technology for meso-system technology (MsST), *Sensors and Actuators A: Physical* **89**(3), 222–241.

Griss, P., Melin, J., Sjödahl, J., Roeraade, J. and Stemme, G. (2002), Development of micromachined hollow tips for protein analysis based on nanoelectrospray ionization mass spectrometry, *Journal of Micromechanics and Microengineering* **12**, 682–687.

Guerreo, I., Bocanegra, R., Higuera, F. and Fernández De La Mora, J. (2007), Ion evaporation from taylor cone of propylene carbonate mixed with ionic liquids, *Journal of Fluid Mechanics* **591**, 437–459.

Hendricks, C. D. (1962), Charged droplet experiments, *Journal of Colloid Science* **17**(3), 249–259.

Holbrey, J. D. and Seddon, K. R. (1999), Ionic liquids, *Clean Products and Processes* **1**, 223–236.

Hruby, V., Gamero-Castaño, M., Falkos, P. and Shenoy, S. (2001), Micro Newton colloid thruster system development, *in* Proc. 27th International Electric Propulsion Conference, Pasadena, California, number 281.

Huberman, M. N., Beynon, J. C., Cohen, E., Goldin, D. S., Kidd, P. W. and Zafran, S. (1968), Present status of colloid microthruster technology, *Journal of Spacecraft* **5**(11), 1319–1324.

Jackson, J. D. (1999), *Classical Electrodynamics*, 3rd edn, John Wiley & Sons, Inc.

Jahn, R. G. (1968), *Physics of Electric Propulsion*, McGraw-Hill, Inc.

Jaworek, A. (2007), Electrospray droplet sources for thin film deposition, *Journal of Materials Science* **42**(1), 266–297.

Jhuree, J., Alexander, M. S. and Stark, J. P. W. (2007), Electrostatic influence on charge to mass spectrum in mixed ion/droplet mode: implications for colloid thruster design, *in* Proc. 30th International Electric Propulsion Conference, Florence, Italy, number 120.

Kent, B., Stark, J., Stevens, B., Alexanter, M., Baker, A., Gibbon, D. and Liddle, D. (2004), A mems based experimental colloid thruster packege for nano satellites, *in* Proc. 18th Annual AIAA/USU Conference on Small Satellites, Logan, Utah, Vol. SSC04-X1-3.

Kobrak, M. (2008), The relationship between solvent polarity and molar volume in room-temperature ionic liquids, *Green Chemistry* **10**(1), 80–86.

Laermer, F. and Shilp, A. (1994), Method of anisotropically etching silicon, Robert Bosch GmbH, U.S. Patent 5,501,893.

Landau, L. D., Lifshitz, E. M. and Pitaevskiĭ, L. P. (1984), *Electrodynamics of Continuous Media*, Vol. 8 of *Course of theoretical Physics*, 2nd edn, Pergamon Press.

Legge, R. S. and Lozano, P. (2008), Performance of heavy ionic liquids with porous metal electrospray emitters, *in* Proc. 44th AIAA/ASME/SAE/ASEE Joint Propulsion Conference & Exhibit, Hartford, Connecticut, number AIAA 2008-5002.

López Urdiales, J. M. (2004), Progress in colloid propulsion, Master's thesis, Massachusetts Institute of Technology.

Lozano, P. (2003), Studies on the ion-droplet mixed regime in colloid thrusters, PhD thesis, Massachusetts Institute of Technology (MIT).

Lozano, P. (2006), Energy properties of an emi-im ionic liquid ion source, *Journal of Physics D: Applied Physics* **39**, 126–134.

Lozano, P. and Martínez-Sánchez, M. (2004), Ionic liquid ion sources: supression of electrochemical reactions using voltage alternation, *J. Colloid Interface Sci.* **280**(1), 149–154.

Lozano, P. and Martínez-Sánchez, M. (2005*a*), Ionic liquid ion sources: characterization of externally wetted emitters, *Journal of Colloid and Interface Science* **282**, 415–421.

Lozano, P. and Martínez-Sánchez, M. (2005*b*), On the dynamic response of externally wetted ionic liquid sources, *Journal of Physics D: Applied Physics* **38**, 2371–2377.

Macky, W. A. (1931), Some investigations on the deformation and breaking of water drops in strong electric fields, *Proceedings of the Royal Society of London. Series A* **133**(822), 565–587.

Mair, G. (1980), Emission from liquid metal ion sources, *Nuclear Instruments and Methods* **172**(3), 567–576.

Mair, G. (1984), Theoretical determination of current-voltage curves for liquid metal ion sources, *Journal of Physics D: Applied Physics* **17**(11), 2323–2330.

Malyshev, G., Kulkov, V., Shtyrlin, A. F., Vyshedkevich, I. and Bychkow, R. (1995), Comparative analysis of the propulsion system for the small satellites, *in* Proc. 24th International Electric Propulsion Conference, Moscow, Russia, number 156.

Marginean, I., Parvin, L., Heffernan, L. and Vertes, A. (2004), Flexing the electrified meniscus: The birth of a jet in electrosprays, *Analytical Chemistry* **76**(14), 4202–4207.

Martínez-Sánchez, M. (2004), 16.522 space propulsion, *in* MIT OpenCourseWare, URL: http://ocw.mit.edu/ [cited 31 October 2007].

Martínez-Sánchez, M., Fernández de la Mora, J., Hruby, V., Gamero-Castaño, M. and Khayms, V. (1999), Research on colloid thrusters, *in* Proc. 30th International Electric Propulsion Conference, Kitakyushu, Japan, number 014.

Martino, W., Fernandez de la Mora, J., Yoshida, Y., Saito, G. and Wilkes, J. (2006), Surface tension measurements of highly conducting ionic liquids, *Green Chemistry* **8**, 390–397.

Nakajima, O., Shiono, N., Muramoto, S. and Hashimoto, C. (1979), Defects in a gate oxide grown after the locos process, *Japanese Journal of Applied Physics* **18**(5), 943–951.

Overstolz, T., Clerc, P., Noell, W., Zickar, M. and De Rooij, N. (2004), A clean wafer-scale chip-release process without dicing based on vapor phase etching, *in* Proc. 17th IEEE International Conference on Micro Electro Mechanical Systems, Maastricht, The Netherlands, pp. 717–720.

Paine, M., Alexander, M., Smith, K., Wang, M. and Stark, J. (2007), Controlled electrospray pulsation for deposition of femtoliter fluid droplets onto surfaces, *Journal of Aerosol Science* **38**(3), 315–324.

Paine, M. D. (2002), A Micro-Fabricated Colloid Microthruster, PhD thesis, University of Southampton.

Paine, M. D., Gabriel, S., Schabmueller, C. G. J. and Evans, A. G. R. (2004), Realisation of very high voltage electrode-nozzle systems for mems, *Sensors and Actuators A: Physical* **114**(1), 112–117.

Prewett, P. and Mair, G. (1991), *Focused ion beams from liquid metal ion sources*, Electronic and electrical engineering research studies - Microengineering series, Research Studies Press LTD.

Qi, M., Wu, G., Li, Q. and Luo, Y. (2008), γ-radiation effect on ionic liquid [bmim][BF$_4$], *Radiation Physics and Chemistry* **77**(7), 877–883.

Quang Tran Si, B., Byun, D. and Lee, S. (2007), Experimental and theoretical study of a cone-jet for an electrospray microthruster considering the interference effect in an array of nozzles, *Journal of Aerosol Science* **38**(9), 924–934.

Regele, J., Papac, M., Rickard, M. and Dunn-Rankin, D. (2002), Effects of capillary spacing on EHD spraying from an array of cone jets, *Journal of Aerosol Science* **33**(11), 1471–1479.

Reneker, D. H., Yarin, A. L., Fong, H. and Koombhongse, S. (2000), Bending instability of electrically charged liquid jets of polymer solutions in electrospinning, *Journal of Applied Physics* **87**, 4531–4547.

Romero-Sanz, I., Bocanegra, R. and Fernandez de la Mora, J. (2003), Source of heavy molecular ions based on taylor cones of ionic liquids operating in the pure ion evaporation regime, *Journal of Applied Physics* **94**, 3599–3605.

Rosell-Llompart, J. and Fernandez de la Mora, J. (1994), Generation of monodisperse droplets 0.3 to 4 μm in diameter from electrified cone-jets of highly conducting and viscous liquids, *Journal of Aerosol Science* **25**(6), 1093–1119.

Schilling, A., Merz, R., Ossmann, C. and Herzig, H. (2000), Surface profiles of reflow microlenses under the influence of surface tension and gravity, *Optical Engineering* **39**(8), 2171–2176.

Schultz, G. A., Corso, T. N., Prosser, S. J. and Zhang, S. (2000), A fully integrated monolithic microchip electrospray device for mass spectrometry, *Analytical Chemistry* **72**, 4058–4063.

Seddon, K., Stark, A. and Torres, M.-J. (2000), Influence of chloride, water, and organic solvents on the physical properties of ionic liquids, *Pure and Applied Chemistry* **72**(12), 2275–2287.

Sjödahl, J., Melin, J., Griss, P., Emmer, A., Stemme, G. and Roeraade, J. (2003), Characterization of micromachined hollow tips for two-dimensional nanoelectrospray mass spectrometry, *Rapid Communications in Mass Spectrometry* **17**, 337–341.

Smith, K. L. (2005), Characterisation of electrospray properties in high vacuum with a view to application in colloid thruster technology, PhD thesis, Queen Mary, University of London.

Smith, K. L., Alexander, M. S. and Stark, J. P. W. (2005), The effect of molar conductivity upon current and thrust in a colloid electrospray thruster system, *in* Proc. 29th International Electric Propulsion Conference, Princeton, New Jersey, number 081.

Smith, K. L., Alexander, M. S. and Stark, J. P. W. (2006), Voltage effects on the volumetric flow rate in cone-jet mode electrospraying, *Journal of Applied Physics* **99**, 064909.

Stark, J., Stevens, B., Alexander, M. and Kent, B. (2005), Fabrication and operation of microfabricated emitters as components for a colloid thruster, *Journal of Spacecraft and Rockets* **42**(4), 628–639.

Stark, J., Stevens, B., Kent, B., Sandford, M. and M., A. (2003), Micro-fabrication and operation of nano emitters suitable for a colloid thruster array, *in* Proc. 4th

Round Table on Micro/Nano Technologies for Space, ESTEC, Noordwijk, The Netherlands.

Stark, K. W. and Sherman, A. (1970), Research and development in needle and slit colloid thrusters, Technical Report NASA TN D-5305, Goddard Space Flight Center, NASA.

Takahashi, N. and Lozano, P. (2008), Computational investigation of molecular ion evaporation in electrospray thrusters, *in* Proc. 44th AIAA/ASME/SAE/ASEE Joint Propulsion Conference and Exhibit, Hartford, Connecticut.

Taylor, G. (1964), Desintegration of water drops in an electric field, *Proceedings of the Royal Society of London. Series A, Mathematical and Physical Sciences* **280**(1382), 383–397.

Velásquez-García, L. (2004), The design, fabrication and testing of micro-fabricated linear and planar colloid thruster arrays, PhD thesis, Massachusetts Institute of Technology (MIT).

Velásquez-García, L. F., Akinwande, A. I. and Martínez-Sánchez, M. (2006), A planar array of micro-fabricated electrospray emitters for thruster applications, *Journal of Microelectromechanical Systems* **15**(5), 1272–1280.

Wang, L., Stevens, R., Malik, A., Rockett, P., Paine, M., Adkin, P., Martyn, S., Smith, K., Stark, J. and Dobson, P. (2007), High-aspect-ratio silica nozzle fabrication for nano-emitter electrospray applications, *Microelectronic Engineering* **84**(5-8), 1190–1193.

Wilkes, J. and Zaworotko, M. (1992), Air and water stable 1-ethyl-3-methylimidazolium based ionic liquids, *Journal of the Chemical Society, Chemical Communications* **13**, 965–967.

Yarin, A., Koombhongse, S. and Reneker, D. (2001), Taylor cone and jetting from liquid droplets in electrospinning of nanofibers, *Journal of Applied Physics* **90**, 4836–4846.

Zeleny, J. (1914), The electrical discharge from liquid points, and a hydrostatic method of measuring the electric intensity at their surfaces, *Physical Review* **3**(2), 69–91.

Zeleny, J. (1917), Instability of electrified liquid surfaces, *Physical Review*.

Ziemer, J. K., Gamero-Castaño, M., Hruby, V., Spence, D., Demmons, N., R., M., Roy, T., Gasdaska, C., Young, J. and Connolly, B. (2005), Colloid micro-newton thruster development for the ST7-DRS and LISA missions, *in* Proc. 41st AIAA/ASME/SAE/ASEE Joint Propulsion Conference and Exhibit, Tucson, Arizona, number AIAA 2005-4265.

Ziemer, J. K., Randolph, T. M., Franklin, G. W., Hruby, V., Spence, D., Demons, N., Roy, T., Ehrbar, E. and Zwahlen, J. (2008), Delivery of colloid micro-newton thrusters for the space technology 7 mission, *in* Proc. 44th AIAA/ASME/SAE/ASEE Joint Propulsion Converence and Exhibit, Hartford, Connecticut, number AIAA 2008-4826.

Zorzos, A. and Lozano, P. (2008), The use of ionic liquid ion sources (ILIS) in FIB applications, *in* Proc. 52nd International Conference on Electron, Ion, and Photon Beam Technology & Nanofabrication, Portland Oregon, number 35910.

Curriculum Vitae

Renato Krpoun

Microsystems for Space Technologies Laboratory
Ecole Polytechnique Fédérale de Lausanne (EPFL)
1015 Lausanne, Switzerland
`renato.krpoun@a3.epfl.ch`

Personal

Date of birth:	January 14, 1978
Nationality:	Swiss and Brazilian
Civil status:	Single

Education

2004 - 2008 PhD candidate, Microsystems and Microelectronics

Ecole Polytechnique Fédérale de Lausanne (EPFL), Switzerland

Research topics: micromachining, electrospray thrusters, satellite design

1998 - 2004 Master of Science, Microengineering

Ecole Polytechnique Fédérale de Lausanne (EPFL), Switzerland

Master thesis title: Design of a simulator for an electric motor drive for satellite

1991 - 1998 Swiss Maturity, Ancient Languages

Kantonsschule Oerlikon, Zürich, Switzerland

High School Exchange:

1995 - 1996 Reynolds High School, North Carolina, USA (11 months)

Further Training and Academic Awards:

2008 Venture challenge
Entrepreneurship course

2004 National Instruments Price
For a high quality master thesis using National Instruments products

Experience

2004-2008 **Research Assistant, EPFL**

- SwissCube satellite system engineer
- Space technology and operations course, teaching assistant

2000-2005 **Student Space Exploration and Technology Initiative, EPFL**

- Design and manufacture of a DSP based electronic control unit for the propulsion system on the SSETI Express satellite (launched in 2005)
- Co-organizer of the 2004 Space Technology Education Conference at EPFL
- Appointed first SSETI association vice-president (2004)
- Participated in the 2002 ESA Student Parabolic Flight Campaign to test a solar panel deployment mechanism

Internships:

1998   **ABB High Voltage Technologies, Baden, Switzerland**

- Development of a LabView monitoring system for long duration data recording

PATENTS

Krpoun, R., Scheidegger, N., Shea, H. and Charbon, E. (2008), Method and apparatus to determine a planet vector, European Patent No. 1 950 540 A1 (filed on 23/01/07).

PUBLICATIONS

Journal Articles

Krpoun, R. and Shea, H. R. (2008), A method to determine the onset voltage of single and arrays of electrospray emitters. *Journal of Applied Physics*, **104**(6), 064511.

Krpoun, R. and Shea, H. R. (2008), Integrated out-of-plane nanoelectrospray thruster arrays for spacecraft propulsion. *Journal of Micromechanics and Microengineering*, submitted November 2008.

Krpoun, R., Smith, K. L., Stark, J. P. W. and Shea, H. R. (2008), Tailoring the hydraulic impedance of out-of-plane micromachined electrospray sources with integrated electrodes. *Applied Physics Letters*, submitted December 2008.

Contribution to conferences

Krpoun, R., Räber, M. , Smith, K. L., Stark, J. P. W. and H. R. Shea (2007), Design and fabrication of an integrated MEMS-based colloid micropropulsion system, *in* Proc. 30th International Electric Propulsion Conference, number 099.

Scheidegger, N., Krpoun, R., Niclass, C., Charbon, E. and Shea, H. R. (2007), A new concept for a low-cost earth sensor: Imaging oxygen airglow with arrays of single photon detectors, *in* Advances in the Astronautical Sciences, **128**, pp. 501–517.

Krpoun, R. and Shea, H. R. (2007), Micromachined electric propulsion using ionic liquids as fuel, *in* Proc. of the 14th International Workshop on the Physics of Semiconductor Devices, IWPSD, no. 4472610, pp. 652–655.

Krpoun, R., Räber, M., and Shea, H. R. (2008), Microfabrication and test of an integrated colloid thruster, *in* Proc. 21st IEEE International Conference on Micro Electro Mechanical Systems, pp. 964-967.

Shea, H. R., Krpoun, R., Smith, K. L. and Stark, J. P. W. (2008), Design and fabrication of an integrated MEMS-based colloid electric micropropulsion system, *in* Proc. 5th International Spacecraft Propulsion Conference.

Krpoun, R. and Shea, H. R. (2008), Onset Voltage Modeling of Micromachined Colloid Thrusters, *in* Proc. 44th AIAA/ASME/SAE/ASEE Joint Propulsion Conference and Exhibit, AIAA-2008-5003.

LANGUAGES

Native German and Portuguese
English (Cambridge Certificate of Proficiency)
French (Proficient speaking and writing)